Università
Ca'Foscari
Venezia

Master's Degree programme – Second Cycle
(*D.M. 270/2004*)
in Sciences and Technologies of Bion and Nano-materials

Final Thesis

Ca' Foscari
Dorsoduro 3246
30123 Venezia

STUDY OF OSTEOINTEGRATION PROCESSES ON DIFFERENT MODULATED SURFACES OF SILICON NITRIDE CERAMICS USING OSTEOSARCOMA (SAOS-2) AND MESENCHYMAL STEM CELLS (MSCs)

Supervisor
Prof. Pietro Riello
Prof. Giuseppe Pezzotti

Graduand
Francesco Boschetto
846474

Academic Year
2015 / 2016

Abstract

The study of the interactions that take place between the bone and an artificial implant is very important in the development of a new material used in the prosthetics field.
Osteointegration is a direct structural and functional connection between biological components of bone tissue and the artificial material implanted inside the body. In this dynamic process, an important role is played by the implant in modulating molecular and cellular behavior. Many materials are used in the production of prosthetic implants including metal alloys, polymers and ceramics. Among the latter silicon nitride is one of the most studied. This non-oxide material can be functionalized with different treatments. In this way its chemistry can be varied from of a silica-like surface to one mainly consisting of amine groups.
In this study different surface-treated silicon nitride samples have been tested in biological environments using two different cell lines: Osteosarcoma (SAOS-2) cells and Periodontal ligament stem cells (PDLCs).
The samples have been divided in two groups:

- “as sintered” mechanically untreated on the surface, used in SaOS-2 treatment
- “as-polished” with lapped surface, employed in PDLCs treatment

For every groups there are five types of different surface-treated samples:

- non-treated
- HF treated, using hydrofluoric acid,
- N_2 baked in N_2 atmosphere and high temperature,
- thermally oxidized, exposing the sample to ambient atmosphere at high temperature
- glazed presenting Si(Y)AlON on the surface.

Alumina and Titanium alloy, two biomaterials currently employed in orthopedic applications, have been used for comparison. To verify the osteointegration process, the formation and the growth of hydroxyapatite (HA) on the surface of the samples have been evaluated through techniques such as Raman spectroscopy and laser microscope. The results have shown the presence of biological compounds and HA in different quantities in all the samples confirming the good biocompatibility and osteointegration properties

of silicon nitride. PDLCs presented a lower quantity of HA as compared to samples treated with SAOS-2 cells. This is probably due to the surface features of the samples. The binding mechanism of the cells to the material can be influenced by the roughness of the different surfaces and by the surface charge. This work provides a basis for future studies to understand which kind of treatment and material's features can give the best benefits to promote osseointegration process, thus boosting the development of the new non-oxide ceramics for biomedical applications.

Summary

Aim of the thesis

The purpose of this thesis is to verify the osseointegration properties of silicon nitride samples subjected to various surface treatments. Two cell lines have been used: cells of osteosarcoma and mesenchymal cells respectively obtained from the periodontal ligament. Interactions with sample surface has been investigated and formation of hydroxyapatite, indication of an osseointegration process, has been verified.

After cell culture, the samples have been analyzed by various analytical techniques including Raman spectroscopy and Laser microscope.

Chapter 1

Introduction

Given the increase in life expectancy throughout the whole world, the number of joint replacement operations is growing year by year. In Italy, more than 1,6% people have joint replacement. Every year in our country the number of shoulder, hip and knee surgeries is over 200,000 (ANSA). The majority relates to hip surgeries, which amounted to 60% and this percentage is set to rise annually by 5%. A high percentage of implant used is also present in America (about 325,000 hip and 300,000 plants in the knees) and even in Europe where respectively 230,000 and 700,000 hip and knee implants are made. Also in the field of dentistry, following the advent of new biocompatible prosthetic implants, such as those constituted by a titanium alloy, there is a high number of yearly interventions. Nearly half a million oral implants are performed each year worldwide.

Despite the improvements in the sector, there are still many reasons for which the application of prosthetic implants may lead to complications.

One of the main reasons is the incorrect positioning of the prosthetic components that can lead to an incorrect distribution of stress within the system [1,2].

This complication can greatly affect the bone remodeling process at the interface bone-implant [3,4,5]. Another problem may be the occurrence of infections that triggers an inflammatory process while preventing the osseointegration process.

This last aspect, which is present almost exclusively in situations involving orthopedic implants and not dental, is of significant importance in the development of a biomaterial deputy to the construction of an implant. A number of materials have been studied to improve the biocompatibility and at the same time promote interaction and bone-implant contact. It also guarantees the absence of immune reactions by the individual because there is no input from other cells or organisms.

In prosthetic market there are different materials which have different functions, replacement, improvement and recovery of tissues or organs; these materials also differ depending on the material that constitutes them: metals such as titanium alloys or stainless steel 316L, having high mechanical strength associated with chemical inertness; organic materials such as polyethylene, and ceramic materials oxide and non-oxide.

Among these materials there is the silicon nitride, a non-oxide bio-ceramic which has characteristics that make it one of the possible materials used in the field of implants even in a future perspective.

Over the last few years, chemical and physical characteristics of this material have been studied, trying to functionalize the surface to make it more akin to the interaction with the load bearing articulation environment and to stimulate the osteointegration and osteoconductive processes, through the use of different mechanical and chemical treatments, keeping its main features.

1.1 Background: Bone tissue

Bone tissue is a connective tissue which has the support functions of an individual and is characterized by high strength and a high hardness. It is responsible for the architecture and the structure of the bones that form the skeleton of vertebrates. The bone tissue mainly consists of cells present in an extracellular matrix, which is in turn formed from an amorphous substance glycoprotein, fibers and which presents also a mineral compound noted as hydroxyapatite. The amorphous substance has the particular characteristic of being subject to a process of mineralization and calcification. So the extracellular matrix produced by the same cells constituting the tissue is formed by both inorganic materials mineralized and organic material, very similar to that of the connective tissue, in particular to the cartilage. The prevailing part of the extracellular matrix appears to be the type I collagen fibers. The latter, in adult bone, are arranged in order to obtain a triple helix structure that increases the compactness of the tissue; this complex, fibers and cells make up a laminated shaped structure. The collagen fibers confer a tensile strength to the bone but they are not resistant to compression because of their length. Given its anisotropy, collagen properties strongly depend on their structural arrangement, density

and elasticity. Fibers are arranged parallel to each other, conferring flexibility to the bone structure.

In addition to collagen fibers, in the matrix there are also other components for the adhesion and anchoring mechanisms. These components are fibronectin, thrombospondin and osteopontin protein. In the matrix, there is also another very important protein known as osteocalcin and bone-GLA-protein (BGP) synthesized by osteoblasts and having endocrine functions. They play a significant role in bone mineralization mechanisms. The same function is also covered by another protein of the bone matrix, the osteonectin which favors the formation of mineral crystals and also shows a high affinity for collagen.

As previously noted, the organic part of the bone also presents different cell types deputies to the formation and maintenance of the implant itself:

- Osteo-progenitor cells;
- Osteoblasts;
- Osteocytes;
- Osteoclasts.

The osteo-progenitor cells are mesenchymal stem cells. They have different properties because they can proliferate and differentiate into osteoblasts and are located mainly in the periosteum and endosteum. When reactivated, they proceed to new bone formation.

Osteoblasts are the basic cells of the bone tissue, responsible for the formation of matrix components which arise from the differentiation of mesenchymal progenitor cells. They are characterized by a massive body with an ovoid nucleus not centered but slightly peripheral, are highly polarized and have basophilic cytoplasm as it presents an endoplasmic reticulum rough very extended as well as Golgi apparatus. Osteoblasts have osteogenic function; they are deputies to the synthesis of molecular components of the organic matrix (osteoid) and the deposition of the inorganic matrix. They produce type I collagen, osteocalcin, osteonectin, osteopontin and bone sialoprotein. The latter are expelled by exocytosis and go to act outside of the cell, acting as a support in the deposition process of the calcified matrix.

When bone formation is completed, osteoblasts are trapped inside of the bone matrix gaps created by them. From here become osteocytes, living cells in a quiescent state which provide for the maintenance of bone extracellular matrix. They have an irregular shape with a clearly visible nucleus, endoplasmic reticulum rough and Golgi apparatus underdeveloped and cytoplasm has several extensions. Through these extensions, the

cells are able to obtain the nutrients that are inside of microscopic tunnels called canaliculus. Through these canaliculus, the cytoplasmic extensions of the osteocytes can make contact with each other through gap junctions or with blood capillaries placed in bone channels allowing the exchange of metabolites. Osteocytes can also keep in contact with osteoblasts through appropriate signals sent by the latter that can control osteocytes if there is a need to lay down new bone extracellular matrix. The function of osteocytes is to participate in the remodeling of the bone tissue in response to stimuli of calcitonin and adjusting the levels of calcium and phosphorus. Osteocytes also have membrane receptors for parathyroid hormone (PTH), which allows control of the osteoclasts.

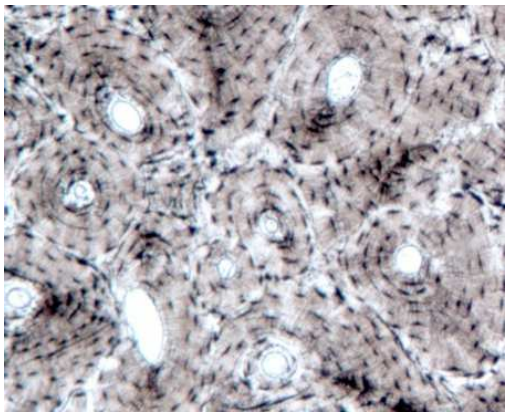

Figure 1.1: Section of lamelar bone tissue.

Osteoclasts do not belong to osteoprogenitress line but derive from the merger of several monocyte precursors (up to thirty), and are assigned to produce and secrete enzymes that destroy the calcified matrix and then allow bone remodeling. These cells come into action during the growth processes with the replacement of the immature bone tissue in the adult form, and to implement subsequent bone remodeling.

Osteoclasts are very large, diameter exceeds 100 microns and have numerous internal nuclei. They are also highly polarized: if they are activated, osteoclasts have a cytoplasmic face bone proximity, with very mobile ripples that adhere to the bone surface, creating a completely isolated from the surrounding microenvironment. The isolated part is subject to acidification with activation of lysosomal enzymes such as protease and phosphatase or other non-lysosomal enzymes such as metalloproteinases. Thus, it has the occurrence of erosion of the bone matrix and the consequent formation of a defined depression of Howship lacuna.

The inorganic part of bone tissue is formed instead of several constituents: calcium, which combines with oxygen, phosphorus and hydrogen. These go on to form a molecule known as hydroxyapatite, the mineral compound that goes on to form thin crystals having the shape of prisms, but there are also other minerals such as magnesium phosphates and citrates of sodium, manganese and potassium. This mineral component in the body of an adult human is about 65% of the dry weight of the bone tissue while the organic part goes to make up the remaining 35%.

The process that leads to bone formation is known as osteogenesis or ossification and takes place starting from mesenchymal progenitor cells of the bone.
The ossification may be of two types mainly:

- Direct or intramembranous;
- Indirect or chondral.

Intramembranous ossification takes place a direct passage from mesenchymal cells for the formation of a bone tissue while through indirect ossification the intermediate formation of hyaline cartilage occurs.
The direct ossification follows the organization in mesenchymal cell aggregates differentiate into osteoblasts and proceed to the deposition of bone extracellular matrix subsequently mineralized. In this way the non-lamellar primitive bone tissue is formed and will be replaced by lamellar bone tissue in response to remodeling. Examples of direct ossification relate to the flat bones and short bones, ie bones that have no supporting function.
The indirect ossification instead is a process that leads to bone formation starting from a cartilaginous structure to obtain a structure highly resistant to compression and therefore suitable for the function of support.

1.2 Bases of osteointegration

Per-Ingvar Branemark, a Swedish professor of applied biotechnology coined the term "osseointegration" at the end of the sixties, referring to "a direct anchoring, an intimate union, of an implant to a bone without the presence of apparent connective tissue" [6]. This particular phenomenon emerged for the first time in 1952 during an experiment carried out in vivo on rabbit and having the purpose of studying the healing of bone fractures processes. Using a titanium container in order to analyze the passing blood flow through the bone tissue, he indeed noticed that the container could no longer be removed, and it was integrated to the bone. Subsequently Schroeder also confirmed, in 1976, the formation of osseointegration due to direct contact between bone tissue and peri-implant surface [7]. Studies later convinced him on the use of titanium, its biocompatibility and integration within the bone. Others like Albrektsson and Zarb defined osseointegration as

"the process by which you get a direct contact at the microscopic level, between the implant made of alloplastic and biocompatible materials and the bone tissue that is constantly changing. Fixation, clinically asymptomatic, must be rigid and maintained under load "[8,10]. Dorland instead identified the osseointegration as "a direct anchorage of an implant through the formation of bone tissue around the implant itself without the growth of fibrous tissue in the area of contact between bone and implant" [11]. Branemark will also define the osseointegration process as "a direct connection, structural and functional between a vital bone and the surface of an implant subjected to load" and that "the fundamental requirement for establishing a real tissue integration and durable by a non-biological material is based on the detailed understanding of the response of the hard and soft tissues of the receiving site, the surgical preparation and the installation of the prosthesis implant" [12].

Other studies were made regarding osseointegration, such as those conducted by Osborn and Newesley where features showed two distinct pathways of bone formation: *distance osteogenesis* and *contact osteogenesis* [13,14].

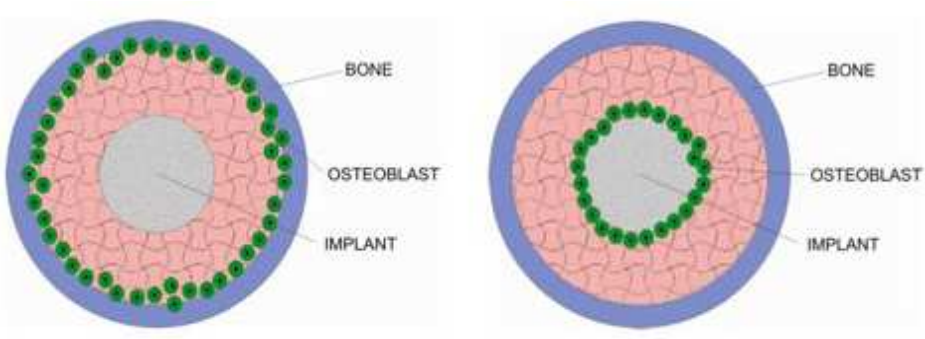

Figure 1.2:Two forms of osteogenesis: distance osteogenesis and contact osteogenesis.

The first relates to a process of deposition of osteoblasts and subsequent mineralization that starts from the bone tissue surface already present and goes towards the implant; the bone goes to slowly encircle the prosthesis. [15, 16] The contact osteogenesis, instead, takes place in the opposite way; the bone tissue is formed directly above the implant surface that is colonized by bone cells which differentiate into osteoblasts and leading to the subsequent formation of bone matrix. This osteogenesis process follows the model of "fracture repair". [17]

Nowadays the osseointegration study led to the development and use of several prosthetic implants in treatments subsequent to amputations as a bone-anchored hearing aids, neck

and hip joints of the fingers, thumb and major arts [18,19,20,21,22] or to replace prosthetic joints such as the hip, knee and spinal implants.

It's necessary also, to point out that the osseointegration phenomenon is related to two other that are the osteoconduction and osteoinduction.

Hench and Wilson have suggested that the osteoconduction is the process by which a bone grows in conformity with the surface of a material [23]. The bone growth on a surface depends on cell differentiation. They may originate in osteoblasts or pre-osteoblasts due to an injury or simply through a recruitment process undertaken by mesenchymal progenitor cells by osteoinduction.

Albrektsson [24] has studied how the osteoconduction and the in vivo remodeling require a full vascularization necessary to transport all those components involved in bone formation such as the growth factors and plasma proteins. Among the main growth factors deputed to the formation of bone tissue there are the TGF-β, the platelet-derived growth factor (PDGF), the insulin-like growth factors (IGF-I, IGF-II) and the factor of growth of fibroblasts (FGF). These act as signaling agents of cells and capable of stimulating the proliferation and cell differentiation.

Osteoinduction indicates the ability of a material to stimulate pluripotent cells, primitive, undifferentiated to develop a particular cell line deputed to bone formation; briefly it is the process by which via migration of certain cells, differentiation and proliferation, there is the formation of a bone tissue, then osteogenesis is induced [23].

As already stated earlier, in addition to differentiated cells such as osteoblasts, osteoclasts and osteocytes, the bones contain a certain number of undifferentiated mesenchymal cells which are of considerable importance for a proper healing or for anchoring to an implant because they can be used as osteo-progenitor cells. The latter may develop following a correct stimulus, by means of inductive agent, in pre-osteoblasts.

One of the main osteoinductive agents is the glycoprotein BMP, belonging to the family of transforming growth factors (TGF-β). During the remodeling process about fifteen BMP are released including BMP-2 and BMP-7, two morphogenic proteins which potentially induce osteoblast differentiation in a variety of cell types.

Bone Induction may be affected directly or indirectly also by stress factors or electrical signals. [25,26,27,28]. It is a referral biological mechanism that occurs regularly, for example during the healing period subsequent to a fracture or after the incorporation of a prosthetic implant.

According to Frost [29,30] after fracture a repair process reactivates involving the same bone, bone marrow and surrounding tissues sensitizing the surviving cells.
After the injury, a series of biochemical and physical local messages, that help cells respond appropriately, are released. Some of them appointed to differentiation and cell organization, while others favor the mitotic reproduction.
It is in this initial part of the healing response that osteoinduction occurs, present immediately after the injury, and very active during the first week.

1.3 Factors that influence osteointegrations

The factors that play a decisive role during the osseointegration process are the primary stability (mechanical stability) and secondary stability (biologic stability after the bone remodeling).
The primary stability is the prerequisite for the advent of osseointegration process. It is a mechanical stability and is created as soon as the implant is inserted in the body and enters in direct contact with the bone. This contact depends on implant shape, bone quality and preparation of the implant site through osteotomia. The fixation of implant must be able to be resistant to those of displacement forces acting on the implant. If these forces are able to also induce a minimum implant mobility during healing, it could introduce a disturbance in the bone formation process up to a subsequent failure of osseointegration process. The biological fixation requires several weeks. The speed in the achievement of stability can vary through the use of modified implant surfaces that allow a high stability of the clot and at the same time accelerate the osseointegration process. The secondary stability, or biological stability, occurs when the remodeled bone is subject to new areas of contact with the implant surface. Here osteoblasts come into play forming new bone matrix and the osteoclasts that, instead, ensure clean up waste products previously.
This process takes over gradually to the first and after healing, the primary stability is fully replaced by the secondary stability (Figure 1.3).

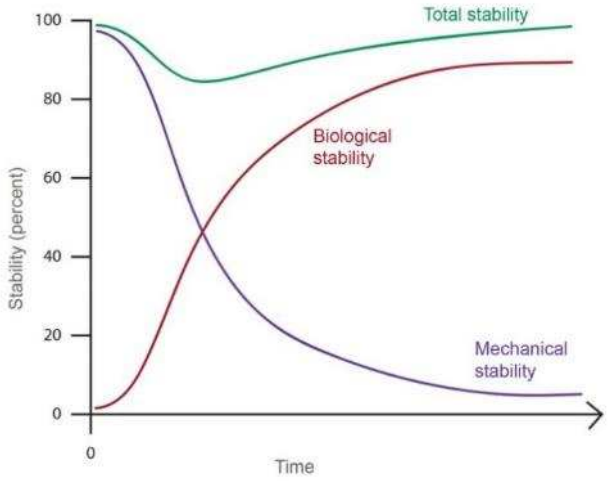

Figure 1.3: Diagram of primary and secondary stability.

However, there is a critical phase characterized by a poor stability of the implant because the pre-existing bone is not yet completely resorbed while the newly formed is still not mature to be able to maintain the loads.

There are other very important factors to consider so that the osseointegration process proceeds in the manner most appropriate and satisfactory as possible [31-37]:

- System design;
- Plant Chemical composition;
- The topography of the area and possible surface treatments;
- The material and its shape and length;
- The host bone;
- The healing mechanism;
- The mechanical stability and load conditions applied;
- The use of osteogenic adjuvant, stimulants or biological coatings;
- Biocompatibility of the material.

Another important factor which can influence the osteointegration process is the surface charge of a material. many researchers reported the improved-biocompatibility, cell affinity and cell differentiation on the implanted surfaces by using the positive ions and the negative ions [38]. For instance, hydrogels scaffolds incorporated with positive charges supported significantly more cell attachment and spreading of osteoblasts and fibroblasts as compared to negative or neutral charges [39]. Another group, also, investigated that negatively charged hydrogels scaffold increased at the extents of chondrocyte differentiation, such as collagen and glycosaminoglycan expression, in

comparison with that on the neutral or positively charged hydrogel scaffolds [40]. The distribution of charges that a material presents to the surface can affect the wettability and, therefore, may confer hydrophilic or hydrophobic characteristics to the material. This fact has been confirmed in numerous studies, varying the surface charge in the analyzed samples and observing as well as the adhesion and cell behavior would behave differently depending on the surface charge. A comparison between the polarized and non-polarized HA samples was made by Nakamura et al. The samples showed difference in wettability, given that those non-polarized showed an angle of contact greater than those polarized. The result in in vitro tests led to the conclusion that polarized surfaces, positively and negatively, favored the adhesion and cell growth [41]. In the case of work done by Masataka et al., Negatively polarized surfaces, and brought accession osteoblast cell proliferation compared with positively charged surfaces and non-polarized [42]. Same conclusions were reissued by Bodha et al. in 2009 [43]. But in the case of the studies done by Kizuki et al., emerged opposite results in which the cells of osteoblast favored samples with negatively charged surfaces [44].

In addition to these we must also consider the factors that can inhibit the osseointegration process [45-47]:

- Excessive plant mobility;
- A not adequate porosity of the material;
- Use of certain drugs such as methotrexate, cisplatin, warfarin, cyclosporin A;
- Non-steroidal anti-inflammatory drugs and how the COX-2 inhibitor.

Even the patient's condition can lead to problems in the development of osseointegration if present osteoporosis, rheumatoid arthritis, poor nutritional conditions, kidney failure, smoking and also the patient's age [48-51].

The features related to the implant surface used are of considerable importance because certain morphological characteristics (ex. Roughness) and surface chemistry can affect the surface energy and consequently the primary interaction between the implant body and environment. Following recent studies, it has been seen as a high surface energy of the plant is beneficial in the integration process. [52] Then the roughness is another factor imported relative to the surface. Curved surfaces that possess cavities or pores having dimensions or comparable rays to those of biological components can interact differently

with respect to those little rough surfaces. The surfaces, which have high roughness, promote osseointegration through membership of cellular components such as platelets and monocytes that allow direct attachment of osteoblasts and subsequent proliferation [53]. It is important, however, to consider how the implant surface should present a correct roughness. studies using samples with high surface roughness showed an unfavorable cell adhesion compared to other samples presenting a lower roughness indicating how certain types of particularly fond moderate roughness cells [54,55].

As indicated above, a very important factor concerns also the load conditions because due to variations of the latter, a remodeling of the bone tissue can occur. To explain the functional adaptation of the bone subjected to load, the Mechanostat theory mathematically described by Frost in 1989 can be used [56].

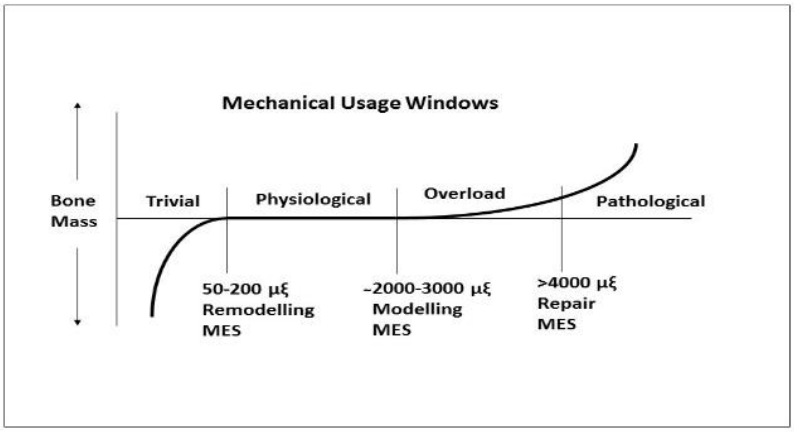

Figure 1.4: Mechanostat theory graph about bone mass-amplitude deformations.

This theory presents four levels of load increasing bone:

- Pathologic unload areas - if no force is applied on the bone then its minerals and consequently its resistance are lost (ex non usu atrophy). Characterized by deformation of less than 200 microstrain (με);
- Adaptation areas - if the bone is properly stimulated, the right physiological remodeling is created. The deformations amount in the range between 200 and 2000 με, range of physiological loads;

- Overload zone - if the applied force exceeds the adaptation area, the bone tissue reacts by opposing the external stimulus with activation of osteoblasts and new bone apposition. Deformations in the range between 2000 and 3000 με;
- Pathologic overloaded zones: if the load exceeds the physiological range can inhibit the function of osteoblasts, and therefore the osteoclastic function prevails. Consequently, the bone becomes weaker and in the case of dental implants osseointegration doesn't occur. Finally, overcoming the elastic limit and fabric strength are witnessing the bone fracture. The deformation exceeds the limit of 3000 με.

Following a higher load than necessary, there is a greater activity of osteoblasts and thus, an increase of bone formation while if there is a lower load, a resorption can occur. So it is important to accurately evaluate the intensity of the load.

An incorrect load distribution can also lead to another phenomenon known as "*stress shielding*" which leads to a reduction in bone density (osteopenia) [57]. *Stress-shielding* can be caused by the discharges of the forces which don't take place correctly. They are supported by the prosthesis and not by the bone that tends to atrophy leading to a demineralization, a bone resorption with loss of mechanical stability given by the prosthesis mobilization [58,59].

If this phenomenon occurs, the osseointegration process hardly happens.

Even the bone quality interested to the intervention and the implant site have to be considered. A healthy bone is very important because it provides cells, growth factors, local regulators and nutrients through the blood vessels near so that allow rapid healing; on the contrary osteoporosis seems to compromise the primary and secondary stability, therefore the mechanical fixation. Furthermore, disease like osteoporosis can affect mesenchymal cells, cell proliferation (low osteoblast), protein synthesis and the reactivity of cells to local factors [60,49]; moreover, vascularization may be compromised [61,62].

The implantation site influences the osseointegration process through the type of bone tissue which is in direct contact with the prosthesis. The process varies depending on whether it has a lamellar bone tissue or a non-lamellar bone tissue.

The lamellar bone tissue can be divided in compact (cortical) and spony tissue. It consists of lamellas that confer resistance to stress especially in compact tissue, which is equal to 80% of the total bone tissue and is responsible for the protective and support functions of the skeleton. In contrast to the non-lamellar bone tissue it is a compact tissue and

promotes primary stability. Studies have shown that an implant placed in the bone lamellar shows a percentage of bone-implant contact that reaches 90%, however this percentage can go down to 50% if the implant is placed in the medullary bone [63,64].
The functionalization of a material with biological components or through coatings can increase the osseointegration process [36,37]; Conventional coating systems using different growth and differentiation factors have been developed in order to accelerate the healing process and thus, to improve bone cell growth and to strengthen the bond of the tissue implant [31].
Among these, the most important growth and osteogenesis factors used are [65-68]:

- Bone morphogenic protein (BMP) (in particular BMP-2 and BMP-7);
- Osteogenic protein (OP-1);
- Growth factor derived from protein (PDGF);
- Insulin-like growth factor (IGF);
- The transforming growth factor beta (TGF-β1, TGF-β2);
- Collagen and extracellular matrix proteins such as fibronectin and vitronectin or the parathyroid hormone (PTH).

1.4 Cellular treatments

1.4.1 Osteosarcoma cells (SAOS-2)

The SAOS-2 is a human tumor cell line isolated the first time in 1973 by Fogh [69] that has its own characteristics of osteoblasts and is used as a research resource inherent in bone tissue behavior [70]. Through the use of the SAOS-2, cell line, it is possible to obtain a large number of cells in a very short time; also they can easily differentiate the same way with which naturally differ osteoblasts [71].

The SAOS-2 is ideal for the study of bone tissue development in vitro because of its ability to produce a mineralized extracellular matrix [72].

These cells have shown from previous analyses how the structure of collagen synthesized is very similar to that synthesized by human osteoblasts but have a high level of hydroxylation of lysine which becomes hydroxylysine through the action of the enzyme lysyl hydroxylase [73,74]. Thus, a continuous production of collagen takes place, and the latter is then glycosylated.

Important feature of this cell line is the activity of alkaline phosphatase that is still high in the time unlike normal cells.

Vesicles of alkaline phosphatase, in the extracellular matrix, have a very important role in the bone mineralization process. SAOS-2 cells can be stimulated by dexamethasone as well as phosphate substrates influencing cell phenotype [74].

As regards the growth factors and cytokines, the values in the cell line SAOS-2 are comparable to those of normal osteoblasts [74]; Moreover, it is seen that the SAOS-2 showed an expression level of parathyroid hormone (PTH) and calcitriol (1,25 (OH) 2 D3) similar to that expressed by osteoblasts, both in vivo and in vitro.

The adhesion and spread of SAOS-2 is permitted thanks to the presence of two integrins, the β_1 subunit and the α_v subunit which are really important for cells adhesion, proliferation and formation of mineralized extracellular matrix.

Recent studies have shown that these cells have a strong interaction with fibronectin rich substrates by binding the α_v integrin subunit [74,75].

1.4.2 Periodontal ligament stem cells (PDLSCs)

The second cellular treatment was done using mesenchymal cells, particularly stem cells from periodontal ligament (PLDSCs). PLDSC, are multipotent cells that can differentiate into adipocytes, osteoblasts, chondrocytes and cementoblasts producing mineralized tissue influenced by certain factors such as the tissue origin, inflammatory conditions, the growth factors present, the donor's age and the ground of culture when treated in vitro.

This cell line has a high proliferation capacity and express markers on the surface of the membrane as the fibroblast growth factor (FGF) and endostatin. The PDLSC also express certain markers such as CD105 [76-81], CD90 [76-78, 81, 82], and CD73 [80,83]. Moreover, they possess immuno-modulatory activity comparable to those of the mesenchymal cells of bone marrow (bmMSCs). They have a low immunogenicity due to the fact that there are molecules having costimulatory activity of T lymphocytes and HLA-DR II, specifically, there are no two markers CD80 and CD86 [84]. The PDLSCs inhibit the proliferation of allogeneic T lymphocytes via an upregulation of prostaglandin E2 (PGE-2) and cyclooxygenase-2 (COX-2) and also inhibit the proliferation, differentiation and migration of B lymphocytes [85].

Several studies have been made to analyze the osteogenesis properties of this cell line; Gay et al., checked the differentiation and proliferation capacity by examining the level of alkaline phosphatase and sialoproteins (BSP) in the mesenchymal cells of the periodontal ligament (PDLSCs), in mesenchymal cells of bone marrow (bmMSCs), and performing a collection of chondrocytes and adipocytes [86]. The result showed that, despite different initial levels of alkaline phosphatase, the two lines have the same differentiation and proliferation capacity [86]. In recent years, many experiments were done using PDLSCs mesenchymal cells that have occurred a significant regeneration of bone tissue after osseointegration peri-implant [87].

Tests using other mesenchymal cells such as GMSCs (cells mesenchymal gum) have been performed confirming that the mesenchymal cells of the periodontal ligament had more osteogenic and bone formation potential [88,89]. In vivo tests showed the formation of "cementum-like tissue" after the application of a system [90-93]. The mechanism of formation is given by the presence and migration of cementoblasts and precursor cells from the ligament periodontal towards the implant [94] due to the direct contact with the bone tissue implant.

Chapter 2

Materials and Methods

2.1 Material: Silicon Nitride

Silicon nitride is a non-oxide ceramic that expresses unique properties and that for this reason is the subject of study and development in the medical field, in particular in orthopedics [95-99].

It is hardly present in nature; It was first observed in 1990 in meteorites and analyzed by Alfred O.C. Nier [100]. It was synthesized starting from 1857 thanks to Henri Etienne Sainte-Claire Deville and Friedrich Wohler [100] that warmed silicon tetrachloride in nitrogen atmosphere using a crucible placed inside another of carbon-rich coating crucible for the purpose of reduce the oxygen permeation.

The exact chemical composition was unknown until 1879 when Paul Schutzenberger heating the silicon in nitrogen using a carbon paste (coal or coke mixed with clay used for crucibles), made a product with Si_3N_4 composition [101].

In 1910, Ludwig Weiss and Theodor Egelhardt warmed silicon in rich pure-nitrogen environment in order to obtain silicon nitride [102].

Another protocol (proposed by Friederich and L.Sitting and performed in 1925) provided carbo-thermal reduction under nitrogen, by heating the silica, the nitrogen and carbon to 1250-1300 ° C [103].

Since then, for a few decades, the silicon nitride remained nothing more than a mere curiosity until the early post-war years, when it began to be used in commercial applications. From 1948 to 1952 an American company, the Carborundum Company, (Niagara Falls, New York,) came into possession of several patents for the production and application of silicon nitride [100].

Later in 1958 the International Haynes (Union Carbide) used silicon nitride for commercial purposes producing thermocouple tubes, crucibles for melting metals and nozzles for different uses.

This material is used nowadays in various industrial fields and not, including the development of high-performance bearings for turbine blades, spark plugs, uses in electronic fields such as the development of cantilevers and other materials having such characteristics high hardness, strength and wear resistance [104].

The use of silicon nitride in different industrial applications has allowed to improve the mechanical properties by different methods of treatment and refining, and with the use of additives and treatments to create composites.

These properties have led silicon nitride to be used also in the medical field, in particular in the production of knee and particularly of spinal implants [105-107]. Indeed, about 25,000 spinal implants, fusion cages, were produced from 2008 until today with a low incidence of adverse events [108].

Silicon nitride, in addition to being a material having excellent mechanical characteristics, is biocompatible [109,110]; also being partially radiolucent it can be observed by radiography.

Figure 2.1: Representative spinal and hip, knee joint implants produced from biomedical silicon nitride. [98] Courtesy Amedica Corporation

2.1.1 Structure of Silicon Nitride

Silicon nitride is a chemical compound made up of two elements, silicon and nitrogen and having the chemical formula Si_3N_4. It is a mineral of white color having a high melting point, is inert and possesses high hardness (8.5 Mohs scale).

It can take three different crystal structures: α, β and γ.

The most common are the α and β which differ only along the c axis in the stacking sequence of the crystallographic planes.

The γ structure, instead, is obtained working at high pressure (15 GPa) and temperatures around 2000 ° C. In this structure, the coordination number of Si is equal to 6, while in the β structure coordination number is equal to 4. In the structure relative to γ- Si_3N_4 two silicon atoms coordinate six nitrogen atoms in octahedral configuration and the third silicon atom binds to four nitrogen atoms to form a tetrahedron. The space group is Fd3m with a = 7.738 Å.

The crystal structures of α- Si_3N_4 and β- Si_3N_4, determined by Hardie and Jack and Turkdogan, are both hexagonal crystal structures constituted by tetrahedrons of Si_3N_4. Each of them is connected to another by a nitrogen atom [111,112].

The space group of the α- Si_3N_4 structure is P31c with cell parameters a = 7.748 pm c = 5.615 Å contains four unit cells of Si_3N_4, while the β- Si_3N_4 space group is P63/I contains two units of Si_3N_4. The cell parameters of the β- Si_3N_4 are a=7.608 Å and c = 2.911 Å.

Their structure can also be thought like stacked planes consisting of alternating silicon atoms to nitrogen atoms in an ABAB sequence in the β- Si_3N_4 and in a ABCDABCD sequence in α- Si_3N_4.

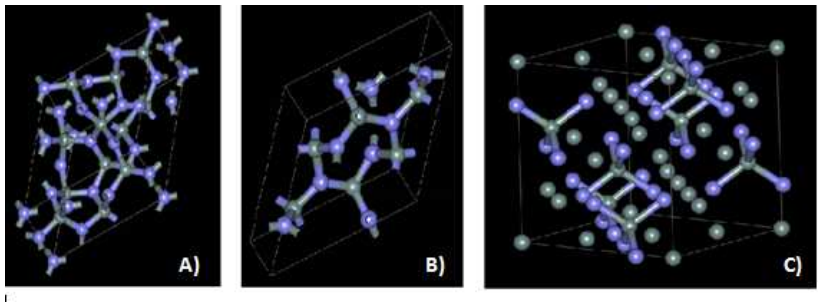

Figure 2.2: Crystalline structure of Si_3N_4-α (A), β- Si_3N_4 (B) and γ- Si_3N_4 (C).

The CDs plans are similar to those AB except for a 180 ° rotation along the crystallographic c axis. The α- Si_3N_4 phase has a mean Si-N bond length equal to 0.1738 nm. The β phase of Si_3N_4 instead provides alternation of atoms of Si and N that forms a

series of layers constituting the continuous channels in the direction c. The average binding length of Si-N in the β phase is equal to 0.173 nm.

2.1.2 Silicon nitride Production Methods

The preparation of silicon nitride requires different essential steps such as the synthesizing and the densification of the powders.

The synthesis of Si3N4 powder leads to the formation of submicrometer grains of variable size between 0.1 µm (fine particles) of up to 10-15 µm (coarse particles).

There are different methods of synthesizing the powders; the oldest is the direct nitridation of silicon powder at temperatures around 1450 ° C in N_2 atmosphere [113,114], the following chemical reaction:

$$3Si + 2\ N_2(g) \rightarrow\ Si_3N_4 \qquad (2.1)$$

Depending on the quality of the starting silicon purity can vary, however, the size of the obtained grains is high.

Another method synthesizing in vapor-phase at high temperatures (~ 1200 ° C) [98,100]:

$$3SiCl_4(g) + 4NH_3(l) \rightarrow Si_3N_4 + 12HCl(g) \qquad (2.2)$$

The result is an amorphous silicon nitride, crystallized after heat treatment (1200-1500°C) [100].

To date, the most widely used method of synthesis is related to the carboreduction in a nitrogen atmosphere.

The starting materials are silica and carbon which are reacted at 1500°C in the presence of nitrogen. A reduction of the silica occurs followed by the nitriding:

$$3SiO_2(g) + 2N_2(g) + 6C \rightarrow Si_3N_4 + 6CO(g) \qquad (2.3)$$

The result is the formation of very fine powders of α-Si3N4.

Subsequently, the obtained powders of silicon nitride are passed to the sintering process. This process is described by the Frenkel's "sphere model" in which two neighboring particles coalesce by diffusion process with the Gibbs free energy reduction:

$$\Delta G_T = \Delta G_v + \Delta G_b + \Delta G_s. \qquad (2.4)$$

There are mainly three different methods of densification:

- Reaction Bonding
- Hot pressure and hot isostatic pressure
- Sintering

The Reaction Bonding consists of a direct nitriding during sintering. This method was developed in 1950 and was mainly used for refractory materials. Later, from 1980, this technique was used to produce turbine engines with hot-zone components consisted entirely from ceramic [100]. In this production method, there is a pre-sintering in an inert atmosphere in order to impart consistency and, subsequently, a nitridation in a nitrogen atmosphere at about 1400 ° C for some days is made. The chemical reaction is:

$$3Si + 2N_2(g) \rightarrow Si_3N_4 \quad (2.5)$$

Silicon nitride obtained by Reaction Bonding (RBSN) has a porosity of 15-25% and presents low mechanical properties. Furthermore, proceeds silicon nitride has a low resistance to bending, equal to 200-300 MPa [98].

The methods of hot pressing and hot isostatic pressing sintering methods are the most used nowadays. In the technique Hot pressing of silicon nitride powders are subjected to pressure of 40 MPa and at temperatures of 1600 ° C; the proportion of additives added is about 5%, and the result obtained has a porosity of about 2%.

Through Hot pressing is possible to obtain only simple shapes, it is, therefore, necessary to carry out subsequent processing on the sample.

The Hot isostatic pressing, instead, differs for the processing performed to the sample because very high pressures have been applied up to 150-200 MPa and the temperature reaches about 2000 ° C. Product obtained is homogeneous and has a perfect density even just adding 1% of additives. Moreover, the sample can have complex shapes without performing further processing.

These treatments lead to an increase in the resistance even if the costs are substantially higher [115].

The third method of densification used is the Sintering in which silicon nitride powders are mixed with a percentage of additives, typically Yttria (Y_2O_3) and alumina (Al_2O_3); the powders are compacted and heated at elevated temperatures above 1700 ° C in N_2 atmosphere with range of pressure between 10-20 MPa. In this method, additives react with the layer of silica SiO_2 formed over the silicon nitride in order to form a liquid phase among the silicon nitride grains and thereby promoting the densification.

On cooling, the material presents a partially crystallized glass phase between the silicon nitride grains [98].

Also, it's possible to sequence two sintering methods, in particular Sintering and the Hot isostatic pressing technology, as to obtain a material with isolated pores and subsequently treated by HIP technique with the aim of obtaining a high resistance at lower costs.

To the powder of Si_3N_4 is possible to add also other additives, in particular metal oxides, which generate a liquid phase appointed to facilitate the transport mechanisms of matter favoring the sintering process.

The powders of α-Si3N4 are covered with a thin layer of silica SiO2 resulting from oxidation which reacts with the additives added to form a liquid phase (~ 1700 ° C) [98].

At the sintering temperature, there is the transition from α phase of silicon nitride to β phase through precipitation.

The result is a structure of β- Si_3N_4 consists of elongated grains presented in a glassy matrix that will constitute the grain boundaries.

Mainly, the most used additives are MgO, Al_2O_3 and Y_2O_3 and are selected according to the thermal properties similar to the predominant phase to avoid the establishment of internal stresses due to thermal expansions [114].

The additives highly influence the material, especially as regards the thermal properties, because the liquid formed in the sintering process and which precipitates at the grain boundaries leads to an increase of the speed of creep and a consequent reduction of the time to creep failure.

Given the presence of an amorphous phase, critical defects for ceramic relate to the grain boundaries. Therefore, it's necessary to find an equilibrium between the needs of sintering and final thermal properties depending by the use.

In addition, additives, favoring the growth of elongated grains, allow a considerable increase of the mechanical strength and hardness thanks to an auto due to a self-reinforcement, which leads to a greater cohesion in the structure.

2.1.3 Properties of Silicon Nitride

Si_3N_4 presents a series of physical properties, including high chemical and mechanical resistance, high hardness and high toughness, much higher than other ceramics, which make it one of the most promising materials in the prosthetic field.

The mechanical properties of Si_3N_4 may also result from the heat treatment used, and by the use of additives to control the composition of a glass phase. This latter is a liquid phase created during the reaction between silicon nitride silica and additives. After cooling the liquid solidifies forming intergranular glass. Silicon nitride, as the other ceramic used in artificial joints is obtained by hot-isostatic pressing which allows to obtain a density closer to the theoretical 100% of the material; the Si_3N_4 has a low density, about 3.2 g / cm3 compared to other important biomaterial commercially available.

Also the size and the morphology of the grains play an important role, since it has been proved that their bimodal structure [116] and their large size [117-119] can increase toughness. The silicon nitride is the only biomedical ceramic having the form of acicular grains. This is given by the irreversible transformation from α- Si_3N_4 phase to β- Si_3N_4 phase growing in anisotropic manner.

As said, silicon nitride is a non-oxide ceramic, however, this material has a flexural strength comparable to that of the oxide materials and is between 800 and 1100 MPa [100]. Moreover, this high resistance, in contrast to other ceramic, doesn't depend on the presence of a metastable phase transformation but on the acicular microstructure.

The progress of an eventual crack continues along a tortuous path at high energy. There are toughening mechanisms such as *bridging grain* and the *pull-out* in the crack that allow a reduction in stress and tensile stresses resulting in increased resistance to crack growth. [120]. *Bridging* mechanism occurs when an elongated not fractured grain supports part of the load applied to the crack exerting a block against the surfaces of fracture [121]. *Pull-out* instead occurs when the elongated grains do not break in correspondence with the propagation plane of the fracture, but above or below it. In this case crack has to make a grain extraction work, consuming a certain amount of energy.

The *pull-out* mechanism is favored for grains having a small diameter and in high temperature tests [121, 122]. If a brittle material is treated, the level of resistance is related to the presence of defects and their dimensions.

Another important parameter which provides a statistical measure of the resistance variation is the Weibull modulus. This is commonly used to characterize the resistance of the experimentally determined materials [123].

The Weibull modulus of silicon nitride is ≥12 and is influenced by the size of the grains, because as seen from the *R-curves* that describes the propagation resistance compared to the length of a crack, the increase in size and number of the grains results in an increase of the resistance and a hardness to fracture [124-126]. Indeed, if there isn't acicular growth of the grains, the mechanical properties of silicon nitride are comparable to those of the ceramic oxides [127,128]; it's important to notice that if the grain size increases, concomitantly, also the related Weibull modulus increases because, they are the strength which limits the flaws [128]. It has a K_{IC}, critical factor of the stress intensity which determines the resistance to fracture of a linear-elastic material, which varies between 4.4 and 15.0 MPa $\cdot$ $m^{1/2}$. This value is due to a structural difference resulting from different microstructures that allow an increase of the hardness as a result also of a joint of a fibrous nature. Indeed, as can be seen from the Figure 2.3, silicon nitride has the strongest *R-curves* compared to other ceramic as a result of the propagation of the crack (up to 8 µM) there is an increase of the resistance [129].

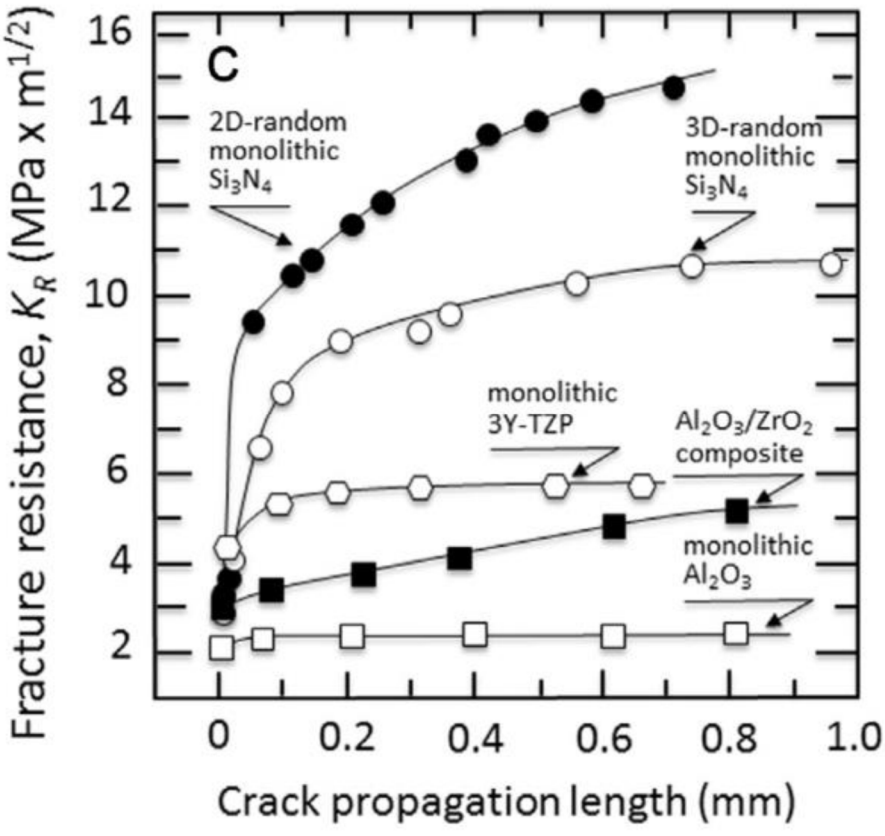

Figure2.3: R-curve of different bioceramics. [129]

As said, the preparation of Si_3N_4 involves a phase transformation from α to β.

With the addition of adjuvants, useful in the sintering process, the α-Si_3N_4 is converted entirely in β-Si_3N_4.

The α phase has a higher free energy, about 30 kJ / mol at 25 ° C, and this makes the inverse transformation completely impossible [130].

It forms a thin layer of silicon dioxide SiO_2 at the grain boundaries and this depends on the percentage of additives present and the degree of impurities of the starting powders [131]. The phase of this material remains stable in a physiological environment which has no impact. Indeed, according to the quantity and the composition of the added components, Si_3N_4 can resist at ambient temperature, from attack by common organic solvents and acids or weak bases [132-133]. This has been verified by a study that has shown how solutions containing NaCl and $CaCl_2$ in contact with silicon nitride, at room temperature, have corrosive power almost negligible [132].

Silicon nitride is strongly influenced by the corrosive working at high temperatures, or in the presence of strong acids or strong alkaline solutions [134-141] (> 300 ° C), high pressures (> 8MPa) [142] or in the presence of molten salts [143,144].

The resistance of this material also depends on the conditions and the corrosive solvent concentration [145,146]. Moreover, in addition to the conditions, also the type of processing may influence the anticorrosive properties of the silicon nitride; an example is given by a study conducted in two different samples of Si_3N_4, the one produced by sintering and the other by high isostatic pressing.

Results have shown as the first sample was more susceptible to attacks of hydrochloric acid HCl, placed in contact with the samples successively, compared to isostatically pressed sample. By treating the samples with HF, corrosive effect of the agent was the opposite of what happened in the samples treated with hydrochloric acid [135].

The corrosion, as in the case of other ceramics, occurs at the level of the grain boundaries; this indicates how a better resistance can be conferred after the crystallization of the intergranular glassy part [138-141].

The silicon nitride has been shown to be a material having a stable phase under hydrothermal conditions. However, on a superficial level, chemical-physical variations can occur through the interaction with biological fluids.

As shown by some studies, through tribological processes, the dissolution of silicon nitride, at the surface level, is mediated by a preferential attack of the Si-N with the

consequent release of ammonia (NH_3) and hydroxylate silicic acid ($Si(OH_4)\cdot xH_2O$ [136, 147,148], a tribochemical wear surface film is formed that allows the reduction of stress on the roughness and the reduction in the rate of wear and the friction level [147,148].

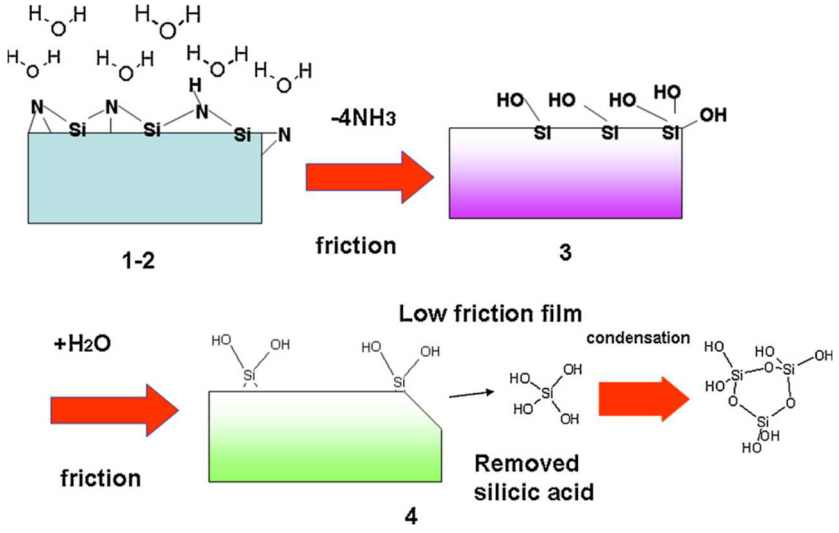

Figure 2.4: Scheme shows the tribochemical wear mechanism of silicon nitride with water. [470]

Moreover, Si_3N_4 in hydrothermal conditions behaves as oxygen scavenger bringing an improvement, especially in polyethylene implants, given by a preventive action against oxidative deterioration [148].

2.1.4 Biocompatibility

Among the appropriate characteristics that make the silicon nitride an excellent material for medical applications, there is definitely the biocompatibility.

However, initially, the first studies carried out in 1980 regarding the biocompatibility of Si_3N_4 didn't bring positive results [149]. Samples tested contained iron and magnesium as adjuvants and, therefore, it was concluded that this material could not hold jobs in the medical field.

In 1989, however, porous silicon nitride obtained through Reaction-bonding was used to check bone growth in vivo and the results showed favorable outcomes [150]. Subsequently, other study groups focused their attention in the characteristics of silicon nitride with a special interest in the clinical field. Among these, Kue et al. in 1999 carried an *in vitro* study using discs that presented a surface machined modified, made smooth (as-polished), and others who had a higher surface roughness (as-sintered). These samples

obtained by means of two different methods of sintering, were placed in contact with the human cell line MG-63 osteoblast. The polished disks presented high levels of osteocalcin and a proliferative capacity greater than non-polished discs [151].

A year later other studies were carried out by Sohrabi et al [152] on silicon nitride samples obtained by Reaction-bounding or by Sintering after Reaction-bounding. The experiments showed that there was cell propagation in both samples but the samples produced by Reaction bonding showed a high presence of interleukin 1L-1β and also of the cytokine TNF-α compared to the other samples. This results indicate that Si_3N_4 is biocompatible and doesn't obstruct the proliferation or induce proinflammatory cytokine expression of cells in vitro.

Also composites of silicon nitride were studied; Si_3N_4 / bioglass complex were analyzed by inherent testing about the wettability in order to obtain the contact angle using water, diiodomethane and a simulated body fluid (SBF) [153]. The results showed that the composite assumed hydrophilic behavior because the contact angle analyzed is lower than that of other conventional ceramics such as HA, βTCP and bioglass. This hydrophilic behavior can lead to an increase of cells adhesion to the Si_3N_4 than other materials which have hydrophobic behavior on the surface.

Even the use of additives such as Ytterbium, yttrium and aluminum oxides in the silicon nitride have been tested and it is seen that the derivative material hasn't cytotoxic activity [154]. In 2004 comparative tests were made using silicon nitride, alumina and titania to check the cytotoxicity, the adhesion, the cell viability and also the morphology. These tests were made *in vitro* using an osteoblasts cell line of mouse (the L929-cell). They received various good results especially in those samples of polished silicon nitride in which the cell growth was better promoted. [155]

Other studies showed how the silicon nitride was also biocompatible with other cell types. Cappi et al. showed as samples treated with human mesenchymal cells had non-toxic nature, encouraging growth and differentiation into osteoblasts [156].

In 2004 results were published relating to a research concerning the use of the intervertebral spacers of Si_3N_4 effected in a period of time long 15 years and addictive thirty patients presenting degeneration of the spinal cord.

For this research were used 10 subjects like control, tested with autogenous bone; after a year, fourteen patients had a significant decrease in pain while after five years almost all patients had a reduction in pain along with an increase of implant resistance [157].

In 2006 mini-fixing systems were employed to induce osteosynthesis in piglets. The materials, miniplates and the screws were composed of silicon nitride and were reliable in the absence of movements or problems concerning the implant, or fracture. However not all the samples presented direct contact with the bone and consequently a complete bone healing [158]. Another test *in vivo* was made from Guedes et al. using ceramic of silicon nitride implanted in rabbit tibias for about 8 weeks. The histological analyzes of the samples were made and results have shown that the process of osseointegration has taken place throughout the period without any adverse reaction present around the implant [159].

Another test *in vivo* was carried out by Anderson and Olsen who employed silicon nitride with a spongy non-absorbable structure and developed a cylindrical implants inserted in the medial femoral condyle of sheep [160].

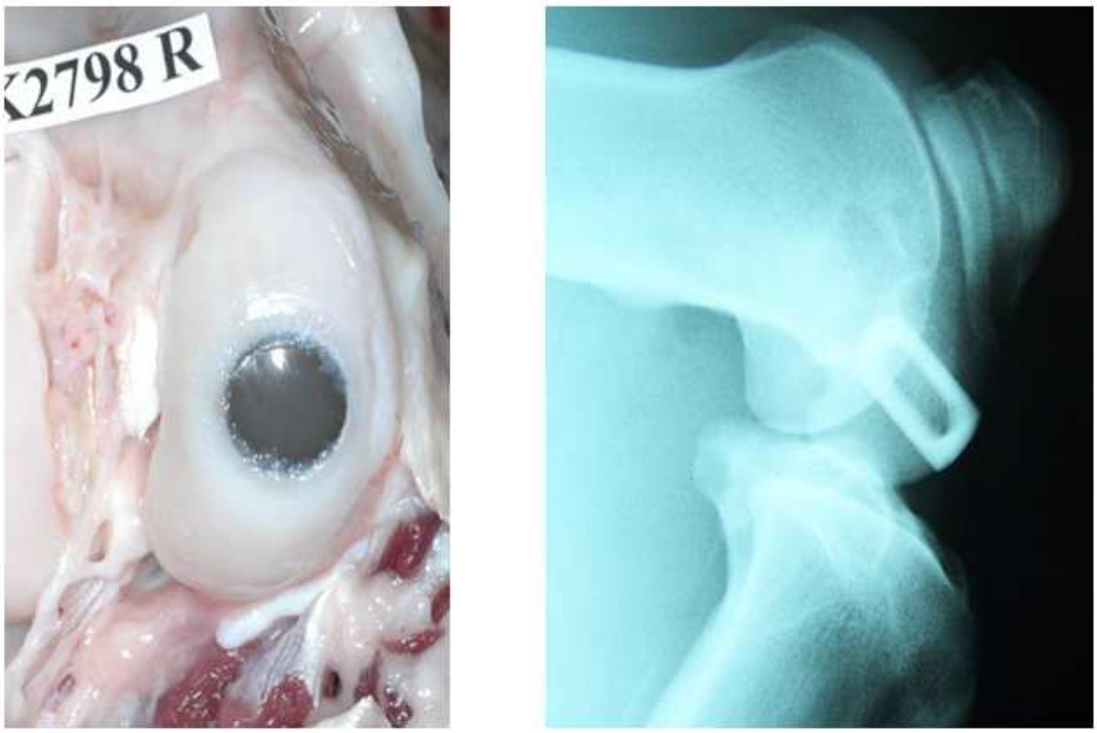

Figure 2.5: In vivo femoral condyle implant in ovine. Courtesy Amedica Corporation

The implants were retrieved from the animals after 3 and 6 months and were analyzed in order to verify the bone growth [160].

Also monolithic materials and an electroconductive composite Si_3N_4/TiN were developed which didn't show toxic activity and could be shaped into complex geometries [161]. These materials were also the subject of study in terms of wettability in aqueous media

or physiological solutions. Their stability and the wear resistance in conditions similar to the hip prosthesis have been studied. The results showed low contact angles compared to the initial ones, signaling increased hydrophilicity which can lead greater cell adhesion [162].

2.1.5 Si(Y)AlON

The market of the prosthesis is dominated (more than 90% of the products) by ceramics containing alumina despite other ceramics, such as silicon nitride, have better properties for certain applications. The reason of this choice can be found in the excessive cost of the production of pure silicon nitride and, therefore, a new solid solution based on the same structure of silicon nitride has been studied and produced [163]. The SiAlON, silicon oxynitride and aluminum, is a ceramic which is formed when in the structure of the silicon nitride Si_6N_8 oxygen is replaced to the nitrogen and at the same time, the aluminum takes over to silicon maintaining the neutrality of the charge [164].

This material has an isomorphic shape, in particular, there are three basic forms which are isostructural with the α and β forms of silicon nitride and the silicon oxynitride. The most common form of SiAlON is the β form as in the case of silicon nitride.

The composition of the ceramic of β-SiAlON is $SI_{6-x}Al_xO_xN_{8-x}$, with the value of x which can vary in the range from 0 to 4.2 [165, 166]. Reported in the 1971 by Oyama [167,168] and successively in 1972 by Jack and Wilson, SiAlON presents a lot of very important properties and features like a high chemical and oxidation resistance. This material is easier to sinter thanks to the presence of aluminum that reduces the eutectic temperature by 200° C, being easier forming grain boundary glasses [164].

Microstructural characteristics of SiAlON depend by the nature of Si_3N_4 before the processes, the conditions of sintering and also the additives used. As written before, Si_3N_4 exists in two forms, α and β; α-Si_3N_4 has higher reactivity than β-Si_3N_4 and during the sintering process there is a transformation from α to β and the formation of elongated grains [169-171]. If it's used α-Si_3N_4 as the starting powder, it's more difficult to obtain the formation of elongated grains and their densification [172].

The working conditions and the additives used have an important role during the process of formation of SiAlON, especially on the growth of the grains [173, 174].

The transformation during sintering process forms α-SiAlON to β-SiAlON is fully reversible differently from the silicon nitride transformation. The morphologies of α-SiAlON and β-SiAlON are different because β-SiAlON consists of elongated prismatic grains, while in α-SiAlON grains are small and equiaxed.

The material's mechanical and thermal properties depend on the ratio of the two polymorphs (α-SiAlON and β-SiAlON) and the presence of sintering aids like rare earth oxides and the different treatment and procedures that can control the composition [175, 176]. The quantity of additives initially influences the chemistry and the amount of the glass phase changing different properties of the material as fracture toughness, strength at high and ambient temperature, creep and oxidation resistance [177,178].

Also the thickness of the grain-boundary and the layers depend by the amounts of additives [179,180]. Like the quantity, also the chemical composition can shape the strength even if debonding phenomenon can lead to loss of it [181].

Silicon nitride samples can be treated with different ratios of Y_2O_3 and Al_2O_3. Different percentage of these additives can vary the behavior of the material; in particular, it's possible to see that more elongated rod-like crystals have better resistance to crack propagation, so if the composition of the grain boundary changes, the morphology and the ratio of the grain vary as the time and temperature of sintering [174,179].

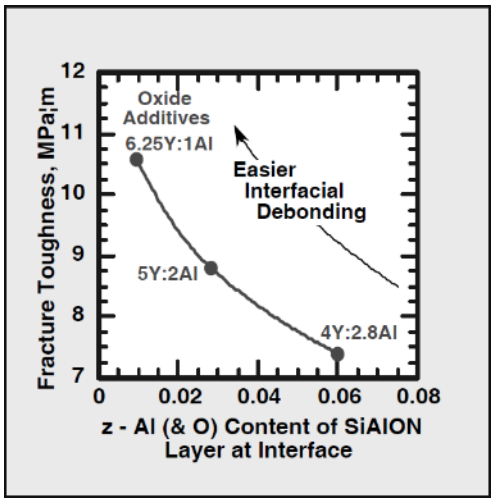

Figure 2.6: Fracture toughness v. intergranular glass composition. [179]

Indeed, in a comparison between silicon nitride with low Y:Al ratios and silicon nitride samples with high Y:Al ratios, the latter show an intergranular increased fracture. this is due because different ratios of Y:Al can influence the atomic bonding structure across the silicon nitride intergranular glass interface. Furthermore, inducing different contents of Al and O in the growth region of elongated grains, it's possible to modify the composition of the glassy phase [179]. The figure 2.6 shows how the decrease of Al can bring an improved fracture resistance by activation of toughening mechanisms.

2.1.6 Surface chemistry of the Silicon Nitride

On its surface, silicon nitride develops a layer of SiO_2 because the material possesses a thermodynamic instability in oxidizing or moist environment [182]. This layer has been measured, and can be 3-5 nm thick [183] and this formation is due by the following reactions [184]:

$$Si_3N_{4(s)} + 3O_{2(g)} \rightarrow 3SiO_{2(s)} + 2N_{2(g)} \quad (2.6)$$

$$Si_3N_{4(s)} + 6H_2O_{(l)} \rightarrow 3SiO_{2(s)} + 2NH_{3(g)} \quad (2.7)$$

However, these reactions don't describe exactly the surface chemistry of silicon nitride because the situation is more complex, in particular the composition near the surface contains also Si-N-O and Si-O bonds [183, 185-189]. There is a transitional process, when Si-N bonds are exposed to air or moisture, a reaction starts to form charged functional groups like $Si\text{-}NH_3^+$, $Si\text{-}OH_2^+$, $Si\text{-}O^-$, and also neutral functional groups like $Si\text{-}NH_2$, Si-OH [186, 190-193].

About the neutral functional groups, the equations that describe the reactions are [186, 191] :

$$Si_3N_{(s)} + 2H_2O_{(l)} \rightarrow Si\text{-}NH_{2(s)} + 2Si\text{-}OH_{(s)} \quad (2.8)$$

$$Si\text{-}NH_{2(s)} + H_2O_{(l)} \rightarrow Si\text{-}OH_{(s)} + NH_{3(g)} \quad (2.9)$$

In an aqueous environment, the two species, $Si\text{-}NH_2$ and $Si\text{-}OH_{(s)}$, can dissociate following these reactions [191, 194, 186]:

$$Si\text{-}OH_{2(s)}^+ \leftrightarrow Si\text{-}OH_{(s)} + H_{(aq)}^+ \quad (2.10)$$

$$Si\text{-}OH_{(s)} \leftrightarrow Si\text{-}O^- + H_{(aq)}^+ \quad (2.11)$$

$$Si\text{-}NH_{3(s)}^+ \leftrightarrow Si\text{-}NH_{2(s)} + H_{(aq)}^+ \quad (2.12)$$

The reaction describing the protonation of the silanol group $Si\text{-}OH_{2(s)}^+$ is possible only in highly aicidic environment whereas, the other two reactions are possible at homeostatic pH. Through the change in pH of the system, it's possible to drive the reactions, and is possible to analyze the isoeletric point of the material with zero net charge at the surface. The isoelectric point (IEP) is an indicator of an equal balance of negative-charges and

positive-charges on the surface of a material [187]. If IEP is lower than pH of the environment, the surface of the material will expose net negative charge, while if IEP is highest compared to pH, the surface's net charge will be positive.

The IEP of a sample of pure silicon nitride is 9.3-9.7, and this value is due by the presence of a high amine groups concentration on the surface [187,197] and this feature assumes that the surface has a negative charge.

Instead, SiO_2 owns a low IPE (2-3) and so thanks to the variation of IPE, it is possible to analyze and estimate the thickness of the oxide layer and the balance between amine and silanol groups on the surface.

However, it is more important to consider also the influence and the presence of chemical additives like Y_2O_3 and Al_2O_3 because these can react with silion nitride and with superficial silicon dioxide to form a liquid phase. After cooling, this liquid solidifies and there is the formation of an intergranular glass or Si(Y)AlON, crystalline silicon yttrium aluminum oxynitride. These sintering aids can bring other modifications on the surface with the formation of hydrolyzed Al-OH and Y-OH functional groups especially in regions where grain boundaries intersect the exposed surface.

The reactions are similar to the reaction that describes the behavior of SiOH as follows [195]:

$$\text{Y-OH}^{+}_{2(s)} \leftrightarrow \text{Y-OH}_{(s)} + \text{H}^{+}_{(aq)} \quad (2.13)$$

$$\text{Y-OH}_{(s)} \leftrightarrow \text{Y-O}^{-} + \text{H}^{+}_{(aq)} \quad (2.14)$$

$$\text{Al-OH}^{+}_{2(s)} \leftrightarrow \text{Al-OH}_{(s)} + \text{H}^{+}_{(aq)} \quad (2.15)$$

$$\text{Al-OH}_{(s)} \leftrightarrow \text{Al-O}^{-} + \text{H}^{+}_{(aq)} \quad (2.16)$$

IEP for the additives is ~8-9 for Yttria [198] and ~9 for Allumina [199] while IEP for a silica-rich silicon oxynitride is 6-7 [200]. The combination of these compounds influences the chemistry of the surface and this permit immediately the development of a surface charge when placed in an environment (i.e. biological environment) where Si_3N_4 is covered by an absorption layer. An important rule is played by topography of the material that can help about the formation of this layer of ions and proteins, permitting the adhesion of cells both *in vivo* and *in vitro* [201].

Surface composition has an important effect like using hydroxylated surfaces of TiO_2, Ta_2O_5 and SiO_2 where it has been shown how these surface can induce the formation of apatite at biological condition of pH both *in vivo* and *in vitro* [202, 203] through a

mechanism on the surface of the material and concerns the exhibition of negative charge at homeostatic pH.

2.2 Samples

2.2.1 Silicon Nitride and surface treatments

Silicon Nitride samples used in this thesis have been produced by Amedica Corp., (Salt Lake City, UT), using conventional ceramic fabrication techniques. Si_3N_4 powder (Ube SN E-10, Ube City, Japan) has been mixed with Y_2O_3 (Grade C, H. C. Starck, Munich, Germany) and Al_2O_3 (SA8-DBM, Baikowski/Malakoff, Charlotte, NC) used as additives and sintering aids. The samples have been sintered in nitrogen atmosphere at a temperature 1700°C and further densified by Hot-isostatic pressing at 1650°C and in N_2 gas pressure of >200MPa. The resulting Si_3N_4 showed a two-phase microstructure: a anisotropic β-Si_3N_4 grains separated by thin (<2 nm) grain boundaries constituted by an amorphous or crystalline yttrium aluminum oxynitride or Si(Y)AlON, respectively [204]. The samples can be divided into two groups. One group designated as “as-fired” which has untreated surface. The second group is labelled “polished” because the surface has been lapped using 6 µm diamond (Engis, Wheeling, IL) on a lapping machine (Lapmaster, Mt. Prospect, IL), and subsequently polished using colloidal silica (Leco, St. Joseph, MI). The samples have then divided into sub-groups and subjected to the thermal and chemical treatments [191]:

- Wet Chemical Etching; this treatments, made using hydrofluoric acid (HF), should maximize the concentration of amine groups at the surface by etching away the passivation layer of SiO_2 [205]. Thus the surface composition has been biased to the nitride end of the nitride-oxide spectrum;
- Nitrogen Heat Treatment: this heat treatment can be considered as a potential alternative to the HF etching treatment. Re-exposing Si_3N_4 to a N_2 atmosphere at high temperatures, the density of surface amines relative to hydroxyl groups might increases;

- Oxidation Treatment: this treatment was employed to oxidize, completely, the surface, yielding the maximum concentration of hydroxyl groups and pushing the surface composition as far to the oxide end of the nitride-oxide spectrum.

Another sub-group has been subjected to a glazing treatment using slurry which contains:

- SiO_2 (~.05 micron): 48.8 mol%
- Si_3N_4 (~95% alpha, SNE-10, <0.5 micron): 2.4 mol%
- Y_2O_3 (<0.1 micron, HC Starck): 28 mol%
- Al_2O_3 (theta, ~50-100nm, Sasol APA-0.2): 4.8%
- AlN (~0.5 micron, HC Starck Grade C): 16%

A layer on the surface has been formed and the samples have been characterized before the cellular treatment to understand the surface chemistry and structure.
All the samples have been analyzed and tested with different cells and after characterization.
In the treatment with osteosarcoma line cells (SaOS-2) the samples employed are “as-fired”, the “glazed” samples (as-fired and polished) and Ti alloy and Al_2O_3, used as control.
In the treatment with PDLSCs cell line the samples used are “polished” and control (Ti alloy and Al_2O_3); no “glazed” samples have been tested.

2.3 Methods: Raman spectroscopy

2.3.1 Introduction to Raman spectroscopy

Raman spectroscopy is one of the main spectroscopic technique used to study vibrational, rotational and other low-frequency modes in a system in chemistry or in condensed matter physics [206].

This technique permits to identify molecules and it's used to provide information about physical forms and chemical structures thanks to a specific spectral pattern, called "fingerprint" which is also used to estimate, quantitatively or semi-quantitatively, the amount of a substance in the sample.

Raman spectroscopy can be used to study solid, liquid and gaseous samples.

The phenomenon on which this technique relies is known as Raman scattering, an inelastic scattering of a monochromatic light.

The frequency of the monochromatic light changes upon interaction with the sample. Photons of the laser source are absorbed by the sample and then reemitted at different frequencies shifted up or down compared with original monochromatic frequency. This shift provides information about vibrational, rotational and other low frequency transitions in molecules.

Raman scattering has been foretelled initially in 1923 by Adolf Smekal and observed by Raman in 1928 [207,208]. First experiments used concentrated sunlight, a lens to collect the scattered radiation and filters to show the existence of scattered radiation.

The results of these tests were based on direct observation of the color changes in the diffuse light [209]. Following experiments provided spectra of different liquids obtained using mercury lamps and spectrographs until, in 1960, a great improvement in the development of visible laser occurred with the introduction of such a monochromatic source, laser source, coherent, with a very narrow beam and high intensity. Since then, very small volumes of solids, liquids and gases samples can be analyzed obtaining a Raman spectrum also in a variety conditions.

This spectroscopic technique has been further improved thanks to microelectronics that led to the introduction of stepper motors and computerized techniques. These latter allow the counting of the photons and the acquisition and the process data. A big step forward

was done with the inclusion of the CCD, charge couple device, that permits to record a complete Raman spectrum in less than a second [210].
Main advantages of this technique are the capabilities to focus a very intense light onto a sample with small size and the wide range of available exciting wavelength, which can mitigate or even permits the suppression of undesired fluorescence emission derived from certain samples. Indeed, now it's possible to select the the laser beam based on the sample to investigate, varying the wavelength from the infra-red to the ultra violet.
Raman spectroscopy can be used in numerous applications in research activities for analysis both qualitative and quantitative of inorganic, and organic system [211].
In the biological field the use of this technique has brought many advantages. First, there is no complex handling during the preparation, the use of aqueous solutions doesn't not affect the output and it's possible to obtain precise information on the sample.
It is therefore possible to use this technique to analyze some materials as artificial prosthesis studying their behavior when subjected to loads and the interactions with the body. There are numerous cases in the literature that illustrate how Raman spectroscopy can be used to answer key questions of medical interest, science and technology. Through an approach of spatial and spectral deconvolution, it's possible to perform a non-destructive test verifying the reliability of a biomaterial.
Surface analysis, can be carried out in materials that have undergone a phase transition following exposure to a biological environment. These analyses can be done using Raman confocal, technique which deletes out-of-focus light adding a spatial pinhole placed at the confocal plane of the lens [212]. So Raman spectroscopy is used to calculate the residual stress within each phase, oxidation and other changes related to the combined effect of biological environment and load.

2.3.2 Basic Theory: scattering process

When a monochromatic light interacts with the matter, most of it is scattered elastically, without loss of energy while a part of it can be scattered elastically. This latter can carry with it important information about the structure of the matter.
If a photon, in the light, has certain energy compared with the energy gap between ground state and excited state of a molecule, this photon can be adsorbed and so the molecule

promotes to the higher excited energy state. This change of energy, in absorption spectroscopy, corresponds to an energy loss of radiation from the light detected, but it's also possible that the photon can scatter from a molecule after the interaction [213].
Scattering spectroscopic technique, as written before, can give some informations about the materials and molecules analyzed, like size and its distribution.
Furthermore, it's possible to do molecular identification. For this latter, Raman scattering spectroscopy is the main technique used. Like Raman, there are other spectroscopic technique that used the process of adsorption like X-ray absorption spectroscopy, NMR, acoustic spectroscopy and FTIR. But the way in which radiation is employed between FTIR and Raman spectroscopy is different because in infrared spectroscopy; indeed, where the frequency of incident radiation matches that of a vibration, there is the passage of state. Infrared absorption involves direct excitation of the molecule from a low energy state to an excited state by a photon of exactly the energy difference between them. While Raman scattering uses much higher energy radiation and measures the difference in energy between the two different states by subtracting the energy of the scattered photon from that of the incident beam.
Another important technique based on the absorption process is SERS, Scattering Raman Surface-enhanced, technique which gives an enhancement of up to about 10^6 in scattering efficiency over normal Raman scattering.

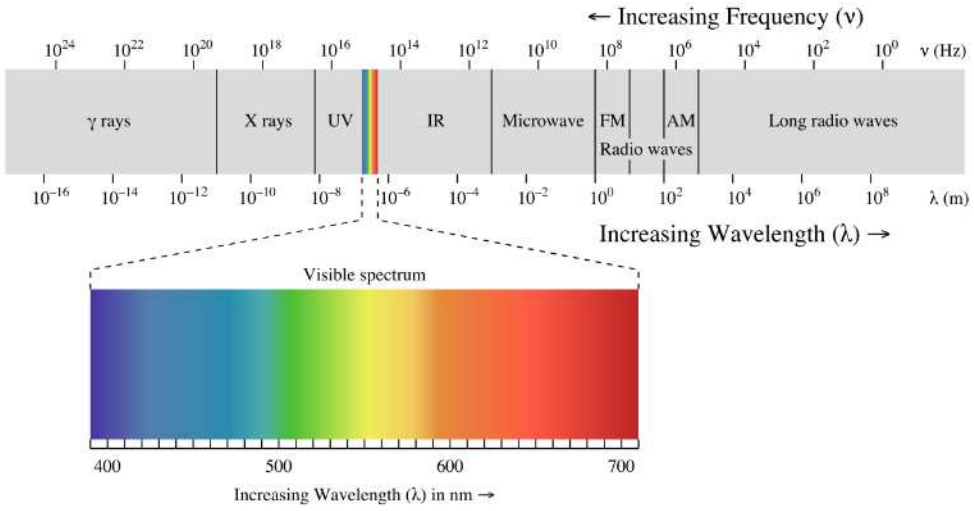

Figure2.7: The electromagnetic spectrum showing the wavelength associated to different types of radiation.

In the figure 2.7, the electromagnetic spectrum, a wavelength range of some used type of radiation and associate to spectroscopic technique, is indicated. This range can be divided

different spectral regions characterized in wavelength and frequency. Radiation is characterized by wavelength (λ), but in spectroscopy, usually discussing in terms of energy, it's useful to introduce frequency (ν) and wavenumber (ϖ) scales. Between these parameters, there is a correlation, given by the following equations [214,215]:

$$\lambda = c / \nu \tag{2.17}$$

$$\varpi = \nu / c = 1 / \lambda \tag{2.18}$$

$$\nu = \Delta E / h \qquad \Delta E = h\nu \tag{2.19}$$

Raman spectroscopy employs a single frequency of radiation to irradiate the matter and this radiation, detected after inelastic scattering, has different energy from the incident one.

In Raman scattering, light interacts with the molecule, polarizes the cloud of electrons around the nuclei and forms a "*virtual state*". This latter, is not a stationary state and does not correspond to a well-defined value of the energy. Furthermore, it is a short-lived state, not stable so the photon is quickly re-radiated. The spectroscope detects the nuclear motion caused by the change of energy. But if the nuclear motion is not induced and the electron cloud distortion involves only scattering, the change of frequencies will not be present. This process is an elastic scattering called *Rayleigh scattering* and photon maintains the incident energy. This is the dominant process, while, if nuclear motion is induced during the scattering process, energy will be transferred either from incident photon to the molecule or from molecule to another photon scattered. In this case the process is inelastic and it's called *Raman scattering*. In this process the scattered photons possess a totally different energy from that to the incident photon.

This scattering process can be divided in *Stokes scattering* if photons undergo a loss of energy, and *anti-Stoke scattering* if photons earn energy.

An exemplary of the Raman spectrum can be seen in Figure 2.9 which shows the intense peak, related to the Rayleigh scattering in the center, that shows no shift in frequency, and the Stokes and anti-Stokes bands with opposing movements.

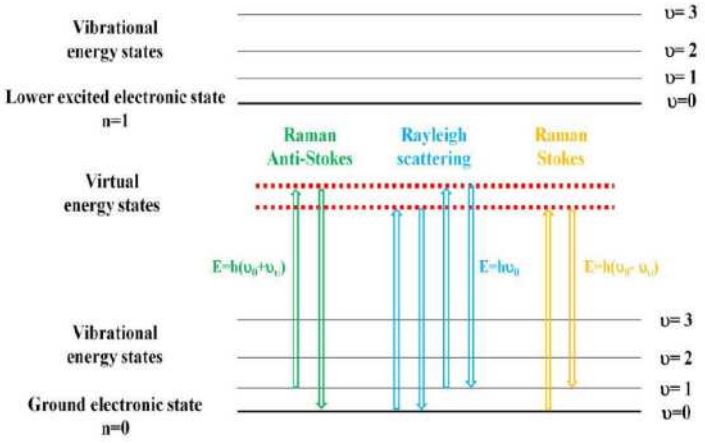

Figure 2.8: Scheme about different energy states describing anti-Stokes, Rayleigh and Stokes scattering.

At room temperature, a lot of molecules are present in the lowest energy vibrational level. The virtual states of these molecules are created when laser interacts with the electrons and causes polarization and the energy of these states is determinated by the frequency of the light source used. The most intense process will be the Rayleigh scattering since most photons scatters elastically, and as written before, it doesn't lead to changes of energy. Consequently, the light returns to the same energy state.

Raman scattering process describes instead an adsorption of energy by the molecule with a promotion from the ground vibrational state to a higher energy excited vibrational state. This phenomenon is called Stokes scattering. But it's also possible that some molecules can be present in an excited state, due to thermal energy and not in the ground state. This is the case of an anti-Stokes scattering.

The basic processes are shown in the Figure 2.8, and the relative intensities depend on the population of the various states of the molecule.

Stokes and anti-Stokes scattering differ from Rayleigh scattering of a quantity $\Delta E = h\nu$, (the sign changes and it's positive in scattering Stokes and it's negative in scattering anti-Stokes) and this corresponds to the energy gap between the first vibrational level and ground state.

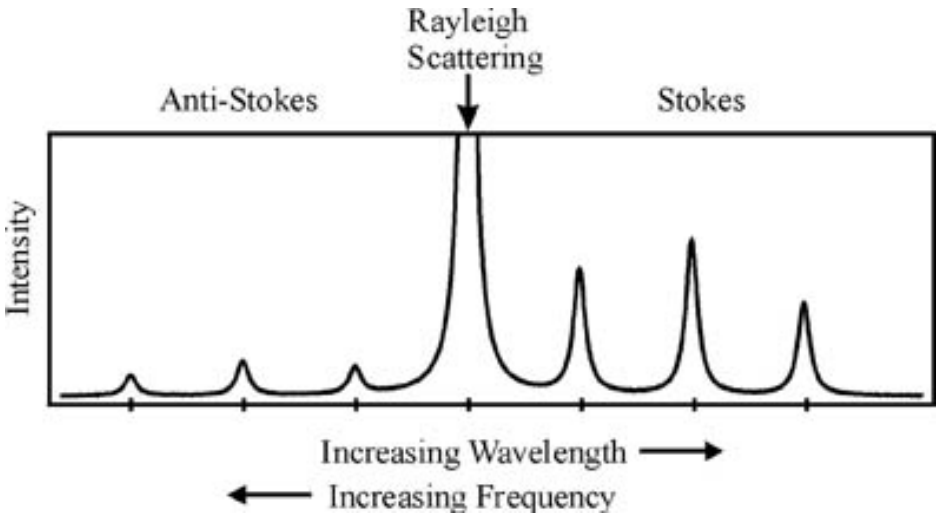

Figure 2.9: Example of Raman spectrum with the different bands related to scattering Rayleigh, Stokes and anti-Stokes.

The ratio of the intensities between anti-Stokes and Stokes depends and increases with the temperature, because there is an increasing of the number of molecules in the vibrational excited state if thermal motion grows. This can be calculated from the Boltzmann equation,

$$\frac{N_n}{N_m} = \frac{g_n}{g_m} \exp\left[\frac{-(E_n - E_m)}{kT}\right] \qquad (2.20$$

Where N_n and N_m are the numbers of molecules in the excited vibrational energy level (n) and in the ground vibrational energy level (m), g is the degeneracy of the levels n and m (this indicates if there are different molecules at the same energy state), $E_n - E_m$ is the difference in energy between the two energy levels and k is the Boltzmann's constant ($1{,}3807 \times 10^{-23}$ JK^{-1}).

At room temperature, as written before, there are a lot of molecule present in the ground state energy level than the excited energy state, and this indicate that anti-Stoke line is much weak than the Stroke line. Another important thing regards the molecule's polarizability.

Polarizability measures the case with which the electron cloud around the molecule can be distorted. The selection rule asserts that Raman scattering occurs because a molecular vibration can variate the polarizability. This is described by these formulas:

$$\mu = \alpha E \tag{2.21}$$

$$\left(\frac{d\alpha}{dq}\right)_{q_0} \neq 0 \tag{2.22}$$

where μ is the induced dipole moment, α is the polarizability of the molecule, E is the electric field, q_o is the coordinate of the nuclear displacement q (normal coordinate of vibration).

The change of polarizability is described by its derivative, dα /dq that have to be different from zero; this means that the charge distribution of the molecule may be distorted by an electric field E of a certain quantity q. Polarizability increases in big atoms because the volume occupied by the electrons enhances, the size grows and the binding of the electrons with the nucleus decreases in intensity.

On the contrary, in small atoms, the electrons are strongly bund to the nucleus.

If a molecule is polarizable, it is also a Raman active molecule. Among these molecules are H_2O, CO_2, alkanes, CS_2 and many others. In the figure 2.10 vibrational modes and the changing of polarizability ellipsoids is shown. All modes are found to be Raman active, and this is generally true for all asymmetric top molecules like water. It's possible to see how if $q = 0$ there is no variation of the polarizability.

Molecules more polarizable are alkanes, more than alkenes and arenes thanks to their high reactivity.

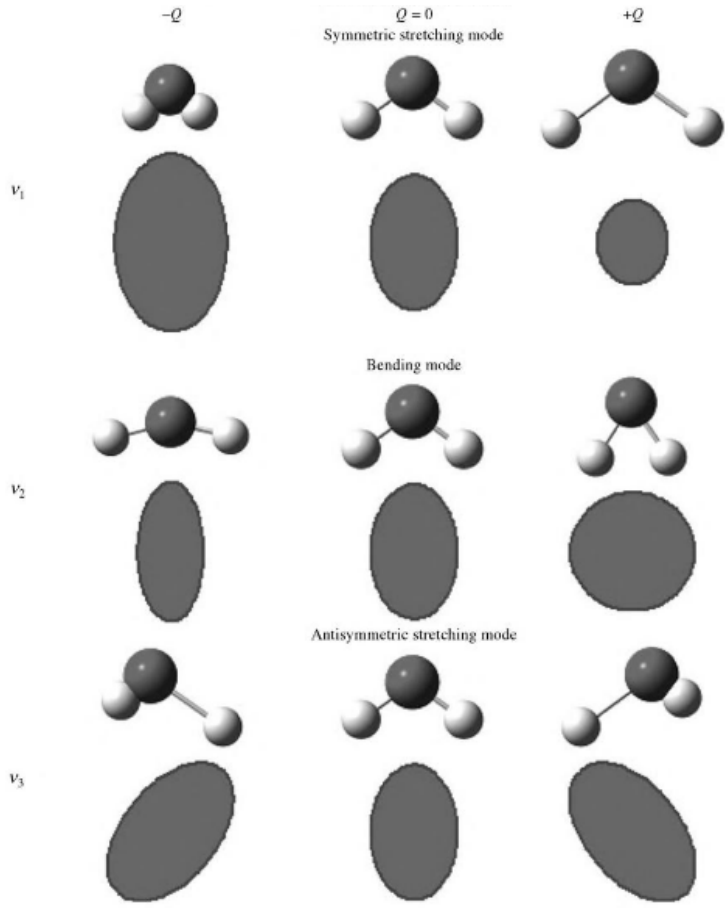

Figure2.10: changes in the polarizability ellipsoid in water molecules.

2.3.3 Hydroxyapatite structure and Raman Spectra

Apatite is a group of minerals having the general formula $Ca_{10}(PO_4)_6X_2$ with the final group being Cl^-, F^-, Br^- or OH^- [216,17]. The last group regards the hydroxyapatite (HA) that is the most relevant and common mineral studied in biology and material sciences. HA can be found in teeth and bones because it's the naturally occurring form of calcium apatite [218]. HA has a hexagonal crystal structure, with 44 atoms per unit cell and a stoichiometric calcium-to-phosphate ratio of 1.67 [219]. Hydroxyapatite belongs to the $P6_3/m$ (dypiramidal) [220], and the structure is constituted by PO_4 tetrahedral in which the two atoms of oxygen are placed on the horizontal plane compared to the axis c and the other two located on the axis which is parallel to the direction c. The unit cell dimensions of HA are a=b= 9.432 Å and c= 6.881 Å (α=β=90° and γ= 120°) [221-223]. Tetrahedrons are arranged in two levels (placed at ¼ and ¾ of the unit cell) and distributed

forming two types of channels which are perpendicular to the basal plane [224]. One of them contains calcium ions and it's called Ca (I) or columnar Ca. In every unit cell there are two channels with two calcium ions. The other channel is larger than the previous one and surrounded by oxygen and calcium atoms. These latter are denominated Ca (II) of the axis of screwing (screw-axis). Figure 2.11 shows the HA structure:

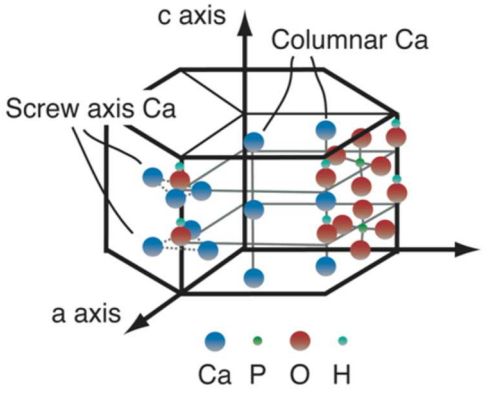

Figure 2.11: structure of hexagonal hydroxyapatite.

The main symmetry elements of HA are:

- One plane of symmetry perpendicular to the z-axis (at z = $^1/_4$);
- One roto-traslation axis (screw-axis) 6_3 to the origin of the cell parallel to the *c*-axis and associated with an inversion center to (0,0,0);
- Three axes of rotation-translation 2_1 parallel to the axis c at the center of the unit cell at ($^1/_2$, ½, z), ($^1/_2$, 0, z) and (0,$^1/_2$, z). The axes are associated respectively with the inversion centers ($^1/_2$, $^1/_2$, 0), ($^1/_2$, 0, 0) and (0, $^1/_2$, 0).
- Four of improper rotation axes 6 parallel to the axis c at ($^1/_3$, $^2/_3$, z) and ($^2/_3$, $^1/_3$, z).

There is a correlation between the symmetry of the lattice and the overall vibrational behavior of hydroxyapatite; 33 Raman modes in addition to 22 active infrared modes can be found and represented by the following representation [219,220,225]:

$$\Gamma = 22A + 22B + 22E_1 + 22E_2 \qquad (2.23)$$

Bands that originate from internal vibrations of phosphate ions (PO_4^{3-}), dominate the Raman spectrum of HA. (PO_4^{3-}) ion has nine normal vibrational mode and T_d symmetry (figure 2.12) [219, 225]:

- Symmetric stretching of the P-O bond, ν_1;
- Bending doubly degenerate O-P-O, ν_2;

- Asymmetric stretching three-time degenerate P-O, ν_3;
- Bending asymmetric three times degenerate O-P-O, ν_4.

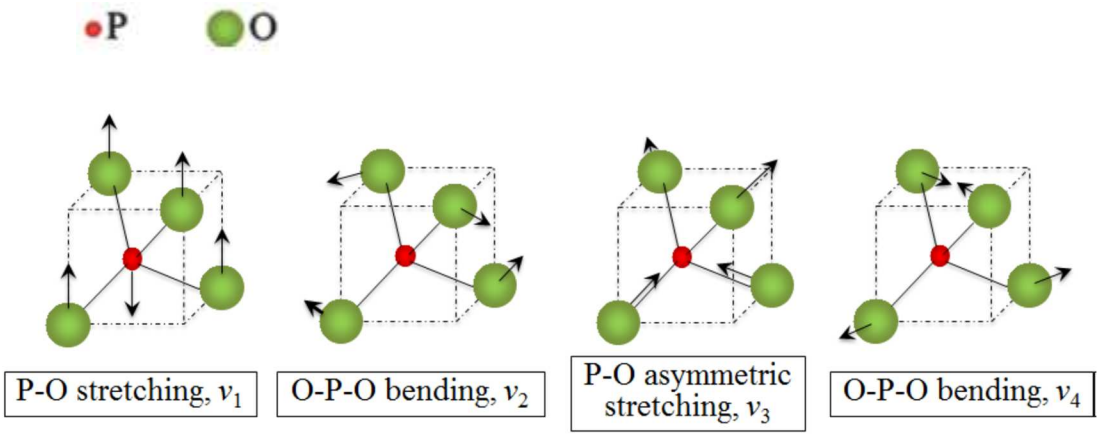

Figure 2.12: vibrational modes of the PO_4^{3-} ion.

In the next figure instead (figure 2.13), two Raman spectra of hydroxyapatite are shows in which there are the four spectral regions ν_1 ~ ν_4. The Raman spectra have been performed both with a cross polarization both parallel. In both polarizations it can be observed at around 960 cm^{-1} Raman band corresponding to the most intense peak of the symmetrical stretching of the P-O bond (ν_1).

The two band located at about 432 and 442 cm^{-1} belong to the ν_2 region related to the bending of O-P-O. The bands included in ν_3 group are located at higher frequencies and that is around 1025, 1047 and 1087 cm^{-1}. Finally, the bands belonging to the vibrational modes ν_4 are about 579, 592 and 608 cm^{-1}.

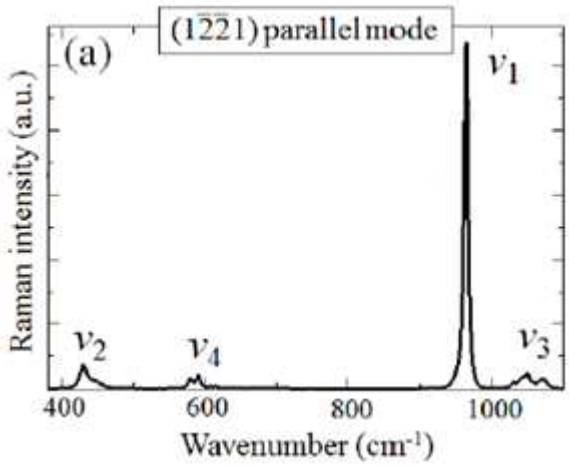

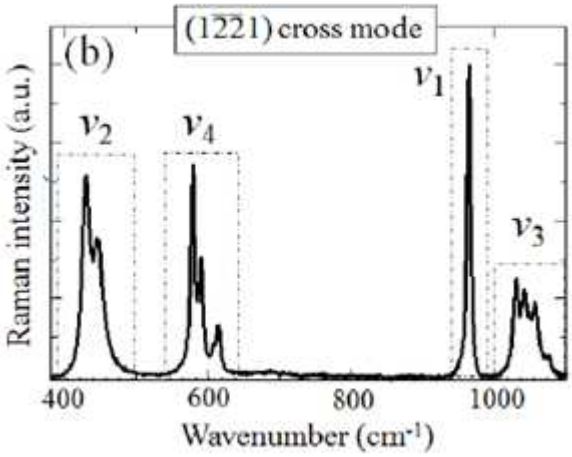

Figure 2.13: Raman spectrum of a single crystal obtained from plane (1221) with cross and parallel polarization.

It's important to mention that fluoride (F^-), chloride (Cl^-) or carbonate (CO_3^{2-}) ions can replace OH^- ions and the result is the formation of three different minerals: fluoroapatite, chloroapatite and carbonateapatite.

In the synthetic hydroxyapatite, for example, there is the substitution of OH^- (type A) or PO_4^{3-} (type B) with CO_3^{2-} in the lattice which creates an important impurity [226].

The band related to the symmetric stretching ν_1 of CO_3^{2-} is the most intense like the symmetric stretching ν_1 of PO_4^{3-} of HA spectrum. Spectral variations especially in the ν_3 PO_4^{3-} region have been shown in Raman studies on carbonated apatites [227]. Two main bands have been reported at ~1070 and 1046 cm^{-1} and two distinct wavenumbers for the ν_1 carbonate mode have been suggested to depend on whether substitution is of type A or B at 1108 and 1070 cm^{-1}, respectively [228]. These substitutions induce the generation of vacancies and distortions in the lattice.

2.3.4 Instrumentation

Raman spectroscope consists of five main components:

- A source of monochromatic light;
- A microscope device;
- A spectrograph;
- A detector;
- A software.

There are also other important components, among them, the “notch filter” that cuts off the elastic Rayleigh scattering of the laser and the “optical polarizer” whose rule is to collect the polarized Raman light. The typical source of a Raman spectroscope is a laser with a specific wavelength which, depending by the application, can vary from ultraviolet to near infrared. The light beam from the source is focused on the “notch filter” which reflects it toward the sample with a correct angle.

Figure 2.14: Overview of the T64000 spectrophotometer.

The scattered Raman radiation is direct back to the filter and the its structure allows the passage of only Raman radiation. This latter is directed toward a monochromator which uses a grating to diffract the beam with very narrow band wavelength. Each wavelength is caught by a detector, in general, a CCD detector (charged-coupled device) which counts the photons and converts the information into an electric signal processed by an appropriate software. All the spectroscopic experimental results reported in this thesis have been obtained at room temperature, in backscatter condition, using a micro-Raman spectrometer (T-64000, Horiba/Jobin-Yvon., Kyoto, Japan) and an excitation source emitting at 532 nm (Nd:YVO_4 diode-pumped solid-state laser; SOC JUNO, Showa Optronics Co. Ltd., Tokyo, Japan) operating with a power of 10 mW. The figure 2.14 shows an overall view of the instrument.

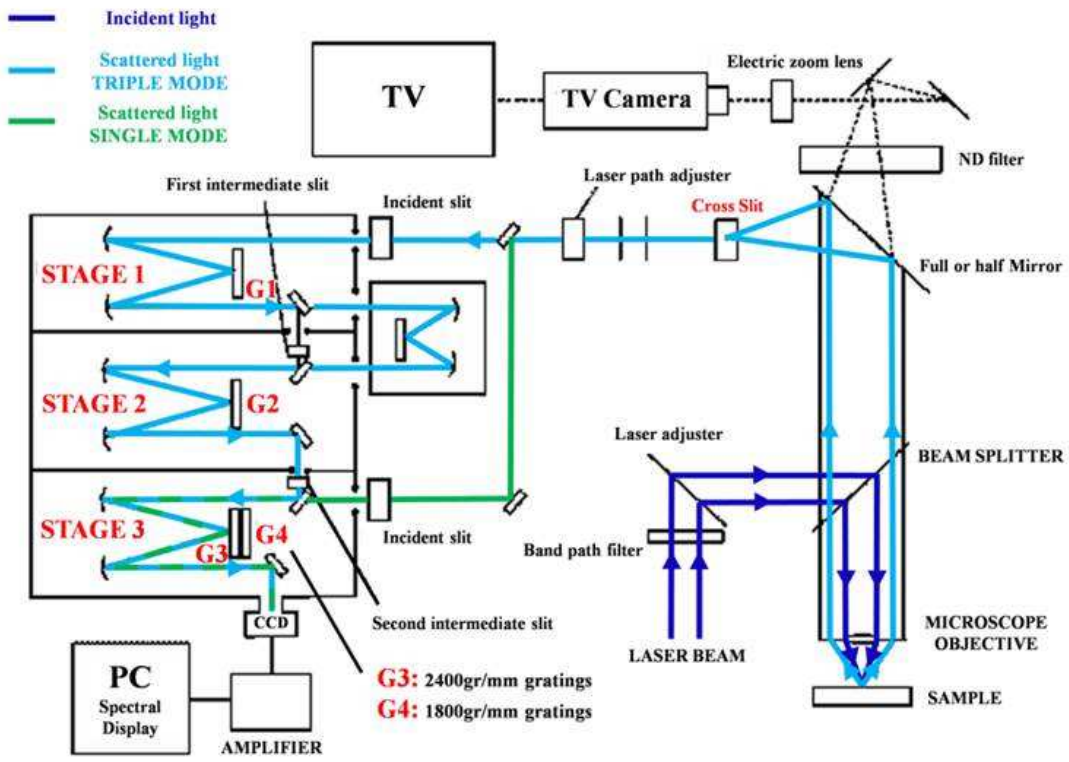

Figure 2.15: Scheme concerning the operation of T64000 spectrometer.

The instrument is equipped with an integrated triple monochromator design for increasing optical stability and spectral resolution; furthermore, it presents a set of holographic diffraction gratings of 600 gr/mm, 1800 gr/mm and 2400 gr/mm. This latter, in the spectrograph stage, permit to obtain the resolution and the range of wavelength that a spectrometer can handle. Indeed, a better dispersion of the polychromatic light is favored by an increase of the grooves number. Also the width of the spectral band depends by the grating used. The T64000 spectrometer can work using a single or triple monochromator. The triple configuration consists of one spectrographic stage and two pre-monochromators double. These latter are two identical grating (1800gr/mm) which work in a subtractive mode and act as filters adaptable to the specific spectral range (stage 1 and 2 of figure 2.15). In the single monochromator, notch filter is used to eliminate the elastic component (Rayleigh) and the first two stages are skipped (stage 3 figure 2.15). There is a motorized stage which allows to choose the point to analyze.

To acquire the spectrum, the detector used is a multichannel 1024 x 256 pixels CCD camera device (CCD-3500V, Horiba Ltd., Kyoto, Japan) mounted in the plane of the exit image and cooled down to 140 K with liquid-nitrogen.

The laser beam is focused on the sample by an optical microscope. This latter has three different objective long focus lenses: a 100x objective lens with NA=0.9, a 50x objective lens with NA=0.X and a 20x objective lens with NA=0.9. Using a beam splitter, the scattered light is separated from the incident beam because it is collected in backscattering configuration.

Furthermore the T64000 Raman spectrometer has a set of cross-lit, which allow the modulation of the Raman probe and hence can work in confocal mode, excluding the informations from the region out-of-focus. The confocal microscopy is technique employed in the Raman spectroscopy and in other imaging microscopy [229]. It has been patented by Minsky in 1957 [230], and presents two filtering pinhole, one placed on the laser beam path (Gaussian shape of probe is enhanced) and the second is located in the exit focal plane of the microscope (space resolution, both lateral and axial, improved) (Figure 2.16). Through this two pinhole it's possible to exclude the light originating from the out-of-focus planes.

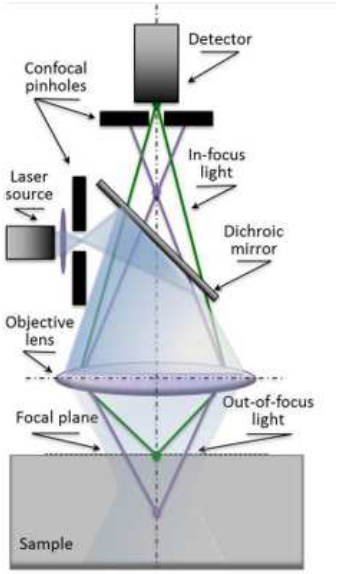

Figure 2.16: Schematic draft of the confocal configuration for Raman assessments.

The signal is brought from the surface to a focus at the aperture and passes without significant attenuation. On the other hand, out-of-focus light from below the surface is cut off because it is brought to a focus before the aperture. So this technique can bring advantages like an increase of resolution and an improvement of the signal / noise ratio.

2.4 Laser microscope

Laser microscope is a technique that permits to obtain high-resolution optical images with depth selectivity. It has been used to characterized the morphology of the samples and to quantify the growth of hydroxyapatite after cellular treatments. The key feature of this microscope is its ability to acquire in-focus images from selected points and depths. The principle on which is based the confocal microscope has been described by paragraph 2.3.4 and it's shown in the figure 2.17. The laser microscope used (Laser Microscope 3D & Profile measurements, Keyence, VK-x200 series, Osaka, Japan) has a very high resolution and a large magnification (24000X according to the manufacturer).

As written before, the confocal configuration presents two pinholes and only a small fraction of the volume of the sample around the point of focus will be probed.

This technique has also the advantage to scan not only in the xy plane but also along the z axis obtaining a 3D profile of the surface of the specimen. So, it's possible to obtain some informations about the profile and the surface roughness without any kind of contact with the surface of the sample avoiding to damage it.

Figure 2.17: 3D Laser Scanning Microscope of the VK-x200 series by Keyence.

2.5 Laser Raman Microscope

Raman microscope is a laser-based microscope used to perform Raman spectroscopy [231]. This technique begins with a standard optical microscope and adds a set of fundamental components in Raman spectroscopy like excitation laser, laser rejection filters, a monochromator, and a detector like CCD. Traditionally the use of Raman

microscopy was to measure the Raman spectrum of a point on a sample, but recently the implementing of Raman spectroscopy, for direct chemical imaging over the whole field of view on a 3D sample, has extended the technique.

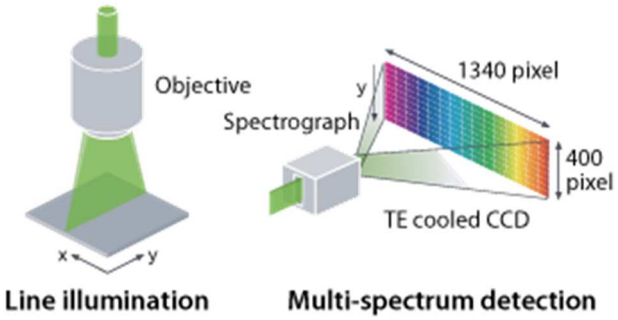

Figure 2.18: Illumination system of the device.

The instrument used is Laser Microscope RAMANtouch (Nanophoton Co., Osaka, Japan), which show the ultra-fast imaging and diffraction-limited spatial resolution. This device is equipped with the dedicated confocal optics, spatial resolution, closed to the diffraction limit which can achieve even in depth direction. The illumination mode forms point laser beams into line shaped to cover larger sample area.

This line of illumination excites Raman scattered light along the line-illuminated area by collecting 400 spectra simultaneously, thus collecting maps in a time faster than the movement of cells. The device presents galvanometer mirrors which help to scan fastly and accurately the laser beam. A spectrograph with 50 mm focal length is used and there are a multiple selections of gratings but it's possible to choose three gratings at maximum (150, 300, 600, 1200, 1800, 2400gr/mm). It has laser with different excitation wavelengths which you can decide to use based on the sample (488nm, 532nm, 671nm, 785nm).

Figure 2.19: Laser Raman Microscope RAMANtouch.

2.6 Experimental procedure

2.6.1 Cellular Treatment: Osteosarcoma SAOS-2

SaOS-2 (Human osteosarcoma cell line) ($5x10^5$cells/ml) were placed in 24-well plate above the discs of "as sintered" silicon nitride and the controls (Al_2O_3, alloy of Ti).
Also “as sintered” glazed samples and “polished” glazed samples have been tested with SAOS-2 cells to compare the osseointegration activity with Titanium control.
The cells were grown in osteogenic media (DMEM with 10% FBS, Ascorbic Acid, β-Glycerophosphate, Hydrocortisone) which was changed twice in a week.
culture conditions:

- CO_2 5%;
- Temperature 37°C;
- Humidity 95%.

After 7 days the samples were washed and analyzed.

Figure 2.20: 24-well plate with samples under cellular treatments.

2.6.2 Cellular Treatment: Mesenchymal stem cells (PDLSCs)

Human Periodontal Ligament Fibroblasts (Lonza, Switzerland) were cultured with Osteogenic media (DMEM with 10% FBS, Ascorbic Acid, β-Glycerophosphate, Hydrocortisone) on "polished" disks for osteogenic differentiation.
Culture conditions:

- CO_2 5%;
- Temperature 37°C;
- Humidity 95%.

The Medium was changed every 3days. After 5 weeks, Disks were removed from the culture plate and analyzed.

2.6.3 Raman spectroscopy

The Raman spectra have been recorded in backscattering, using a triple monochromator. An objective lens with a numerical aperture of 0.9 has been used both to focus the laser beam on the sample surface and to collect the scattered Raman light. A pinhole aperture of 100 µm was adopted with employing an objective lens with a magnification of 100x. Averages of 30 Raman spectra, collected at different random locations, were used for comparing differently treated Si_3N_4 samples. Acquisition time of 45 seconds is employed for all the analysis and for every spectrum 4 acquisition have been done to delete the presence of spike (narrow and intense peaks due to cosmic rays and not to the sample) and to reduce the background noise. Spectral windows were centered at 850 cm^{-1} and 3000 cm^{-1}. The spectra have been studied using two software commercially available: Labspec 5 (Horiba, Japan) and Origin 9.2 (OriginLab Co. Northampton, MA, USA).

2.6.4 Laser Microscope

The excitation source in the experiments used a 408 nm violet semiconductor laser operating with an output of 0.95 mW. An objective lens with a numerical aperture of 0.55 was used both to focus the laser beam on the sample surface and to collect the reflected light. Taking advantage of an automated stage, whose movement can be controlled in xyz directions, a 3 dimensional colored image of the sample surface can be acquired by joining the 3D profile with the optical microscope image. The images of the samples have been taken at two different magnifications, 10X, 20X and 150X. Datas have been analyzed using the software VK Analyzer (Keyence, Osaka, Japan).

2.6.5 Laser Raman Microscope

Raman microscopy images were collected on living SaOS-2 cells with a dedicated equipment (RAMANtouch, Nanophoton Co., Osaka, Japan) with a 20x immersion-type optical lens. The excitation source emitted at 785 nm and the spectral resolution was 1.2 cm^{-1} (spectral pixel resolution equal to 0.3 cm^{-1}/pixel).

Chapter 3

RESULTS AND DISCUSSIONS

3.1 Surface characterization of silicon nitride samples

3.1.1 Raman characterization

Silicon nitride samples have been characterized before the cellular treatment using Raman spectroscopy to understand surface chemistry.
Figure 3.1 shows the spectrum of the different samples:

- untreated (AS);
- chemically etched with HF (HF);
- thermally treated in N_2 atmosphere (N_2);
- thermally oxidized (OX);
- glazing treated.

All of the silicon nitride samples spectra have three main peaks (henceforth referred as "main triplet"), respectively at about 180 cm^{-1}, 200 cm^{-1} and 220 cm^{-1} (peak 1, 2 and peak 3 in the Figure 3.1) and related to the vibrational modes [232]:

- E_{2g} (~180 cm^{-1});
- A_g (~ 200 cm^{-1});
- E_{1g} (~ 220 cm^{-1}).

In addition to this "main triplet", there are other two peaks of silicon nitride at about 450 cm^{-1} (peak 5 in Figure 3.1) and 615 cm^{-1} (peak 6 in Figure 3.1) which both represent E_{2g} vibrational modes. Depending on the sample, triplet spectra have different relative intensities depending on the surface treatment to which they have been subjected. Silicon

nitride glazed sample spectra shows numerous peaks, compared with other samples. In the glazed samples the “main triplet” is present but, compared to those in the other spectra, it is less intense.

There are many other peaks related to Y_2O_3 [233], AlN [234], α-Al_2O_3 [235] and SiO_2 [236,237]. These are the five differet powders contained in the glazed slurry used in the glazing treatment. There are, also, peaks of Yttrium Alluminum Garnet (YAG) arising from heating glazing mixture at high temperature [238]. YAG has many peaks, the most intense being at 402 cm^{-1} which is also the highest of the spectrum. Furthermore, in the spectrum there are two peaks releated to α-Si_3N_4 [239]. All the peaks of glazed spectrum, with related symmetry, have been listed in the table 3.1.

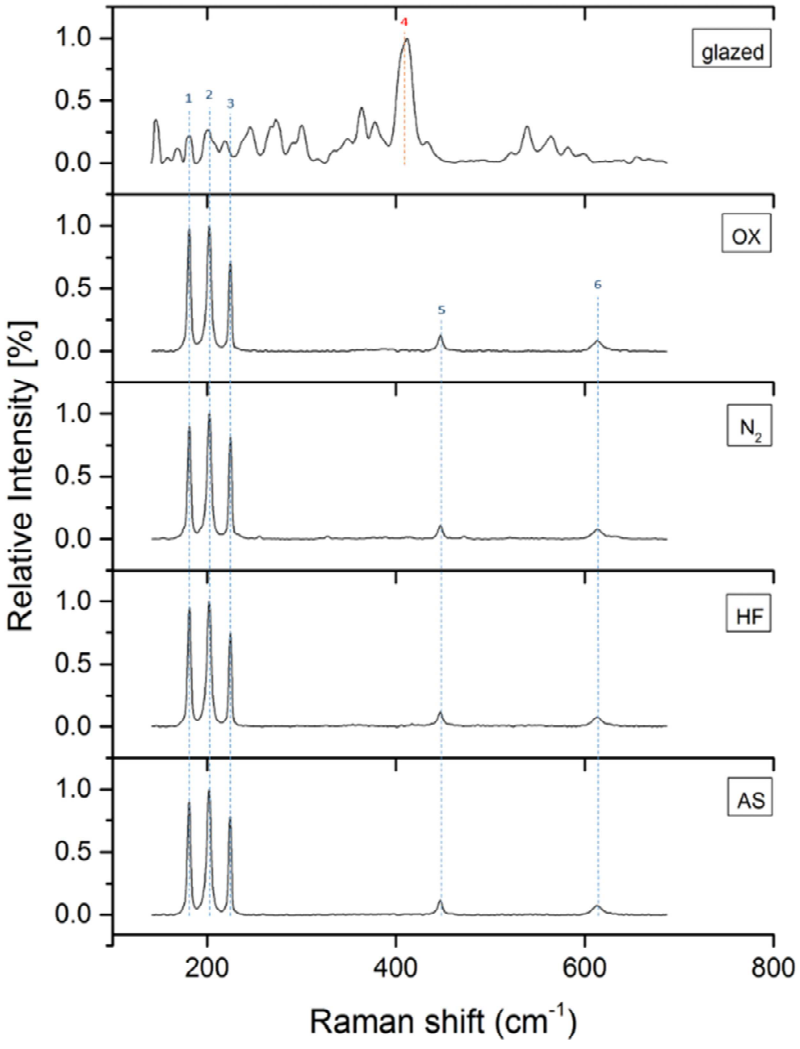

Figure 3.1: Raman Spectra of silicon nitride samples: as-sintered (AS), etched with HF (HF), N2 annealed (N2), thermally oxidized (OX) and glazed. peaks labeled referred to vibrational modes of silicon nitride (peaks 1,2,3,5 and 6) and to YAG (peak 4).

RAMAN SHIFT [cm^{-1}]	COMPOUND	SIMMETRY
125	Y_2O_3	T_g
149	YAG	T_{2g}
161	Y_2O_3	A_g+T_g
181	β-Si_3N_4	E_{2g}
200	β-Si_3N_4	A_g
221	YAG	T_{2g}
230	β-Si_3N_4	E_{1g}
249	AlN	E_2
259	YAG	T_{2g}
274	SiO_2	
318	Y_2O_3	T_g+E_g
334	Y_2O_3	E_g
351	SiO_2	A_1
366	α-Si_3N_4	A_1
375	YAG	A_{1g}
393	YAG	E_g
402	YAG	T_{1g}
424	Y_2O_3	T_g
515	α-Si_3N_4	
533	YAG	E_g
560	YAG	A_{1g}
578	α-Al_2O_3	E_g
597	Y_2O_3	T_g
655	AlN	E_2

Table 3.1: Raman peaks assigment for glazed silicon nitride Raman spectra.

3.1.2 Laser Microscope: roughness and morphology

Surface roughness measurement were carried out (Figure 3.2). As-sintered samples have been compared pointing out that:

- The three samples subjected to physical and chemical processing (HF, N_2, OX) are uniform and don't show statistical difference ($p \geq 0.05$);
- The roughness of the three treated samples is higher than Al_2O_3 and as-sintered (AS) ($p \leq 0.05$);
- The roughness of Ti control doesn't show a statistical significant difference with all the silicon nitride samples ($p \geq 0.05$).

In the table 3.2 there are the value of Ra, the arithmetic mean roughness and standard deviation of all the As-sintered samples, and controls.

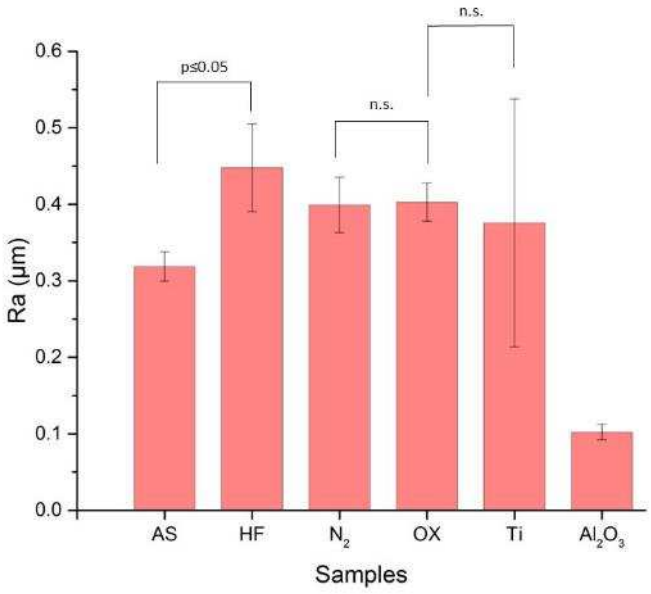

Figure 3.2: Roughness of As-sintered samples compared with commercially available bioceramic alumina and Ti samples.

Samples	Ra (µm)	Std Dev
AS	0.318	0.019
HF	0.447	0.057
N_2	0.399	0.036
OX	0.402	0.024
Ti	0.375	0.162
Al_2O_3	0.102	0.010

Table 3.2: Average roughness of As-sintered samples and controls.

Both glazed samples show statistically significant differences in roughness compared with the controls and with untreated sample (Figure 3.3). Glazed samples have the highest roughness compared to the as-sintered glazed and other control samples while the two glazed samples haven't significant statistical differences among themselves. This high level of roughness is given because of the surface treatment.

Table 3.3 represents values of average roughness of the glazed samples.

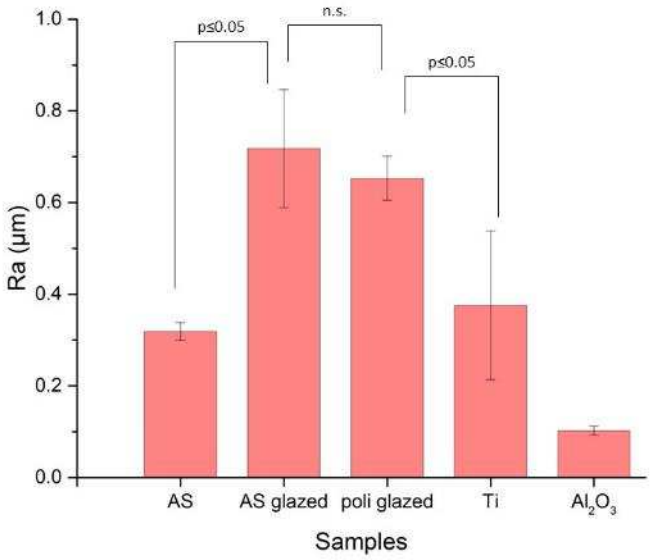

Figure 3.3: Roughness of glazed samples compared with as-sintered sample and with commercially available bioceramic alumina and Ti samples.

Samples	Ra (µm)	Std. Dev
AS glazed	0.718	0.128
Poli glazed	0.653	0.048

Table 3.3: Average roughness of as-sintered glazed sample and polished sample.

All the polished samples have different roughness showing statistically significant differences in all the comparisons and having lower roughness compared to controls, as shown in Figure 3.4. This is because the processing and mechanical treatment received before the chemical/physical changes. Among the silicon nitride samples, the one that has a greater roughness is the thermally oxidized sample (OX), while the sample treated with hydrofluoric acid (HF) has a roughness less than the untreated sample (AS). In Table 3.4 are reported polished samples average roughness values.

Images obtained by laser microscope using a magnification at 150X are showed below. As-sintered samples (Figure 3.5a-5c), surfaces don't exhibit obvious morphological hexagonal even though Si_3N_4 grains anisotropically arranged are clearly visible.

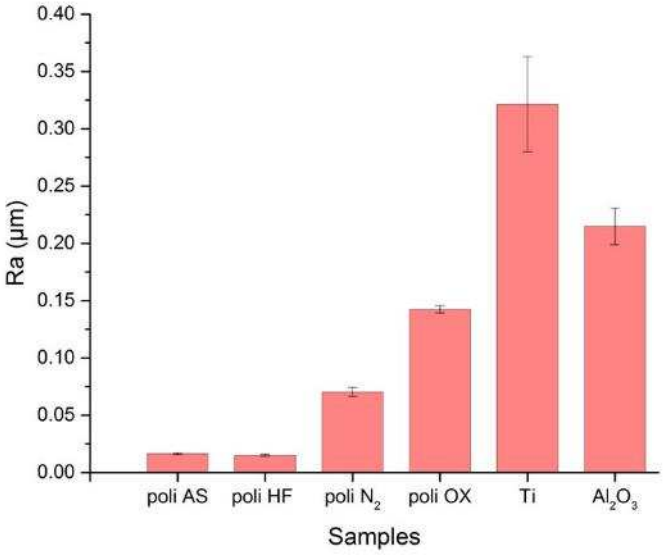

Figure 3.4: Polished sample roughness compared with commercially available bioceramic alumina and Ti samples. All the samples show statistical differences. ($p \leq 0.05$)

Samples	Ra (µm)	Std Dev
Polished AS	0.016	0.001
Polished HF	0.015	0.001
Polished N_2	0.070	0.003
Polished OX	0.142	0.003

Table 3.4: Polished samples average raoughness compared with controls.

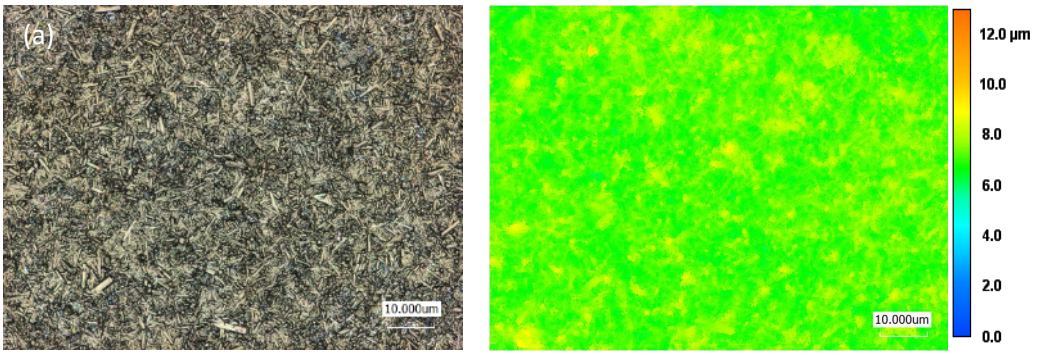

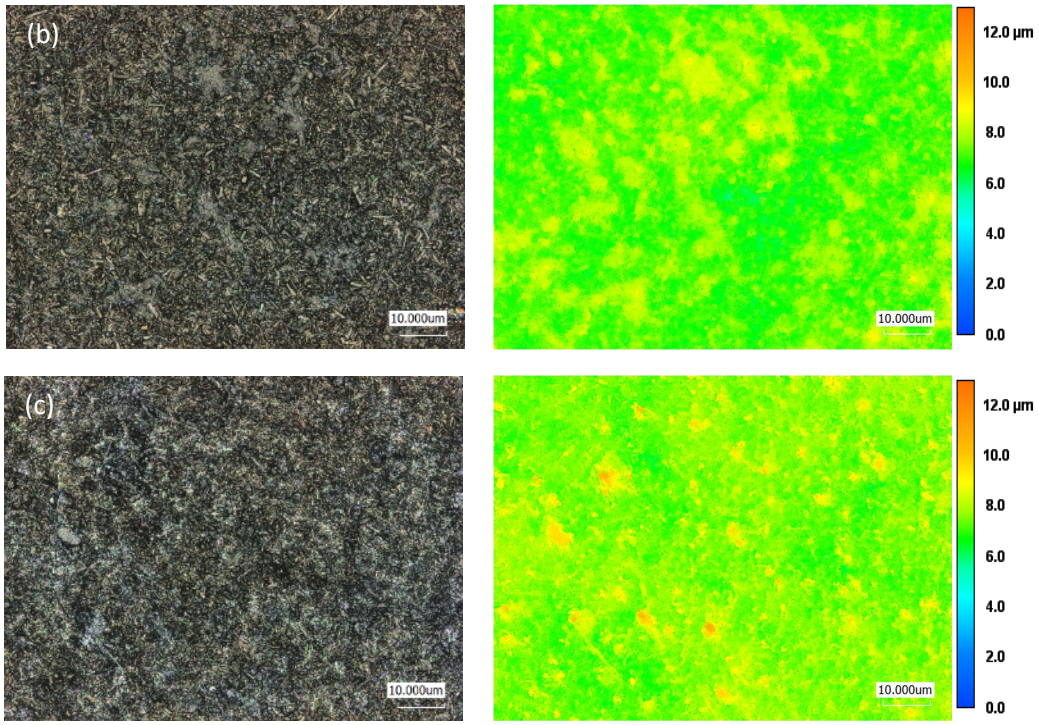

Figure 3.5: Silicon Nitride samples laser micrographies at 150X of magnification: as-sintered untreated (a), N_2 annealed (b), thermally oxidized (c).

The glazed samples (Figure 3.6a and 3.6b) have a different morphology compared to all other samples, given by the glazed layer. It is possible to note the differences of the underlying layer between as-sintered glazed and the glazed polished sample due to different roughness. The as-sintered sample seems to have a more homogeneous surface than the polished samples.

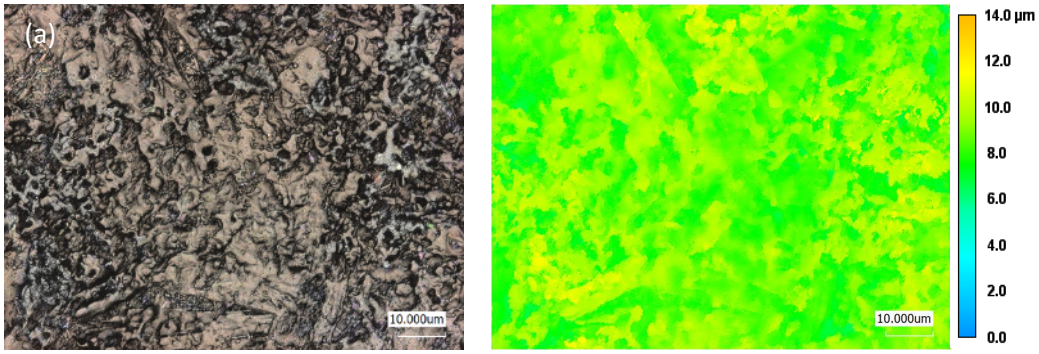

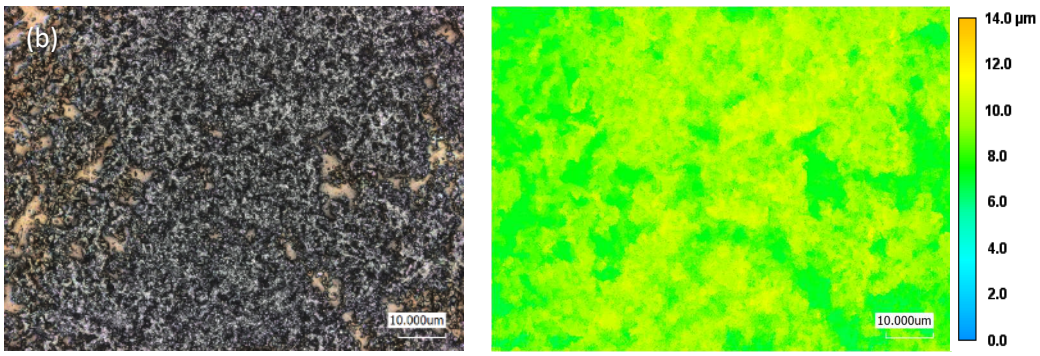

Figure 3.6: Laser micrograph of glazed sample at 150X of magnification: as-sintered (a), polished (b).

The polished samples show morphological differences between each other in the case of AS and HF samples with a surface appearance almost equal (Figure 3.7a-3.7c). Unlike the as-sintered samples, the anisotropic grains of silicon nitride are not visible due to the mechanical treatment to which they have been subjected. The surface modifications can be observed especially on the samples treated in nitrogen atmosphere (N_2) and thermally oxidized (OX) which present a different morphology than the untreated sample (pure).

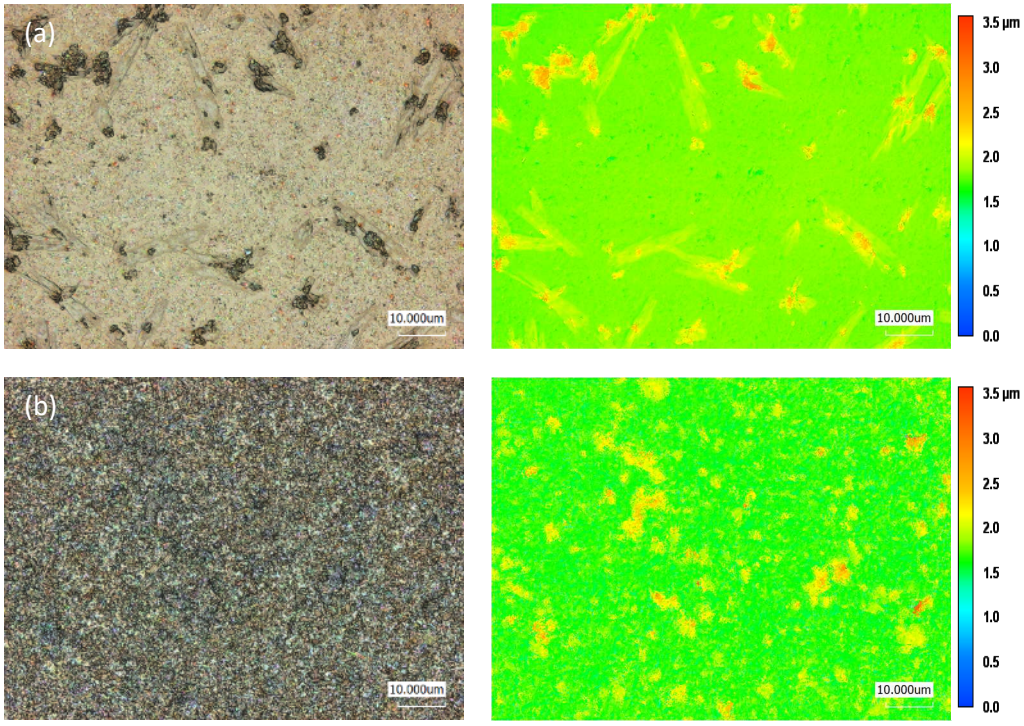

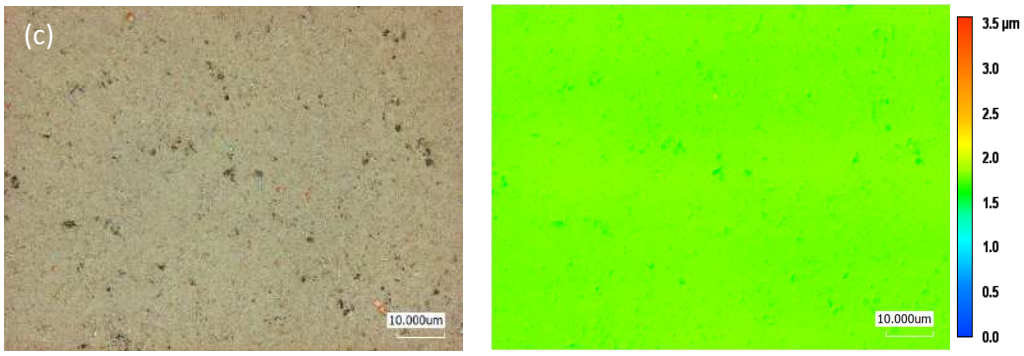

Figura 3.7: Laser micrograph of polished silicon nitride samples at 150X of magnification: N_2 annealed (a), thermally oxidized (b), polished untreated (c).

3.2 Analysis after SAOS-2 treatment

3.2.1 Raman analysis of as-sintered and glazed samples

A Raman characterization of silicon nitride as-sintered and glazed samples was carried out after the cell treatment with SAOS-2. Figure 3.8 refers to the average spectra, which all show a main peak at 960 cm^{-1} corresponding to the P-O symmetric stretching of hydroxyapatite [240]. In addition to this band there are also other major bands summarized in the table 3.5 and related to the vibrational modes of hydroxyapatite, bands at about 591,947,1044 and 1076 cm^{-1} and approximately corresponding to vibrational modes ν_1, ν_3 and ν_4 of the tetrahedral phosphate [240,241]. This shows the effective formation of the mineral on the surface of the samples.

In addition, there are also bands corresponding to vibrational modes of biological and cellular components such as lipids, DNA, and the collagen proteins necessary for the formation of bone tissue matrix.

Among these there are some peaks related to vibrational modes ν of C-C binding and ν_{as} of C-C of lipids at 1088 cm^{-1}, 1125 cm^{-1} [241]. These components are very important in the mineralization process because they are the main constituents of the matrix vesicles. Moreover, lipids can assembly complex with cholesterol-dependent which involve the externalization of phophatidylserine [242]. There are two peaks in the spectra, related to the presence of cholesterol, at 609 cm^{-1} and at 2967 cm^{-1} [243]. Cholesterol is present inside the matrix vesicles and some, according to some studies, plays an active role in the

initial mineralization processes thanks to the good fit with the crystallographic HA crystal structures [244,245].

There are two peaks at 577 cm^{-1} and 730 cm^{-1} relating to two classes of phospholipids that are very important: phosphatidylserine and phosphatidylinositol [243]. These latter play a main role in the formation of hydroxyapatite, as located in the most active sites of nucleation. Phosphatidylserine, in contact with lipids droplets, has a high binding affinity towards Ca^{2+} ions and also reacts with phosphates resulting in phospholipid:calcium: phosphate ion complexes which help in early mineralization [246-249]. It facilitates calcium-dependent Annexin protein binding, and are permissive for Annexins forming calcium channels through the membrane. The result is the entrance of ions Ca^{2+} into matrix vesicles for crystal formation [250]. Phosphatidylinositol, instead placed in the membrane of matrix vesicles, in form of glicophosphatidylinositol (GPI) bond to the membrane thanks to fatty acids, has the function to anchor the alkaline phosphatase. This latter is a mineralization promoter, an important enzyme to increase the concentration of inorganic phosphate.

Regarding protein component, there are different peaks in the spectra related vibrational modes of C-C stretching of collagen backbone or of amino acids like phenylalanine and tyrosine at 621 cm^{-1},859 cm^{-1}, 937 cm^{-1}, 1003 cm^{-1} and 1030 cm^{-1} [241,251-253]. These peaks indicate the presence of an organic extracellular matrix necessary for the growth of the tissue. Furthermore, the presence of the phenylalanine indicates cell viability.

Furthermore, there are several bands related to the vibrational modes of proline (at 727 cm^{-1}, 827 cm^{-1}, 853 cm^{-1},937 cm^{-1}, 1066 cm^{-1}) [241,254]. Proline is a non-essential amino acid, necessary for the formation of collagen type-I which is essential for the mineralization process in the extracellular matrix.

The amino acid glutamate is used as a precursor in the biosynthesis of proline [255]. The intracellular proline concentration increases with the confluence of cells [255].

There are two band related to the presence of hydroxyproline, at 827 cm^{-1} and 937 cm^{-1} which is formed from the hydroxylation of proline under the influence of ascorbic acid (ASAP), which was added to cell culture media in this study [241,249]. Proline, hydroxyproline, glycine and other amino-acids constitute pro-collagen, which is exocytosed by Golgi bodies and is processed by pro-collagen peptidase to yield collagen. Collagen molecules are attached to the external side of the cell membranes in an organized way by fibronectins and integrins resulting in collagen type-I.

In the Figure 3.9, spectra centered at 3000 cm^{-1} were obtained to verify the presence of collagen proteins and organic components responsible for the formation of bone extracellular matrix. The figure shows a broad peak between 2800 cm^{-1} and 3000cm^{-1} corresponding to protein and lipids bonds vibrations.
The main intense peaks are related to [256,257,243]:

- CH_2 asymmetric stretching of lipids at 2933 cm^{-1} (peak 3 in Figure 3.9);
- CH_2 asymmetric stretching of proteins at 2891 cm^{-1} (peak2);
- CH_2 symmetric stretch of lipids at 2967 cm^{-1} (peak 4);
- CH_2 asymmetric stretch of lipids and proteins of lipids and proteins at 2871 cm^{-1} (peak 1);
- vibrational modes ν of aromatic amino acid residues at 3054 cm^{-1} (peak 5);
- C-H stretching of aromatic or aliphatic groups of proteins at 3065 cm^{-1}.

All the peaks and their relative assignments are listed in the table 3.5.
Studies carried out on this spectral window, in different time interval, have allowed to understand some aspects of the mineralization process, highlighting how the morphology and the intensity of the peaks can vary by passing to an increase of bands related to stretching of the protein and consequent decrease in those concerning to lipids. This indicates that there is the influence of lipids in the early stages of mineral formation, which are subsequently replaced by the proteins in the advanced stage which allows the growth of the apatite. In our case, in the area of 2800 cm^{-1} and about 3000 cm^{-1}, peaks related to vibrational modes of the lipids are still present. In particular, there is the peak at 2933 cm^{-1} which is the most intense of the spectrum, relative to the asymmetrical stretching of the CH_2 in lipids; this indicates how cells are still in the initial states of the mineral formation [249].
In summary, the Raman spectra of samples as-sintered and glazed silicon nitride treated with the cell line SAOS-2 have revealed the presence of numerous important components relating to the process of mineralization and formation of the extracellular matrix through matrix vesicles and creation of collagen scaffold.

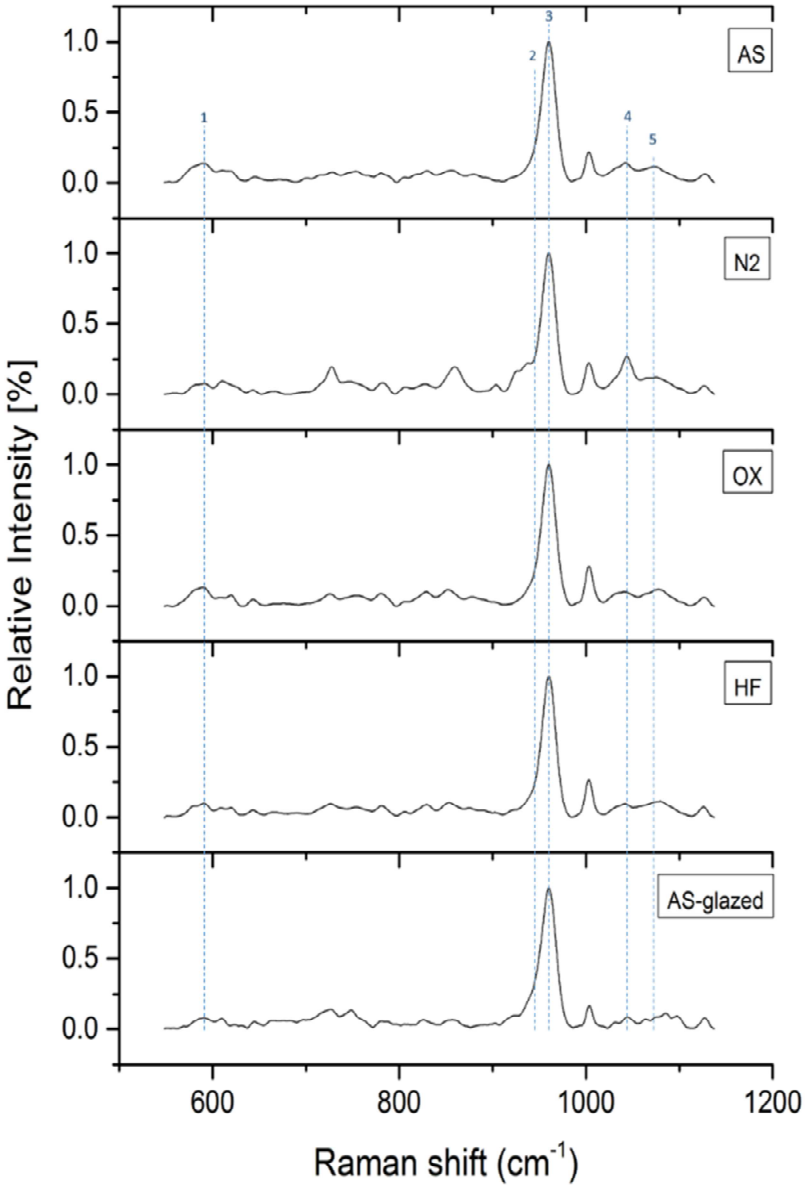

Figure 3.8: Raman spectra centered at 850 cm^{-1} of silicon nitride as-sintered and glazed samples treated with SAOS-2. The labeled peak (1-5) are relative to v_1 symmetric stretching of P-O (peak 2 and 3) or v_4 and v_3 of PO_4^{3-} (peak 1,4 and 5) of hydroxyapatite.

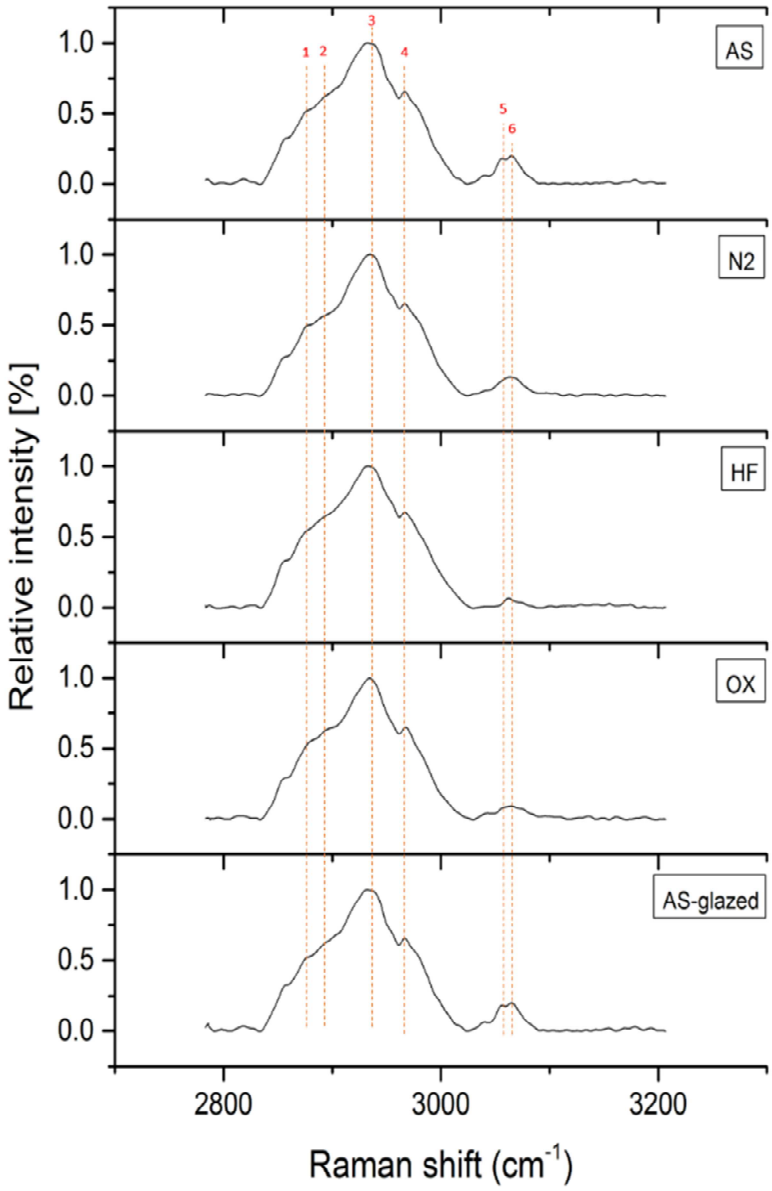

Figure 3.9: Raman spectra centered at 3000 cm^{-1} of silicon nitride as-sintered and glazed samples treated with SAOS-2. The labeled zone related to an interval between 2800 cm^{-1} and 3000 cm^{-1}contains some peaks which refer to symmetric stretching of CH, CH_2 and CH related to protein and lipids (peak 1-4). The labeled zone at about 3050-3070 cm^{-1} regards to different peaks referred to a vibrational modes of aromatic amino acids residues and to symmetric C-H stretching of aromatic and aliphatic groups of proteins (peak 5 and 6).

RAMAN SHIFT [cm^{-1}]	ASSIGNEMENT	REFERENCE
577	Phosphatidylinositol	[243]
591	Symmetric stretching vibration of ν_4 PO_4^{3-} (phosphate of HA)	[241]
609	Cholesterol	[243]
621	C–C twisting mode of phenylalanine	[251-253]
727	C–C stretching, proline (collagen assignment)	[254]
730	Phosphatidylserine	[243]
746	T (ring breathing mode of DNA/RNA bases)	[258]
755	Symmetric breathing of tryptophan	[251,253]
781	Cytosine/uracil ring breathing (nucleotide)	[251,252]
827	Proline, hydroxyproline, tyrosine, ν_2 PO^{2-} stretch of nucleic acids	[241]
853	Ring breathing mode of tyrosine and C–C stretch of proline ring, Structural proteins like collagen	[251,252, 259]
859	Tyrosine, collagen	[251]
937	Proline (collagen type I), Amino acid side chain vibrations of proline and hydroxyproline, as well as a (C–C) vibration of the collagen backbone	[241]
947	Hydroxyapatite P-O symmetric stretching	[240]
960	Hydroxyapatite P-O symmetric stretching	[240]
1003	Phenylalanine (of collagen)	[241]
1030	Phenylalanine of collagen	[241]
1044	ν_3 PO_4^{3-} (symmetric stretching vibration of ν_3 PO_4^{3-} of HA)	[241]
1066	Proline (collagen assignment)	[254]
1076	Symmetric stretching vibration of ν_3 PO_4^{3-} (phosphate of HA)	[240]
1088	ν_1 CO_3^{2-}, ν_3 PO_4^{3-}, ν(C–C) skeletal of acyl backbone in lipid	[241]
1124	ν(C–C) skeletal of acyl backbone in lipid	[241]
2854	CH_2 symmetric stretch of lipids, CH_2 asymmetric stretch of lipids	[256]
2871	CH_2 symmetric stretch of lipids, CH_2 asymmetric stretch of lipids and proteins	[256]
2891	CH_2 asymmetric stretch of proteins	[256]
2912	CH stretch of lipids and proteins	[256]

2933	CH_2 asymmetric stretch	[256]
2967	ν_{as} CH_3, lipids, fatty acids, cholesterol and cholesterol ester	[257,258]
3006	ν_{as}(=C-H), lipids, fatty acids	[257]
3054	vibrational modes ν of aromatic amino acid residues	[260]
3065	C-H stretching of aromatic or aliphatic groups of proteins	[261]

Table 3.5: Peak assignments for as-sintered samples and glazed samples Raman spectra.

3.2.2 Laser Microscope: HA volume and distribution

The analysis performed by Raman spectroscopy allowed to confirm HA presence and to calculate its volume.

Images were collected using a magnification at 10X to determine the distribution of the formed matrix. It is important to underline that, the distribution of the mineralized extracellular matrix has taken place over the whole sample, but featuring more central areas indicating the uniformity of the samples.

Figure 3.10 shows the different volumes of HA formed over the as-sintered samples.

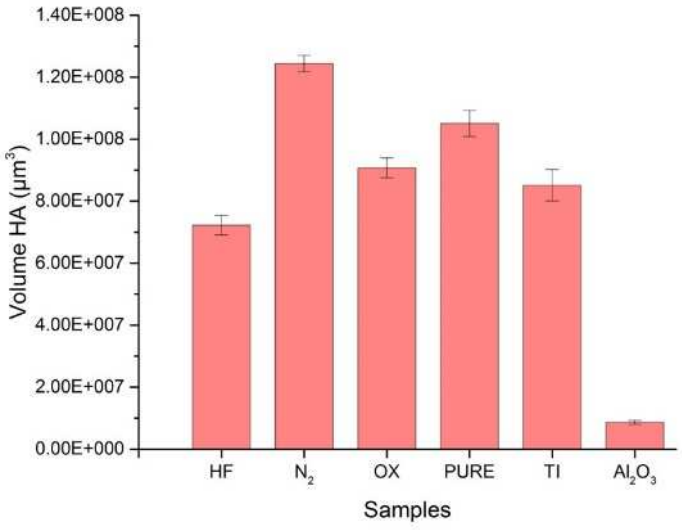

Figure 3.10: HA volumes in the as-sintered samples tested using SAOS-2 compared with Ti alloy and Al_2O_3 controls. All the samples show statistical significate differences ($p \leq 0.05$).

All samples showed significant statistical difference between each other. The sample N_2 present the highest volume compared to the other as-sintered samples and in particular compared to Ti and Al_2O_3 controls.

Analyzing the data about the roughness obtained prior to treatment, the N_2 annealed sample doesn't show differences with other as-sintered sample, subjected to other chemical and physical treatments, and titanium. So it is not possible to distinguish an influence net by the roughness. It can be assumed, therefore, that a principle underlying this result must be due to the surface characteristics derived from thermal and chemical modifications made before the cell treatment which modify the charge surface. Following a study carried out by Bock in 2015, it is seen as the heat treatment in a nitrogen atmosphere, leading to the formation of a layer of β-Si(Y)AlON. Instead, the sample thermally oxidized in air has a layer surface of SiO2 while the sample treated chemically with HF hasn't the surface oxide layer, but surface rich in amino groups [182]. It is supposed, therefore, that the layer of β-Si(Y)AlON neoformed modifies the surface charge conferring hydrophilic characteristics, contrarily to the other samples. This has been confirmed by analysis made by Bock about the contact angle of the different silicon nitride samples; the results have shown how the N_2 sample has the lowest contact angle than the others.

The figures 3.11 shows schematic drafts of the Si_3N_4 surface structure (surface and related charges) at physiological pH:

- The HF-etched "clean" surface, on which the neutral amine groups, NH_2, prefer to accept protons and stay as protonated amino groups, $-NH^{3+}$, thus producing an overall positive charge;
- The thermally oxidized surface with its amphoteric SiO_2 layer by negatively charged deprotonated silanols, SiO^-;
- The N2-annealed surface, on Which Both $-NH^{3+}$ and SIO^- coexist, but the plus charge is enhanced by positively charged given by the presence of Al and Y.

Then, assumption can be made about a "zwitterionic" behavior of the N_2 sample at the surface level conferred by surface charges. It's possible that this surface zwitterionic-like, with both positive and negative charge, influences mostly cell adhesion and proliferation.

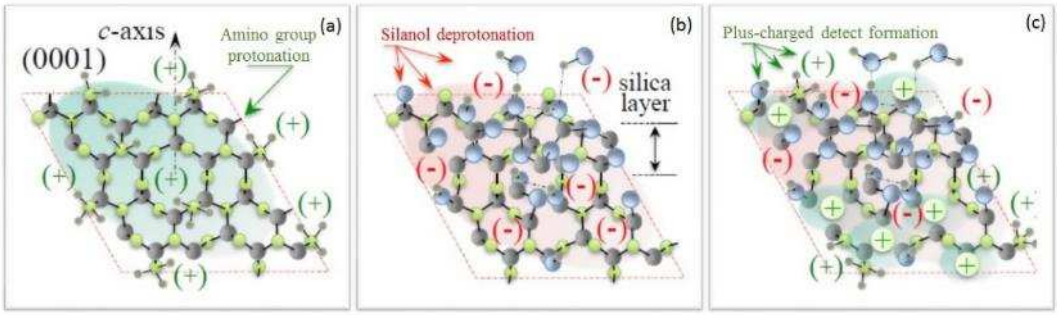

Figure 3.11: Schematic drafts of the Si_3N_4 surface structures and related surface charge at physiological pH: (a) positively charged HF-etched "clean" surface with protonated amino groups, $-NH^{3+}$; (b) negatively charged (thermally) oxidized surface with amphoteric SiO_2 terminated with deprotonated silanols, SiO^-; and, (c) mix-charged N_2-annealed with both negatively charged SiO^- and positively charged $-NH^{3+}$.

This hypothesis about the important role of surface charge in silicon nitride samples is confirmed by the studies made in other biomaterials which have different surface charges [38-44]. These have demonstrated how the surface, having a highly polarized surface, negatively, positively or a "zwitterionic" surface, allows the formation of a protein layer due to serum proteins from the culture medium and subsequent cell adhesion, proliferation and mineralization.

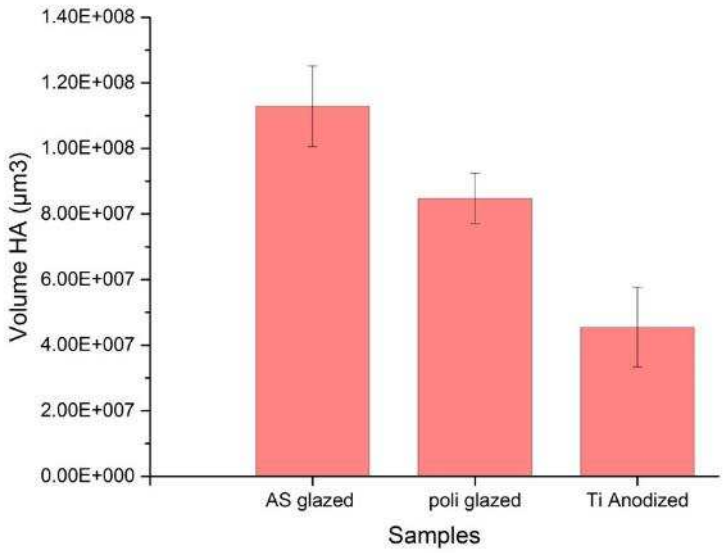

Figure 3.12: HA volumes in the glazed samples tested using SAOS-2 compared with Ti alloy control. All the samples show statistical significate differences ($p \leq 0.05$).

In the case of glazed samples, it is possible to note that the volume of HA is higher in both samples compared to the titanium control used (Figure 3.12). The two silicon nitride samples have shown significant statistical differences with the control. The sample which has showed the highest volume of hydroxyapatite is AS-sintered glazed.

This data suggests that an important role is played by the additives added in the processing that have resulted in an even greater formation of β-Si(Y)AlON thus increasing the number of active sites loads. The higher amount of Y and Al on the surface may have made an increase of the charges, further polarizing surfaces both in the case of the as-sintered sample and in that polished. Furthermore, the results show, from the analyzes previously carried out to the cellular tests, as the surface treatment has also led to an increase in roughness than the control sample and compared to the sample as-sintered untreated.

Hypothesis can be made, saying how roughness, in this case, has played an important role in adhesion and cell behavior. Studies using rat osteoblasts showed a high proliferation and expression of alkaline phosphatase and osteocalcin materials having rough surfaces [262]. These results were also confirmed by Lim et al in 2005 thanks to tests performed on human fetal osteoblast cells in which there has been a high dissemination and proliferation in samples having rough surfaces [263]. Therefore, it is possible that the high level of roughness present compared to samples of Ti may have influenced the adhesion in combination with the surface charge present.

Following, images at 10X of magnification of as-sintered samples, N_2, OX, the untreated sample (AS) and Ti control are shown below (Figure 3.13a-d). In addition, there are also images of the two glazed samples (AS and poli) and its titanium control used and treated under the same conditions (Figure 3.13e-g).

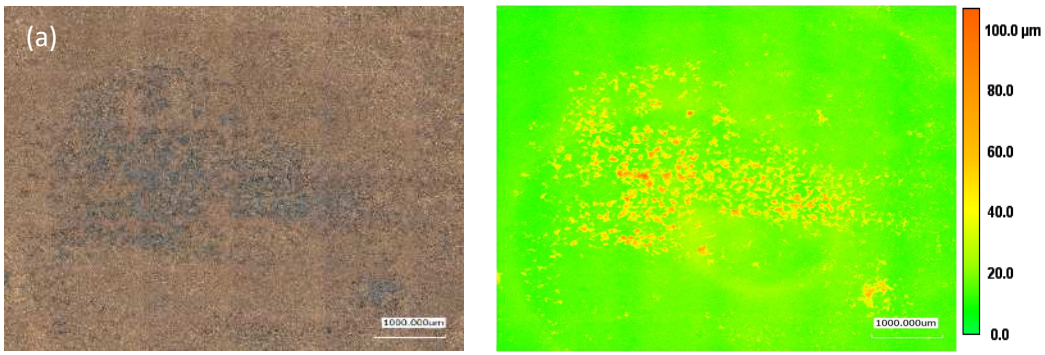

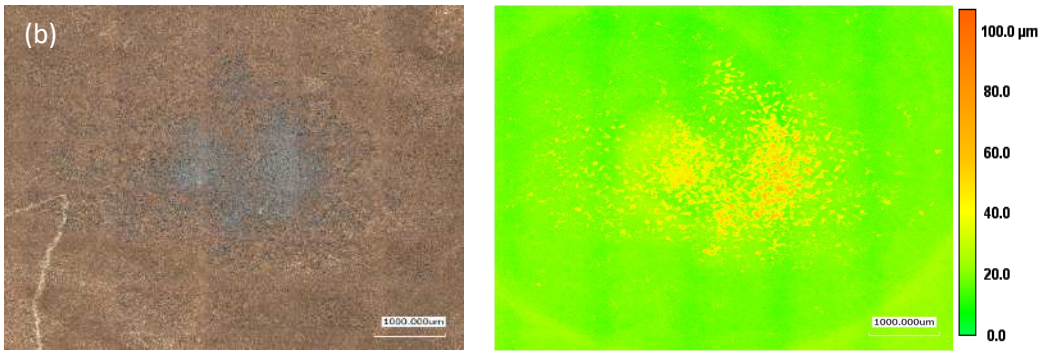
(b)
1000.000um
1000.000um
100.0 µm
80.0
60.0
40.0
20.0
0.0

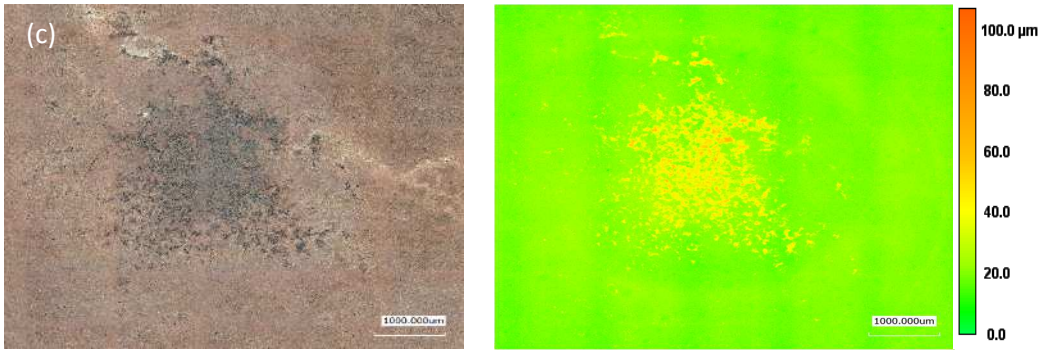
(c)
1000.000um
1000.000um
100.0 µm
80.0
60.0
40.0
20.0
0.0

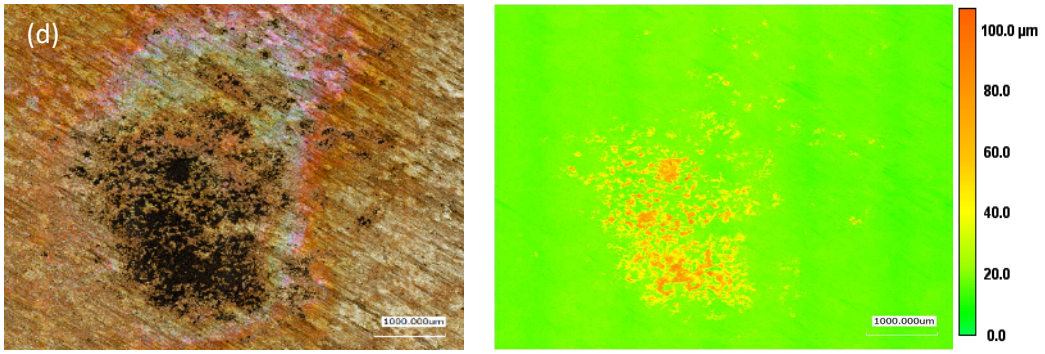
(d)
1000.000um
1000.000um
100.0 µm
80.0
60.0
40.0
20.0
0.0

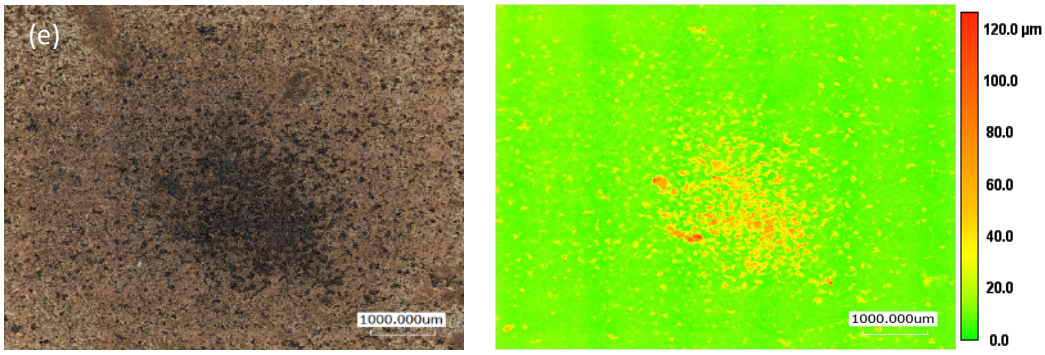
(e)
1000.000um
1000.000um
120.0 µm
100.0
80.0
60.0
40.0
20.0
0.0

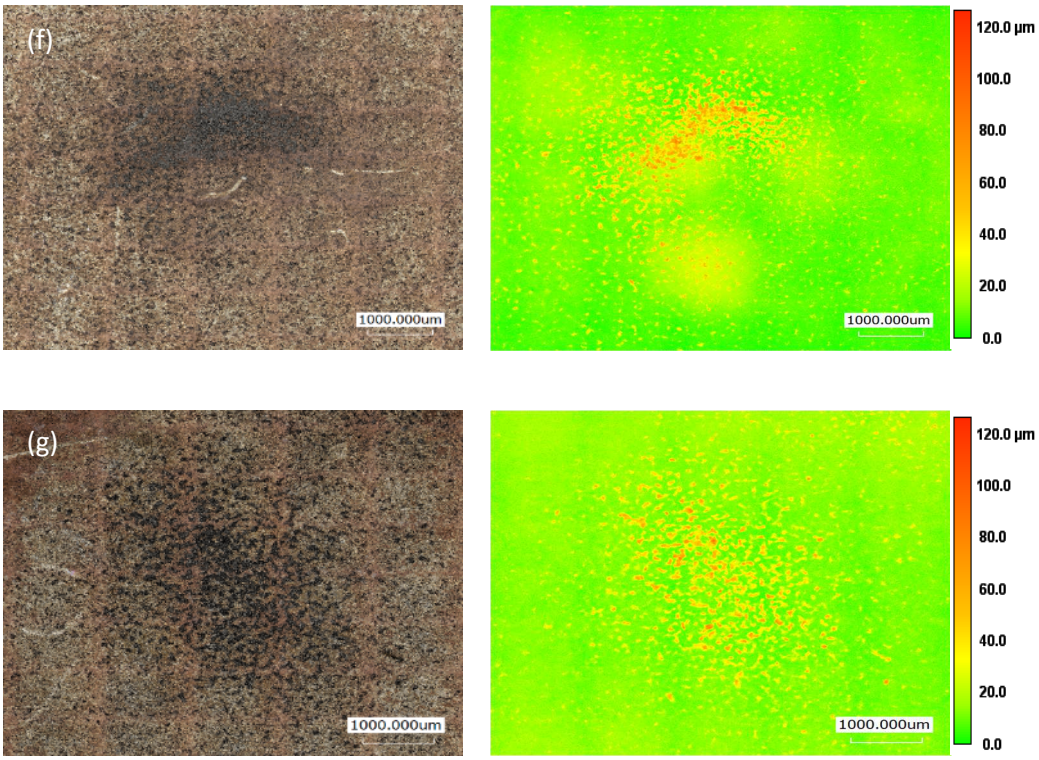

Figure 3.13: Laser micrograph at 10X of magnification of As-sintered samples: N_2 annealed (a), untreated (b), thermally oxidized (c), Titanium control (d), polished glazed (e), as-sintered glazed (f) and Titanium anodized (g). All the images are taken at 10X of magnification after SAOS-2 treatment.

From the images, it's possible to see how the mineralized extracellular matrix is uniformly distributed in the surfaces of all the samples, especially in the galzed samples. There are some sites of nucleation of the matrix which indicate also the homogeneity of the samples. This results can be seen also through the Laser Raman Spectroscope which identify particular areas of the samples where the cells adhere and start the formation of the matrix.

3.2.3 Laser Raman microscope

Laser Raman microscope analysis allowed to obtain Raman maps that showed *in situ* formation of hydroxyapatite and extracellular matrix compounds. Some tests using only SAOS-2 to monitor the growth without silicon nitride disks have been made. Analyzing an area of the sample interested by the growth of extracellular matrix, it's possible to obtain Raman maps on wide surfaces in very short times. From these latter it's possible, through the software, to label a peak of interest and plot intensity and/or area on the map.

In these cases, the highest peak of hydroxyapatite at 960 cm^{-1} and the bands between 2800 to 3000 cm^{-1} have been selected and plotted in the map.

Control tests made using SAOS-2 cells placed in a well without any silicon nitride sample have been shown in the Figures 3.14a- 3.14d. These cells were periodically monitored in order to evaluate the cell growth and the formation of hydroxyapatite using Laser Raman Microscope.

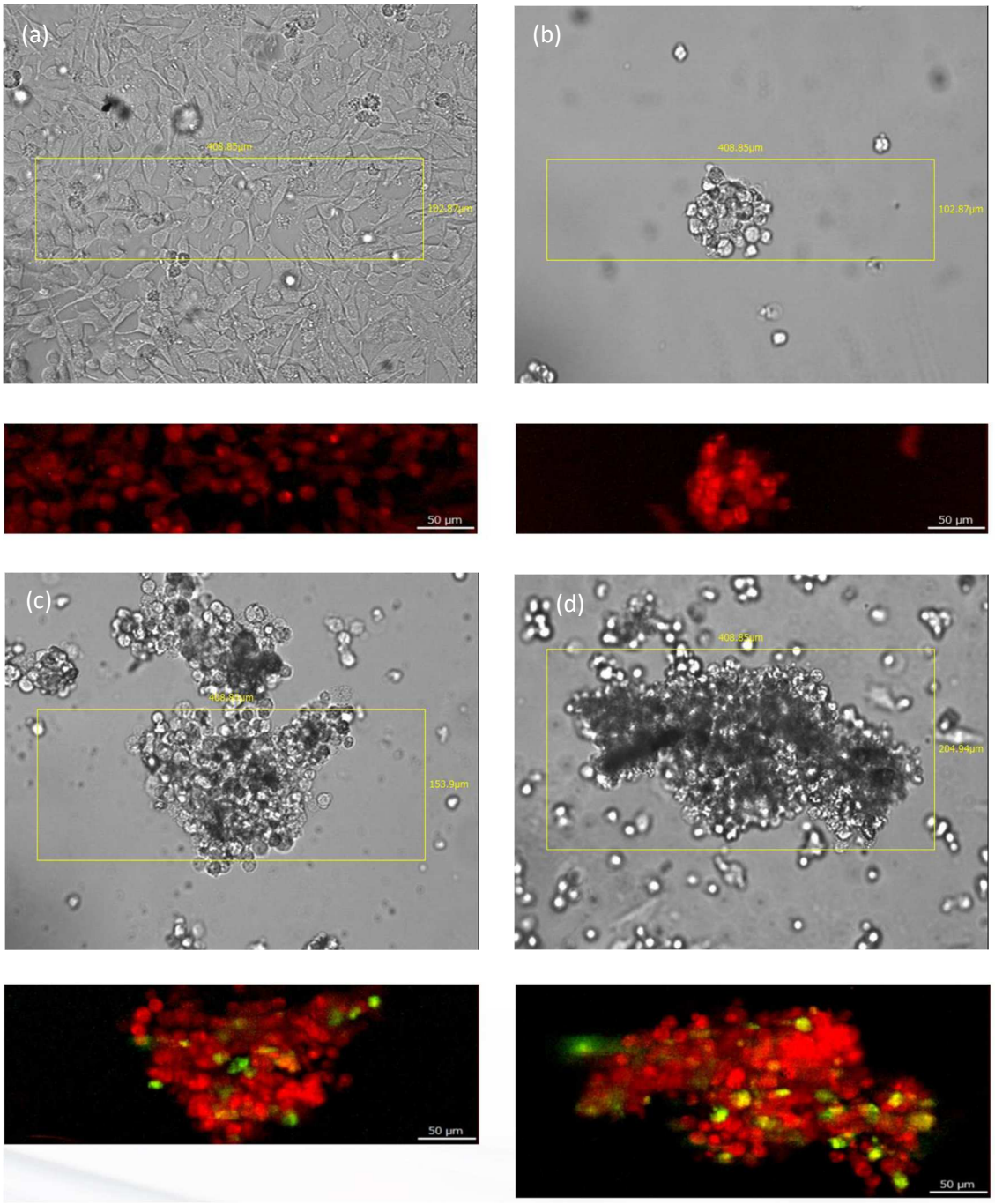

Figure 3.14: Images of the experimental SAOS-2 cultured activity test in a well of the plate without samples of silicon nitride or control. Images at 0 day of the cellular colture (a), at day 1 (b), at day 2 (c), at day 3 (d). Red zones are related to the presence of proteins while green areas indicate HA.

It is seen as with the passage of time the cells are grown and have created a complex proceeding to the formation of hydroxyapatite (green areas) and extracellular matrix (red areas).

Figure 3.15 shows the spectra of the SAOS-2 in different times.

It's possible to note how there are always the bands related to collagen and lipids between 2800 cm^{-1} and 3000 cm^{-1}. But, it's important to see how, the amount of hydroxyapatite increases over time. This fact is indicated by the increase of the peak intensity for 960 cm^{-1} band, the sign of a tissue growth and mineral compounds formation. These spectra confirm the images.

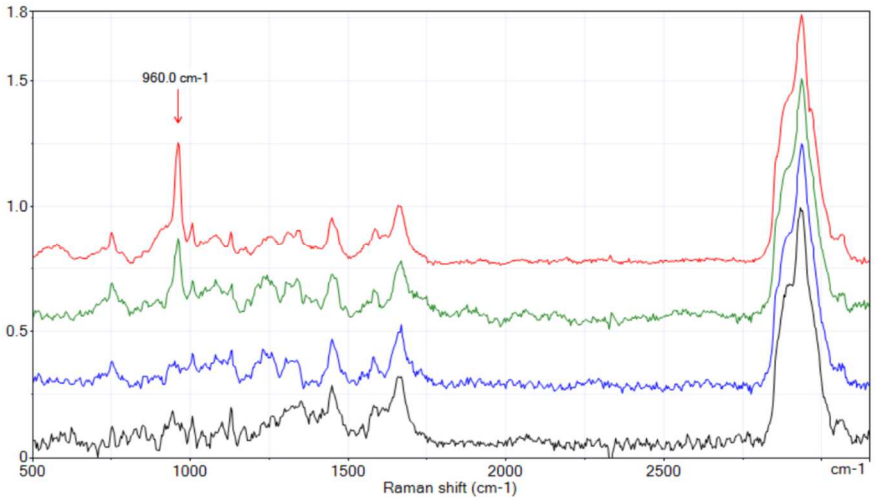

Figure 3.15: Raman spectra of SAOS-2 analyzed at different time: day 0 (black), day 1 (blue), day 2 (green), day 3 (red). The arrow at 960 cm-1 indicates the peak of hydroxyapatite (symmetric stretching vibration v1 of P-O).

The analysis carried out on cells without silicon nitride discs have provided some information regarding the proliferation and the formation of osteoid, which constitutes the first step to generate the bone tissue, making clear what happened on the surface of silicon nitride. At the beginning of the culture it has been possible to see how the cells proliferate and agglomerate going to create the osteoid, an organic matrix that is formed prior to the mineralization. It consists mainly of collagen fibers of type I and also from a small part of chondroitin sulfate and osteocalcin. After the osteoid formation, overtime, osteoblasts produce the matrix vesicles which have a roundish shape and originate directly from the cell membrane.

These vesicles substances are deposited in the matrix and, as mentioned previously, they constitute the nucleating sites for the precipitation of hydroxyapatite.
In the images obtained by Laser Raman Microscope is possible to see how there is an increase, of areas which present HA, in the middle of the protein matrix, probably due to the action of vesicles matrix after the initial formation of collagen.

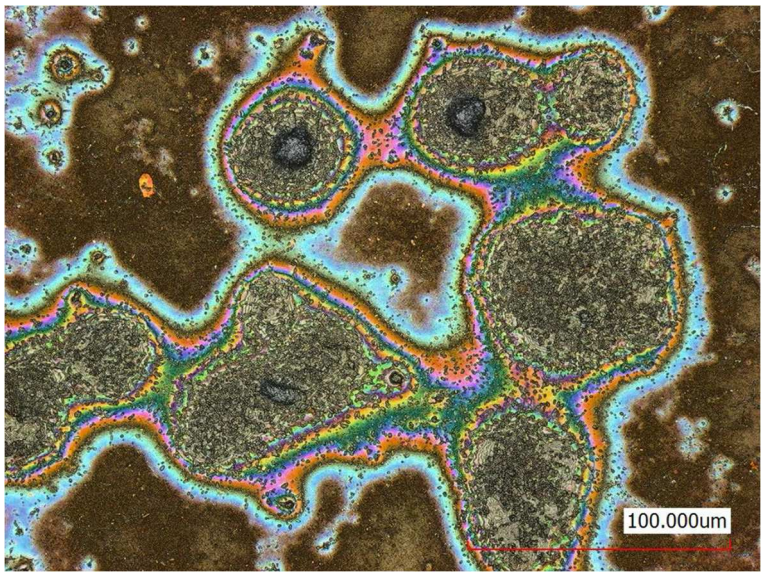

Figure 3.16: Laser micrograph of sample area characterized by osteoid complex and formation of hydroxyapatite.

All this results are confirmed also thanks to images (Figure 3.16) obtained by Laser Microscope of other silicon nitride samples treated with SAOS-2 and showing the formation of hydroxyapatite rapidly due to proliferation, agglomeration of osteoblasts and subsequent formation of the mineralized extracellular matrix.

SAOS-2 treated samples analysis show a similar behavior; cells show a mechanism similar to what occurred on the samples without disks with the formation of extracellular matrix collagen and HA. Compared to the previous case, HA areas are labeled in red while extracellular matrix proteins and lipids are labeled in green (Figures 3.17a-3.17e).
There are some differences between the images, especially in the presence of HA.
As it's possible to see, glazed samples have more red areas, (correlated to hydroxyapatite), than Ti control and the as-sintered sample which present more green areas (related to the presence of collagen). Also N_2 sample present more area related to the presence of hydroxyapatite than Ti control and the sample untreated confirming the

data obtained with Laser Microscope. Furthermore, the red areas are more widespread throughout the sample, as it's possible to see in the images.

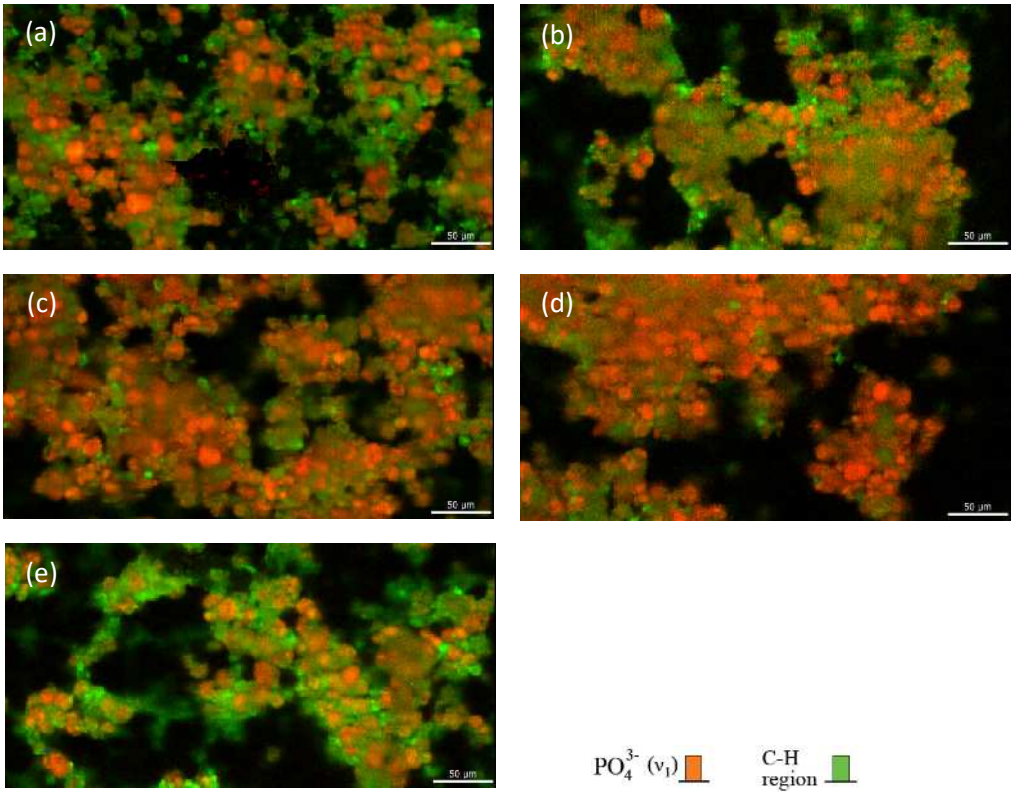

Figure 3.17: Selected area of AS (a), N2 (b), As-sintered glazed(c), polished glazed (d) and Ti samples(e). Red areas indicate hydroxiapatite presence while green areas are related to protein vibrational stretching.

The average spectrum of the samples in the Figure 3.18a indicates the presence of the band at 960 cm^{-1} and at 1044 cm^{-1} related to vibrational modes ν_1 and of the hydroxyapatite and the band at 1088 cm^{-1} which refers to the symmetric stretching mode of the substitutional carbonate and belong to the $CO_3^{2-}(\nu_1)$ in HA [240]. The intensity of the strong ν_1 band of hydroxyapatite scaled with the amount of hydroxyapatite formed, and the scaling rate among different samples was in good agreement with the data by quantitative laser-scanning microscopy. Accordingly, the improved osteoconductive behavior of the N_2-annealed sample could be confirmed by two independent techniques. The average spectrum in the Figure 3.18b shows the presence of proteins and lipids given by peaks located in the so-called CH region at frequencies in the interval 2800 ~ 3050 cm^{-1} which contains some bands related to the CH_2 stretching (ν_{ss}) and (ν_{as}) CH_3 stretching [243,257,264]. Similar to the case of hydroxyapatite, the Raman emission in the CH region shows the highest intensity for the N2-annealed sample.

Due to emission overlapping from organic and inorganic molecules and due to the relatively low spectral resolution allowed by a fast Raman *in situ* screening (i.e., ±2 cm^{-1}) on living cells, we could not detect any significant difference in the morphology of the main hydroxyapatite band among different samples.

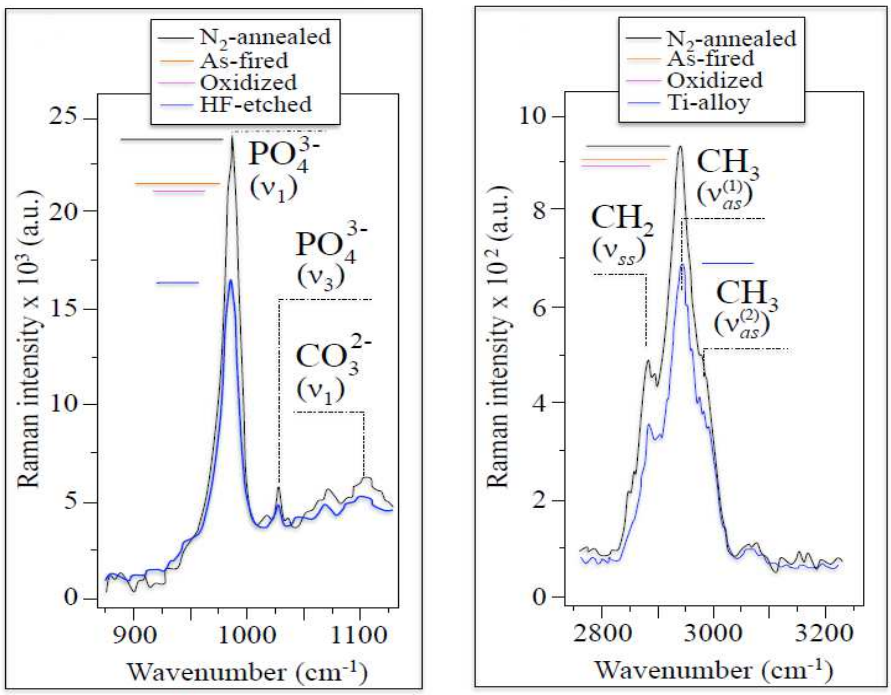

Figure 3.18: Raman spectra of as-sintered sample. In the spectrum (a), it's possible to see different main peaks related to the presence of hydroxyapatite. In the spectra (b) there are additional Raman bands related to the vibration mode of extracellular compounds.

3.3 Analysis after PDLSCs treatment

3.3.1 Raman characterization

Raman analysis were carried out on PDLSC treated polished samples.
The spectra centered at 850 cm^{-1} show in Figure 3.19 the same spectral bands of samples treated with SAOS-2. Peak with highest intensity is the one related to the P-O symmetric stretching (v_1) of hydroxyapatite at 947 cm^{-1} and at 960 cm^{-1} (peaks 2 and 3 in Figure 3.19). Spectral shape suggests a low diversity among the samples.

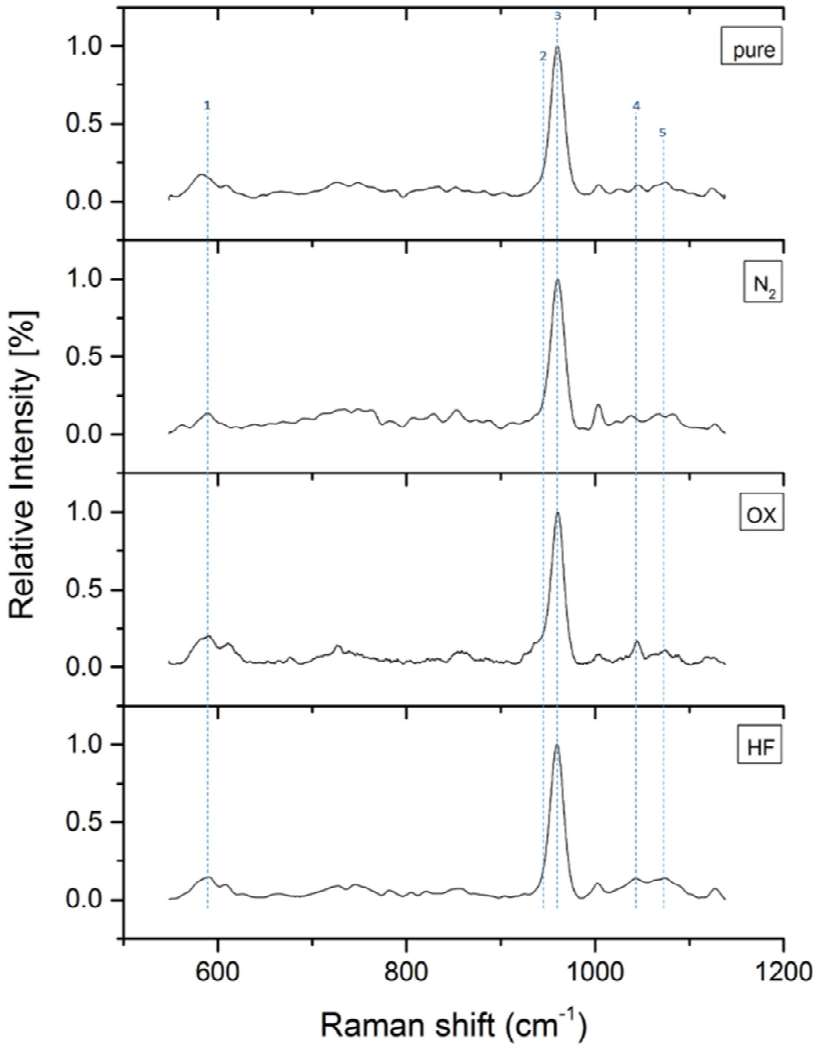

Figure 3.19: Raman spectra centered at 850 cm-1 of silicon nitride as-sintered and glazed samples treated with SAOS-2. The labeled peak (1-5) are relative to symmetric stretching of P-O (peak 2 and 3) or v4 and v3 (peak 1, 4 and 5) of PO43- of hydroxyapatite.

Indeed, there are peaks related to vibrational modes ν_3 and ν_4 of HA at 591, 1044 and 1076 cm^{-1} (peak 1,2 4 and 5 in Figure 3.19).

There are peaks of lipids, phospholipids and other biological components which constitute the vesicles matrix and collagen and favor the mineralization of extracellular matrix.

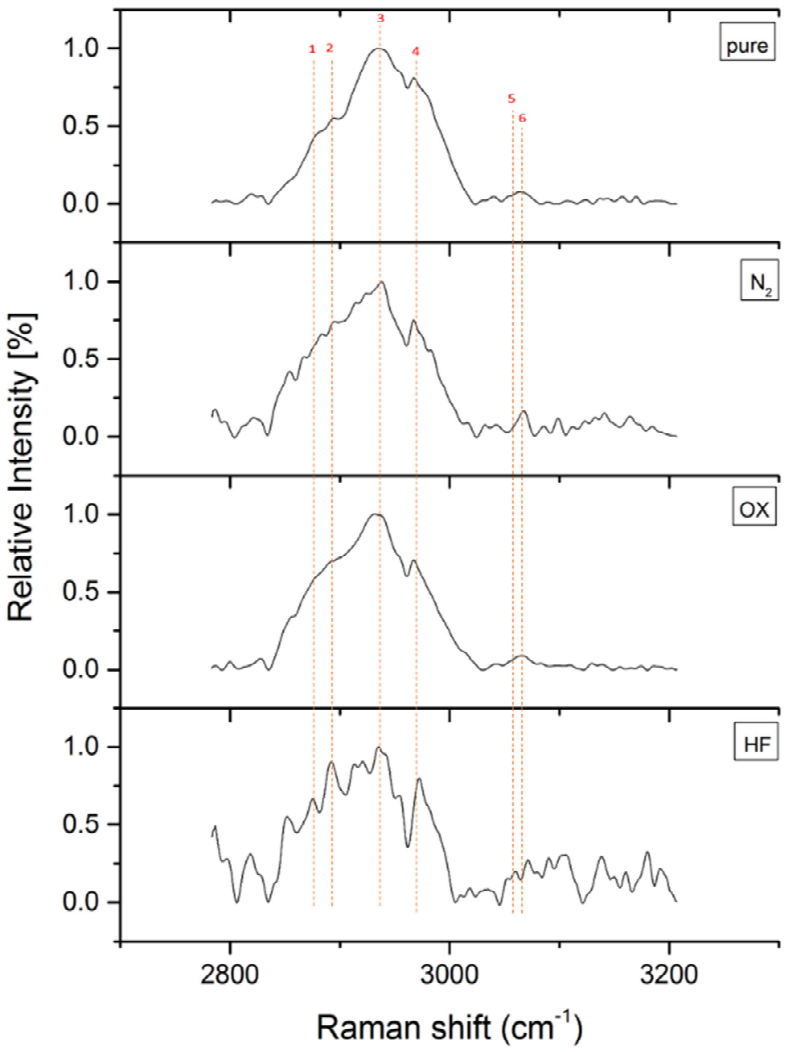

Figure 3.20: Raman spectra centered at 3000 cm^{-1} of silicon nitride as-sintered and glazed samples treated with SAOS-2. The labeled bands related to an interval between 2800 cm^{-1} and 3000 cm^{-1}contains some peaks which refer to symmetric stretching of CH and CH_2 related to protein and lipids (peak 1-4). The labeled bands at about 3050-3070 cm^{-1} regards to different peaks referred to a vibrational modes of aromatic amino acids residues and to symmetric C-H stretching of aromatic and aliphatic groups of proteins (peak 5 and 6).

Even in the case of the spectra centered at 3000 cm^{-1} (Figure 3.20) there are some peaks referred to the presence of bands assigned to the constituents of the extracellular matrix, which appear also in the spectra of as-sintered and glazed samples treated with SAOS-2.

There are peaks characteristics of symmetrical stretching of CH_2 of lipids at 2885 cm^{-1}, 2896, 2933 and 2967 cm^{-1} (peaks 1,2,3,4) and of proteins at 3054 and 3065 cm^{-1}(peaks 5 and 6). Also in this case the highest peak is referred to the vibrational stretching of CH_2 at 2933 cm^{-1}. The tables 3.6 shows all the peaks and their assignments.

RAMAN SHIFT [cm^{-1}]	ASSIGNEMENT	REFERENCE
580	Phosphatidylinositol	[243]
591	Symmetric stretching vibration of ν_4 PO_4^{3-} (phosphate of HA)	[241]
609	Cholesterol	[243]
727	C–C stretching, proline (collagen assignment)	[254]
730	Phospatidilserine	[243]
746	T (ring breathing mode of DNA/RNA bases)	[258]
764	766 cm−1 Pyrimidine ring breathing mode	[265]
827	Proline, hydroxyproline, tyrosine, ν_2 PO^{2-} stretch of nucleic acids	[241]
853	Ring breathing mode of tyrosine and C–C stretch of proline ring, Structural proteins like collagen	[251,252,259]
947	Hydroxyapatite P-O symmetric stretching	[240]
960	Hydroxyapatite P-O symmetric stretching	[240]
1003	Phenylalanine (of collagen)	[241]
1044	ν_3 PO_4^{3-} (symmetric stretching vibration of ν_3 PO_4^{3-} of HA)	[241]
1076	Symmetric stretching vibration of ν_3 PO_4^{3-} (phosphate of HA)	[240]
1088	ν_1 CO_3^{2-}, ν_3 PO_4^{3-}, ν(C–C) skeletal of acyl backbone in lipid	[241]
1125	ν(C–C) skeletal of acyl backbone in lipid	[241]
2854	CH_2 symmetric stretch of lipids, CH_2 asymmetric stretch of lipids and proteins	[256]
2885	νsCH_3, lipids, fatty acids	[257]
2896	C-H_3 symmetric stretching	[264]
2912	CH stretch of lipids and proteins	[256]
2933	CH_2 asymmetric stretch	[256]
2967	ν_{as} CH_3, lipids, fatty acids, cholesterol and cholesterol ester	[257,258]
2972	ν_{as} CH3, lipids, fatty acids	[257]
3006	ν_{as}(=C-H), lipids, fatty acids	[257]
3054	vibrational modes ν of aromatic amino acid residues	[260]
3065	C-H stretching of aromatic or aliphatic groups of proteins	[261]

Table 3.6: Peaks assignement of silicon nitride spectra.

3.3.2 Laser Microscope: distribution of HA

Images with 10X magnification were collected in order to observe the presence of hydroxyapatite and tissue growth.

Unfortunately, due to the low amount of material, other analysis were performed to 50X in order to obtain appreciable results, the surface of the samples. The figures 3.21a-d show the samples of polished silicon nitride, Ti and Al_2O_3 treated with PDLSCs.

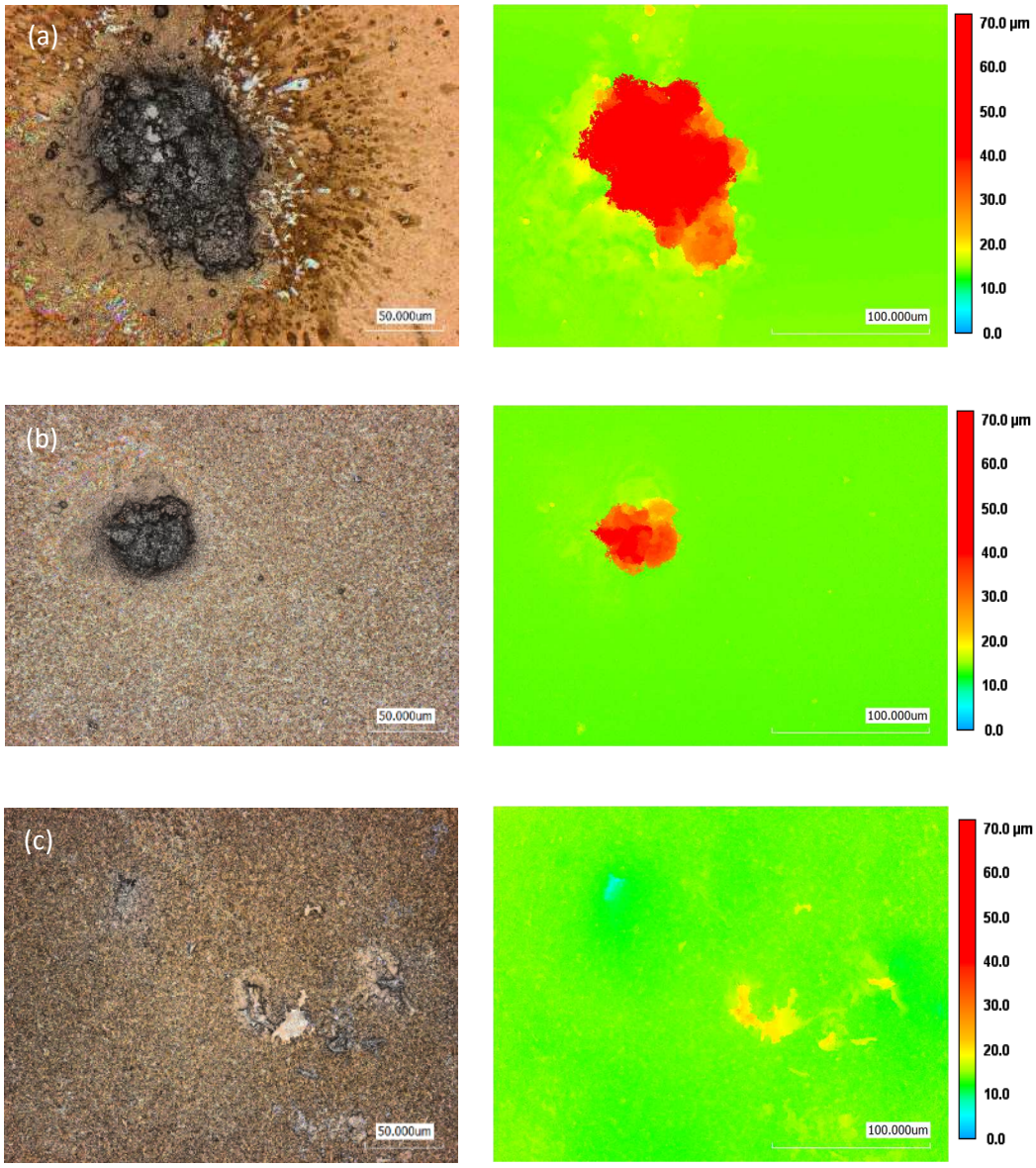

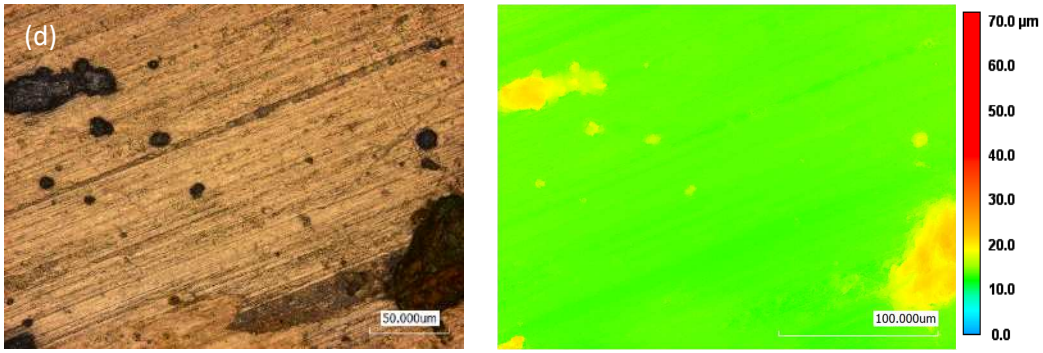

Figure 3.21: Laser micrograph of little areas characterized by the presence of mineralized extracellular matrix of silicon nitride polished samples: etched with HF (a), thermally oxidized (b), N2 annealed (c) and Ti control (d)

Analyzing the results obtained from polished samples treated with mesenchymal cells of the periodontal ligament (PDLSCs), it is seen as the cell treatment has not led to effective osseointegration and formation of mineralized extracellular matrix. Indeed, through the images obtained by Laser Microscope it's possible to see how the cells haven't adhered to the surface if not in few areas of the samples leading to the formation of some "spots" where there are traces of hydroxyapatite confirmed the spectroscopic analysis. This not adhesion of the cells probably can be due to the conditions of cell culture. Indeed, even the sample of Ti, used as a positive control, hasn't shown much more effective formation of hydroxyapatite. So, in all the samples, it hasn't been possible to carry out the quantification of the apatite by Laser Microscope precisely due to the scarcity of material to be evaluated. It can suppose, therefore, that the cause of these results is not due to the poor roughness of the samples compared to the control. A study by Kim et al. on samples of Ti having different roughness and treated with PDLSCs cells have shown expression of all genes and enzymes responsible for cell growth, even after a few days, and even in the less rough samples [266]. This study can contribute to assume that the surface charge has not led to these results, since, as repeated, even Ti control hasn't shown different behaviors. So, in the light of these consideration the main cause may coincide with a problem inherent to a not suitable cell culture protocol, since that despite the medium used and the long time taken, has not arrived at comparable results.

Chapter 4

Conclusion

This study was performed to test the ability of osseointegration possessed by the silicon nitride samples modified at the surface by verifying the formation of mineralized extracellular matrix, studying the mechanisms and comparing the results with other biomaterials commercially available like Al_2O_3 and Ti alloy.
Analyzing data, it's been possible to arrive at certain conclusions:

- Si_3N_4 as-sintered samples treated with SAOS-2 present the formation of mineralized extracelular matrix thanks Raman spectroscopy and Laser Raman Microscope that indicate the presence of HA and collagen compounds;
- N_2 annealed sample has the highest quantity of HA verified by Laser Microscope analysis; this results probably is due to the different surface charge than the other samples which confer to the sample a "zwitterionic" behaviour thanks to the presence of negative charge (SiO^-) and positive charge (NH_3^+);
- The situation on N_2 surface can be due, probably to the presence of β- Si(Y)AlON sites which can have increased positive charge distribution;
- Glazed silicon nitride samples (polished and as-sintered) have a high volume of mineralized extracellular matrix on the surface on the samples, more than that present on the surface of Ti controls. thanks to their chemical treatment, which brings a layer of β-Si(Y)AlON polarizing the surface with both positive charge and negative charge;
- As-sintered samples don't present roughness difference, so it's possible to suppose that the different growth of the mineralized cellular matrix, among the samples, is note influenced by the surface morphology; while, roughness of glazed samples is higher than control and probably could have influenced the cells and the process of osteointegration;

- Si_3N_4 polished samples used in PDLSCs treatment haven’t shown good results: low quantity of HA and extracellular matrix and it hasn’t been possible to verify the effective value by Laser Microscope;
- Also Titanium control doesn’t show high level of adhesion, cellular proliferation and mineralized extracellular matrix formation; hypothesis may be due to experimental protocol of cell colture and not to the surface characteristics of the materials (surface charge, surface roughness).

Chapter 5

Bibliography

[1] Brochers L, Reichant P. Three-dimensional stress dimensional stress distribution around a dental implant at different stages of interface development. J Dent Res, 1983, 62:155-159.

[2] Bidez MW, CE. Force transfer in implant dentistry: basic concepts and principles, J Oral Implantol, 1992 18: 264-271.

[3] Sahin S., Cehreli M., Yalcin E. The influence of funcional forces on the biomechanics of implant-supported prostheses: A review. J Dent, 2002 30:271-282.

[4] Goodacre C.J., Bernal G., Runghcharassaeng K. Clinical complications with implants and implant prostheses, J Prosthet Dent, 2003, 90: 121-132.

[5] Misch CE, Suzuki JB, Misch-Dietsh FM, Bidez MW. A positive correlation between occlsual trauma and prei-impant bone loss: literature support. Implant Dent, 2005 Jun, 14(2):108-116.

[6] Branemark P.I., Breine U., Adell R., Hansson B.O., Lindstrom J., Ohlsson A. Intra-osseous anchorage of dental prostheses. I. Experimental studies. Scan J Plast Reconstr Surg, 1969, 3:81-100.

[7] Schroeder A., Stich H., Straumann F., Sutter D. The accumulation od osteocementum areound a dental implant under physical loading. SSO Schweiz Monatsschr Zahneilkd, 1978; 88(10):1051-58.

[8] Cameron H. U., ed. Mosby, Bone implant interface, Cap. 3-4, 1994.

[9] Albrektsson T., Johansson C. Osteoinduction, osteoconduction and osteointegration, Eur Spine J, 2001, 10:96-101.

[10] Albrektsson T., Zarb G.A. Current interpretation of the osseointegrated response: clinical significance, Int J Prosthodont, 1993, 6:95-105.

[11] W.B. Saunders Company, Dorland's Illustrated Medical Dictionary, 28th Ed., 1994.

[12] Branemark P.I., Zarb G., Albrektsson T. Osteointegrazione tissutale. Osteointegrazione in odontoiatria. Ed it: Tissue integrated Prostheses Osseointegration in Clinical Dentistry, Chicago: Quintessence Publ Co 6:129-40; 10: 175-85; 11:187-97.

[13] Osborn J.F., Newesly H. Dynamic aspects of the implant-bone interface. In: Heimke G., ed. Dental implants:materials and systems. Munchen: Carl Hanser Verlag, 1980:111-23.

[14] Osborn J.F., Newesely H. Bonding osteogenesis induced by calcium phosphate ceramic implants. In: Winter GD, Gibbons DF, Plenk H, eds. Advances in biomaterials. London, etc: John Wiley, 1982; 51-8.

[15] Piattelli A., Trisi P., Emanuelli M. Bone reactions to hydroxyapatite coated dental implants in man: an histological study by means of sem, light microscope and laser scanning microscope. Int J Oral Maxillofac Implants 1993; 8: 69-74.

[16] Piattelli A., Trisi P., Cordioli G.P., Passi P. Tooth bud injury induces formation of dental hard tissues and periodontal ligament around titanium implants: a pilot study. Int J Oral Maxillofac Implants 1994; 9: 417-21.

[17] Davies J.E. Mechanisms of endosseous integration. Int J Prosthodont 1998; 11: 391-401.

[18] Tjellström, A. Osseointegrated systems and their applications in the head and neck. Adv Otolaryngol Head Neck Surg, 1989, 3, 39-70.

[19] Tjellström, A. and Håkansson, B. The bone-anchored hearing aid. Design principles, indications, and long-term clinical results. Otolaryngologic Clinica of North America, 1995,28(1): 53-72.

[20] Lundborg, G., Brånemark, P. I. and Carlsson, I. Metacarpophalangeal joint arthroplasty based on the osseointegration concept. J Hand Surg [Br], 1993, 18(6): 693-703.
[21] Möller, K., Geijer, M., Sollerman, C. and Lundborg, G. Radiographic evaluation of osseointegration and loosening of titanium implants in the MCP and PIP joints. J Hand Surg [Am], 2004,29(1): 32-8.
[22] Lundborg, G., Brånemark, P.-I. and Rose´N, B. Osseointegrated thumb prostheses: a concept for fixation of digit prosthetic devices. J Hand Surg, 1996, 21A: 216-221.
[23] Wilson J., Hench L.L. Osteoinduction. Williams DF (ed) Progress in biomedical engineering, Definitions in biomaterials. Elsevier, Amsterdam, 1987, 4, 29.
[24] Albrektsson T. The healing of autologous bone grafts after varying degrees of surgical trauma. J Bone Joint Surg [Br], 1980, 32, 403–410.
[25] Bassett C.A.L. Biological significance of piezo-electricity. Calcif Tissue Res, 1968, 1:252–261.
[26] Buch F. On electrical stimulation of bone tissue. PhD thesis, Dept of Biomaterials/Handicap Research, University of Gothenburg, Sweden, 1985, 1–139.
[27] Dealler S.F. Electrical phenomena associated with bones and fractures and the therapeutic use of electricity in fracture healing. J Med Eng Tech, 1981,5: 73–82.
[28] Yasuda I. Fundamental aspects of fracture treatment. J Kyoto Med Soc, 1953, 4:395–404.
[29] Frost H.M. The biology of fracture healing. An overview for clinicians, part I. Clin Orthop Rel Res, 1989,248: 283–293.
[30] Frost H.M. The biology of fracture healing. An overview for clinicans, part II. Clin Orthop Rel Res, 1989, 248: 294–309.
[31] Mavrogenis A.F., Dimitriou R., Parvizi J., Babis G.C. Biology of implant osseointegration. J Musculoskelet Neuronal Interact. 2009: 9(2): 61-71
[32] Marco F., Milena F., Gianluca G., Vittoria O. Peri-implant osteogenesis in health and osteoporosis. Micron, 2005; 36:630-44.
[33] Linder L., Obrant K., Boivin G. Osseointegration of metallic implants. II. Transmission electron microscopy in the rabbit. Acta Orthop Scand, 1989; 60:135-9.
[34] Soballe K. Hydroxyapatite ceramic coating for bone implant fixation. Mechanical and histological studies in dogs. Acta Orthop Scand Suppl, 1993; 255:1-58.
[35] Khan S.N., Cammisa F.P. Jr, Sandhu H.S., Diwan A.D., Girardi F.P., Lane J.M. The biology of bone grafting. J Am Acad Orthop Surg, 2005; 13:77-86.
[36] Arrington E.D., Smith W.J., Chambers H.G., Bucknell A.L., Davino N.A. Complications of iliac crest bone graft harvesting. Clin Orthop 1996; 329:300-9.
[37] Younger E.M., Chapman M.W. Morbidity at bone graft donor sites. J Orthop Trauma 1989; 3:192-195.
[38] Bet, M. R., Goissis, G., Vargas, S., & Selistre-de-Araujo, H. S. (2003). Cell adhesion and cytotoxicity studies over polyanionic collagen surfaces with variable negative charge and wettability. Biomaterials, 24, 131-137.
[39] Schneider, G. B., English, A., Abraham, M., Zaharias, R., Stanford, C., & Keller, J. (2004). The effect of hydrogel charge density on cell attachment. Biomaterials, 25, 3023- 3028.
[40] Dadsetan, M., Pumberger, M., Casper, M. E., Shogren, K., Giuliani, M., Ruesink, T., et al. (2011). The effects of fixed electrical charge on chondrocyte behavior. Acta Biomaterialia.
[41] Miho Nakamura, Akiko Nagai, Teuvo Hentunen, Jukka Salonen, Yasutaka Sekijima, Toshinori Okura, Kazuaki Hashimoto, Yoshitomo Toda, Hideki Monma, Kimihiro Yamashita. Surface Electric Fields Increase Osteoblast Adhesion through Improved Wettability on Hydroxyapatite Electret. Applied Materials & Interfaces. 2009: 1: 2181-2189
[42] M. Ohgaki, T. Kizuki, M. Katsura, K. Yamashita, Manipulation of selective cell adhesion and growth by surface charges of electrically polarized hydroxyapatite, Journal of biomedical materials research, 57 (2001) 366-373.
[43] Subhadip Bodhak, Susmita Bose, Amit Bandyopadhyay. Role of surface charge and wettability on early stage mineralization and bone cell–materials interactions of polarized hydroxyapatite. Acta Biomaterialia. 2009: 5: 2178-2188
[44] T. Kizuki, M. Ohgaki, M. Katsura, S. Nakamura, K. Hashimoto, Y. Toda, S. Udagawa, K. Yamashita, Effect of bone-like layer growth from culture medium on adherence of osteoblast-like cells, Biomaterials, 24 (2003) 941-947.
[45] Sakakura C.E., Marcantonio E. Jr, Wenzel A., Scaf G. Influence of cyclosporin A on quality of bone around integrated dental implants: a radiographic study in rabbits. Clin Oral Implants Res 2007; 8:34-9.

[46] Eder A., Watzek G. Treatment of a patient with severe osteoporosis and chronic polyarthritis with fixed implant-supported prosthesis: a case report. Int J Oral Maxillofac Implants 1999; 14:587-90.
[47] McDonald A.R., Pogrel M.A., Sharma A. Effects of chemotherapy on osseointegration of implants: a case report. J Oral Implantol 1998; 24:11-3.
[48] Rosenqvist R., Bylander B., Knutson K., Rydholm U., Rooser B., Egund N., Lidgren L. Loosening of the porous coating of bicompartmental prostheses in patients with rheumatoid arthritis. J Bone Joint Surg Am 1986; 68:538-42.
[49] Zhang H., Lewis C.G., Aronow M.S., Gronowicz G.A. The effects of patient age on human osteoblasts' response to Ti-6Al-4V implants *in vitro*. J Orthop Res 2004; 22:30-8.
[50] Mombelli A., Cionca N. Systemic diseases affecting osseointegration therapy. Clin Oral Implants Res 2006; 17(Suppl.2):97-103.
[51] Wong M.M., Rao L.G., Ly H, Hamilton L., Ish-Shalom S., Sturtridge W., Tong J., McBroom R., Josse R.G., Murray T.M. *In vitro* study of osteoblastic cells from patients with idiopathic osteoporosis and comparison with cells from non-osteoporotic controls. Osteoporos Int 1994; 4:21-31.
[52] R.E. Baier et al. Surface properties determine bioadhesive outcomes; methods and results, J Biomed Mater Res, 1984, 18:337.
[53] Boyan BD, Sylvia VL, Liu Y, Sagun R, Cochran DL, Lohmann CH, Dean DD, Schwartz Z. Surface roughness mediates its effects on osteoblasts via protein kinase A and phospholipase A2. Biomaterials 1999; 20:2305-10.
[54] Yi Deng, Xiaochen Liu, Anxiu Xu, Lixin Wang, Zuyuan Luo, Yunfei Zheng, Feng Deng, Jie Wei, Zhihui Tang, Shicheng Wei. Effect of surface roughness on osteogenesis in vitro and osseointegration in vivo of carbon fiber-reinforced polyetheretherketone–nanohydroxyapatite composite. International Journal of Nanomedicine 2015:10 1425–1447
[55] Buser D., Schenk R.K., Steinemann S., Fiorellini J.P., Fox C.H. Stich H. Influence of surface characteristics on bone integration of titanium implants. A histomorphometric study in miniature pigs. Journal of Biomedical Materials Research, 1991; 25: 889-902
[56] H.M. Frost, “Bone “mass” and the “mechanostat”: a proposal”, Anat. Rec., 1987, 219,1-9
[57] Ridzwan M.I.Z., Solehuddin Shuib, Hassan A.Y., Shokri A.A., Mohamad Ibrahim M.N. Problem of Stress Shielding and Improvement to the Hip Implant Designs: A Review. *Journal of Medical Sciences(Faisalabad)* 2007: 7 (3): 460–467.
[58] Bobyn JD et al. Producing and avoiding stress shielding. Laboratory and clinical observations of noncemented total hip arthroplasty. Clin Orthop 1992; 274:79-96.
[59] Karachalios T et al. The long-term clinical relevance of calcar atrophy caused by stress shielding in total hip arthroplasty: a 10-year, prospective, randomized study. J Arthroplasty 2004; 19: 469-475
[60] D'Ippolito G., Schiller P.C., Ricordi C., Roos B.A., Howard G.A. Age-related osteogenic potential of mesenchymal stromal stem cells from human vertebral bone marrow. J Bone Miner Res 1999; 14:1115-22.
[61] Fini M., Giavaresi G., Torricelli P., Borsari V., Giardino R., Nicolini A., Carpi A. Osteoporosis and biomaterial osteointegration. Biomed Pharmacother 2004; 58: 487-93.
[62] Augat P., Simon U., Liedert A., Claes L. Mechanics and mechano-biology of fracture healing in normal and osteoporotic bone. Osteoporos Int 2005; 16(Suppl.2): S36-43.
[63] Albrektson T., Sennerby L. Direct bone anchorage of oral implants: clinical and experimental considerations of the concept of osseointegration. Int J. Prostodont. 1990: 3: 30-41
[64] Gotfredsen K., Rostrup E., Hjorting-Hansen E., Stoltze K., Budtz-Jorgensen E., Histological and Histomorphometrical evaluation of tissue reactions adjacent to endosteal implants in monkeys. Clinical Oral IMplant Research. 1991: 2: 30-37.
[65] Geissler U., Hempel U., Wolf C., Scharnweber D., Worch H., Wenzel K. Collagen type I coating of Ti6A14V promotes adhesion of osteoblasts. J Biomed Mater Res 2000; 51: 752-60.
[66] Frosch K.H., Sondergeld I., Dresing K., Rudy T., Lohmann C.H., Rabba J., Schild D., Breme J., Stuermer K.M. Autologous osteoblasts enhance osseointegration of porous titanium implants. J Orthop Res 2003; 21: 213-23.
[67] Eberhardt C., Habermann B., Tiemann S., Bauss F., Kurth A.A. Improvement of osseointegration of cementless metal implant under ibandronate is dosedependent. Bone 2006; 38: S42-S64.
[68] Gabet Y., Muller R., Levy J., Dimarchi R., Chorev M., Bab I., Kohavi D. Parathyroid hormone 1-34 enhances titanium implant anchorage in low-density trabecular bone: a correlative micro-computed tomographic and biomechanical analysis. Bone 2006; 39: 276-82.

[69] Fogh J., Fogh J.M., Orfeo T. "One hundred and twenty-seven cultured human tumor cell lines producing tumors in nude mice". *J Natl Cancer Inst.* 1977, 59 (1): 221–226.
[70] Rodan S.B., Imai Y., Thiede M.A., Wesolowski G., Thompson D., Bar-Shavit Z., Shull S., Mann K., Rodan G.A. "Characterization of a human osteosarcoma cell line (Saos-2) with osteoblastic properties". *Cancer Res.* 1987: 47 (18): 4961–6.
[71] Hausser H.J., Brenner R.E. "Phenotypic instability of Saos-2 cells in long-term culture". *Biochem. Biophys. Res. Commun.* 2005: 333 (1): 216–22.
[72] McQuillan D.J., Richardson M.D., Bateman J.F. "Matrix deposition by a calcifying human osteogenic sarcoma cell line (SAOS- 2)". *Bone* 1995: 16 (4): 415–26.
[76] Fernandes R.J., Harkey M.A., Weis M., Askew J.W., Eyre D.R. The post-translational phenotype of collagen synthesized by SAOS-2 osteosarcoma cells. Bone 2007: 40: 1343-1351
[74] Czekanska E.M., Stoddart M.J., Richards R.G., J.S. Hayes, in search of an osteoblast cell model for *in vitro* research, EuropeanCells and Materials, 2012: 24: 1-1
[75] Vohra S., Hennessy K.M., Sawyer A.A., Zhuo Y., Bellis S.L. Comparison of mesenchymal stem cell and osteosarcoma cell adhesion to hydroxyapatite. J Mater Sci Mater Med, 2008: 19: 3567-3574.
[76] Liu W., Konermann A., Guo T., J¨ager A., Zhang L., Jin Y., CanonicalWnt signaling differently modulates osteogenic differentiation of mesenchymal stem cells derived from bone marrow and from periodontal ligament under inflammatory conditions, *Biochimica et Biophysica Acta*, 2014, vol. 1840, no. 3, 1125–1134.
[77] Wang L., Shen H., Zheng W. Characterization of stem cells from alveolar periodontal ligament, *Tissue Engineering— Part A*, 2011, vol. 17, no. 7-8, 1015–1026.
[78] Wada, Menicanin D., Shi S., Bartold P. M., Gronthos S., Immunomodulatory properties of human periodontal ligament stem cells, *Journal of Cellular Physiology*, 2009, vol. 219, no.3, 667–676.
[79] Wenjun Zhu, Min Liang, Periodontal Ligament Stem Cells: Current Status, Concerns, and Future Prospects, Hindawi Publishing Corporation. Stem cells International, 2015: 11 pages.
[80] Feng F., Akiyama K., Liu Y., Utility ofPDL progenitors for in vivo tissue regeneration: a report of 3 cases, *Oral Diseases*, 2010, vol. 16, no. 1, 20–28.
[81] Zhu W., Tan Y., Qiu Q., Comparison of the properties of human CD146+ and CD146− periodontal ligament cells in response to stimulationwith tumour necrosis factor α, *Archives of Oral Biology*, 2013, vol. 58, no. 12, 1791–1803.
[82] Song J. S., Kim S.-O., Kim S.-H. In vitro and in vivo characteristics of stem cells derived from the periodontal ligament of human deciduous and permanent teeth, *Tissue Engineering, Part A*, 2012, vol. 18, no. 19-20, 2040- 2051.
[83] Iwasaki K., Komaki M., Yokoyama N. "Periodontal regeneration using periodontal ligament stem cell-transferred amnion," *Tissue Engineering Part A*, 2014, vol. 20, no. 3-4, 693– 704.
[84] Ding G., Liu Y., Wang W. Allogeneicperiodontal ligament stem cell therapy for periodontitis in swine, 2010 *Stem Cells*, vol. 28, no. 10, 1829–1838.
[85] Liu, Xu J., Ding G. Periodontal ligament stem cells regulate b lymphocyte function via programmed cell death protein 1, *Stem Cells*, 2013, vol. 31, no. 7, 1371–1382.
[86] Gay I.C., CHEN S., MacDougall M. Isolation and characterization of multipotent human periodontal ligament stem cells. Orthod Craniofacial Res. 2007: 10: 149–160
[87] Ramamoorthi M., Bakkar M., Jordan J., Tran S.D., Osteogenic Potential of Dental Mesenchymal Stem Cells in Preclinical Studies: A Systematic Review Using Modified ARRIVE and CONSORT Guidelines. Hindawi Publishing Corporation, Stam Cells International. 2015.
[88] Moshaverinia A., Chen C., Akiyama K. Encapsulated dental-derived mesenchymal stem cells in an injectable and biodegradable scaffold for applications in bone tissue engineering, *Journal of Biomedical Materials Research—Part A*, 2013 vol. 101, no. 11, 3285–3294.
[89] Moshaverinia A., Chen C., Xu X. Bone regeneration potential of stem cells derived from periodontal ligament or gingival tissue sources encapsulated in RGD-modified alginate scaffold, *Tissue Engineering—Part A*, 2014, vol. 20, no. 3-4, pp. 611–621.
[90] Minkle Gulati, Vishal Anand, Vivek Govila, Nikil Jain, Pavitra Rastogi, Rohit Bahuguna, Bhargavi Anand·Periodontio-integrated implants: A revolutionary concept. Dent Res J (Isfahan). 2014 Mar-Apr; 11(2): 154–162.
[91] Warrer K., Karring T., Gotfredsen K. Periodontal ligament formation around different types of dental titanium implants. I. The self-tapping screw type implant system. J Periodontol. 1993; 64: 29–34.

[92] rabe M., Hosokawa R., Chiba D., Sato Y., Akagawa Y. Morphogenetic behavior of periodontium on inorganic implant materials: An experimental study of canines. J Biomed Mater Res. 2000; 49: 17–24.
[93] Jahangiri L., Hessamfar R., Ricci J.L. Partial generation of periodontal ligament on endosseous dental implants in dogs. Clin Oral Implants Res. 2005; 16: 396–401.
[94] Giannobile W.V. Getting to the root of dental implant tissue engineering. J Clin Periodontol. 2010; 37:747–9.
[95] Rahaman M.N., Yao A., Bal B.S., Garino J.P., Ries M.D., Ceramics for prosthetic hip and knee joint replacement, J. Am. Ceram. Soc. 2007, 90 1965–1988.
[96] Mazzocchi M., Bellosi A., On the possibility of silicon nitride as a ceramic for structural orthopaedic implants. Part I: processing, microstructure, mechanical properties, cytotoxicity, J. Mater. Sci. – Mater. Med. 2008, 19, 2881–2887.
[97] Mazzocchi M., Gardini D., Traverso P.L., Faga M.G., Bellosi A., On the possibility of silicon nitride as a ceramic for structural orthopaedic implants. Part II: chemical stability and wear resistance in body environment, J. Mater. Sci. – Mater. Med. 2008, 19, 2889–2901.
[98] Bal B.S., Rahaman M.N., Orthopedic applications of silicon nitride ceramics, Acta Biomater. 2012, 8, 2889–2898.
[99] Taylor R.M., Bernero J.P., Patel A.A., Brodke D.S., Khandkar A.C., Silicon nitride–a new material for spinal implants, J. Bone Joint Surg. Br. 92, 2010, 133.
[100] Riley F.L. Silicon nitride and related materials. J Am Ceram Soc. 2000; 83: 245–65.
[101] P. Schützenberger, Compt. Rend. 2, 1879: p 644.
[102] Weiss L., Engilhardt t. “Uber die Stickstoffverbindungen des Siliciums. Z. Anorg. Allgem Chem. 1910: 65 (1):38-104.
[103] Friederich, E.; Sittig, L. Herstellung Und Eigenschaften von Nitriden. J. Inorg. Gen. Chem. 1925, 143, 293–320
[104] Brook R.J., editor. Concise encyclopedia of advanced ceramic materials. Oxford: Pergamon Press; 1991.
[105] Neumann A., Unkel C., Werry C. Osteosynthesis in facial bones. Silicon nitride ceramic as material. HNO 2006; 54: 937–42.
[106] Neumann A., Unkel C., Werry C. Prototype of a silicon nitride ceramic based miniplate osteofixation system for the midface. Otolaryngol Head Neck 2006; 134: 923–30.
[107] Bal B.S., Khandkar A., Lakshminarayanan R., Clarke I., Hoffman A.A., Rahaman M.N. Testing of silicon nitride ceramic bearings for total hip arthroplasty. J Biomed Mater Res B 2008; 87: 447–54.
[108] Taylor R.M., Bernero J.P., Patel A.A., Brodke D.S., Khandkar A.C. Silicon Nitride - A New Material for Spinal Implants, 2010: *J. Bone Jt. Surg.*, 92-Br [Supp I] 133.
[109] Howlett C.R., McCartney E., Ching W. The effect of silicon nitride ceramic on rabbit skeletal cells and tissue. An in vitro and in vivo investigation. Clin Orthop Relat Res 1989; 244: 293–304.
[110] Neumann A., Jahnke K., Maier H.R., Ragoß C. Biocompatibility of silicon nitride ceramic in vitro. A comparative fluorescence-microscopic and scanning electron-microscopic study. Laryngorhinootologie 2004; 83: 845–51.
[111] Hardie D., Jack K.H., Crystal Structures of SIlicon Nitride. Nature. 1957: 180: 332-333.
[112] Turkdogan T., Bills P.M., Tippett V.A. Silicon-nitrides:Some physico-chemical properties. Journal of Applied Chemistry. 1958: 8(5): 296-302.
[113] Shyan-Lung Chung, Chih-Wei Chang. Carbothermal reduction and nitridation synthesis of silicon nitride by using solution combustion synthesized precursors. J Mater Sci, 2009: 44:3784–3792
[114] Nuray Karakus, A. Osman Kurt, Cihangir Duran, Cem Ozturk, H. Ozkan Toplan. Sintering behaviour of silicon nitride powders produced by carbothermal reduction and nitridation. Advanced Powder Technology, 2013: 24, 697–702.
[115] Wang W., Hadfield M., Wereszczak A.A. Surface strength of silicon nitride in relation to rolling contact performance. Ceram Int 2009; 35: 3339–46.
[116] Kim H.D., Han B.D., Park D.S., Lee B.T., Becher P.F. Novel Two-Step Sintering Process to Obtain a Bimodal Microstructure in Silicon Nitride, *J. Am. Ceram. Soc.*, 2002, 85 [1] 245–252.
[117] Becher P.F., Sun E.Y., Plucknett K.P., Alexander K.B., Hsueh C., Lin H., Waters S.B., Westmoreland C.G. Microstructural Design of Silicon Nitride with Improved Fracture Toughness: I, Effects of Grain Shape and Size, *J. Am. Ceram. Soc.*, 1998: 81 [11] 2821–2830.

[118] Sun E.Y., Becher P.F., Plucknett K.P., Hsueh C.-H., Alexander K.B., Waters S.B. Microstructural Design of Silicon Nitride with Improved Fracture Toughness: II, Effects of Yttria and Alumina Additives, *J. Am. Ceram. Soc.*, 1998: 81 [11]: 2831–2840.

[119] Becher P.F., Microstructural Design of Toughened Ceramics, *J. Am. Ceram. Soc.*, 1991: 74 [2]: 255–269.

[120] Choi S.R., Salem J.A., Crack-Growth Resistance of in Situ-Toughened Silicon Nitride, *J. Am. Ceram. Soc.*, 1994: 77 [4] 1042–1046.

[121] Sajgalik P., Dusza J., Hoffman M. J. Relationship Between Microstructure, Toughening Mechanisms, and Fracture Toughness of Reinforced Silicon Nitride Ceramics, *J. Am. Ceram. Soc.*, 1995: 78 [10]: 2619–24.

[122] Mutoh Y., Yamaishi K., Miyahara N., Oikawa T. Brittle-to-Ductile Transition in Silicon Nitride pp. 427–40 in *Fracture Mechanics of Ceramics*, Vol. 10. Edited by R. C. Brady, D. P. H. Hasselman, D. Munz, M. Sakai, and V. Ya. Shevchenko. Plenum Press, New York, 1992.

[123] Quinn G.D., Morrell R. Design Data for Engineering Ceramics: A Review of the Flexure Test, *J. Am. Ceram. Soc.*, 1991: 74 [9]: 2037–2066.

[124] Li C.W., Yamanis J. Super-Tough Silicon Nitride with R-Curve Behavior, *Ceram. Eng. Sci. Proc.*, 1989:10 [7-8] 632–645.

[125] Li C.-W., Lui S.-C., Goldacker J., Relation between Strength, Microstructure, and Grain-Bridging Characteristics in In Situ Reinforced Silicon Nitride, *J. Am. Ceram. Soc.*, 1995: 78 [2]: 449–459.

[126] Hirosaki N., Akimune Y., Mitomo M. Effect of Grain Growth of ß-Silicon Nitride on Strength, Weibull Modulus, and Fracture Toughness," *J. Am. Ceram. Soc.*, 1993: 76 [7]: 1892–1894.

[127] Krstic Z., Yu Z., Krstic V.D. Effect of Grain Width and Aspect Ratio on Mechanical Properties of Si3N4 Ceramics, 2007: *J. Mater. Sci.*, 42 [14] 5431–5436.

[128] Tanaka I., Pezzotti G., Okamoto T., Miyamoto Y., Koizumi M. Hot Isostatic Press Sintering and Properties of Silicon Nitride without Additive, *J. Am. Ceram. Soc.*, 1989: 72 [9]: 1656–1660.

[129] Pezzotti G., Yamamoto K. Artificial Hip Joints: The Biomaterials Challenge, *J. Mech. Behav. Biomed. Mater.*, 2014: 31 3–20.

[130] Melendezmartinez J. Creep of Silicon Nitride," *Prog. Mater. Sci.*, 2004: 49 [1] 19–107.

[131] Bonnell D., Tien T., Ruhle M. Controlled crystallization of the amorphous phase in silicon nitride ceramics, *J. Am. Ceram. Soc.*, 1987: 70 [7] 460–465.

[132] Lin C.-H., Komeya K., Meguro T., Tatami J., Abe Y., Komatsu M. Corrosion Resistance of Wear Resistant Silicon Nitride Ceramics in Various Aqueous Solutions, *J. Ceram. Soc. Japan*, 2003: 111 [7] 452–456.

[133] Herrmann M., Schilm J., Hermel W., Michaelis A. Corrosion Behavior of Silicon Nitride Ceramics in Aqueous Solutions, *J. Ceram. Soc. Japan*, 2006: 114 [11] 1069–1075.

[134] Mikeska K.R., Bennison S.J., Grise S.L. Corrosion of Ceramics in Aqueous Hydrofluoric Acid, *J. Am. Ceram. Soc.*, 2000: 83 [5] 1160–1164.

[135] Sharkaway S.W., El-Aslabi A.M. Corrosion of Silicon Nitride Ceramics in Aqueous HCL and HF Solutions at 27-80°C, *Corros. Sci.*, 1998: 40 [7] 1119–1129.

[136] Sato T., Tokunaga Y., Endo T., Shimada M., Komeya K., Nishida K., Komatsu M., Kameda T. Corrosion of Silicon Nitride Ceramics in Aqueous HF Solutions," *J. Mater. Sci.*, 1988: 23 3440–3446.

[137] Monteverde F., Mingazzini C., Giorgi M., Bellosi A., Corrosion of Silicon Nitride in Sulphuric Acid Aqueous Solution, *Corros. Sci.*, 2001: 43 [10] 1851–1863.

[138] Seipel B., Nickel K.G. Corrosion of Silicon Nitride in Aqueous Acidic Solutions: Penetration Monitoring, *J. Eur. Ceram. Soc.*, 2003: 23 [4] 595–602.

[139] Schilm J., Herrmann M., Michael G. Kinetic Study of the Corrosion of Silicon Nitride Materials in Acids, *J. Eur. Ceram. Soc.*, 2003: 23 [4] 577–584.

[140] Herrmann M., Schilm J., Michael G., Meinhardt J., Flegler R. Corrosion of Silicon Nitride Materials in Acidic and Basic Solutions and Under Hydrothermal Conditions, *J. Eur. Ceram. Soc.*, 2003: 23 [4] 585–594.

[141] Uchida N., Uematsu K., Kurita T., Yoshimoto K., Suzuki Y. Corrosion of Silicon Nitride Ceramics by Nitric Acid; 1992, pp. 533–538 in *Mater. Res. Symp. Proc.* Cambridge University Press, Cambridge, UK.

[142] Oda K., Yoshio T., Miyamoto Y., Koizumi M., "Hydrothermal Corrosion of Pure, Hot Isostatically Pressed Silicon Nitride," *J. Am. Ceram. Soc.*,1993: 76 [5] 1365–1368.

[143] Fox D.S., Jacobson N.S. Molten-Salt Corrosion of Silicon Nitride: I , Sodium Carbonate, *J. Am. Ceram. Soc.*,1988: 71 [2] 128–138.

[144] Jacobson N.S., Fox D.S., Si F. Molten-Salt Corrosion of Silicon Nitride: II, Sodium Sulfate, *J. Am. Ceram. Soc.*, 1988: 71 [2] 139–48.
[145] Galusková D., Hnatko M., Galusek D., Šajgalík P. Corrosion of Structural Ceramics Under Subcritical Conditions in Aqueous Sodium Chloride Solution and in Deionized Water. Part I: Dissolution of Si3N4-Based Ceramics, *J. Am. Ceram. Soc.*, 2011: 94 [9] 3035–3043.
[146] Sato T., Tokunaga Y., Endo T., Shimada M., Komeya K., Komatsu M., Kameda T. Corrosion of Silicon Nitride Ceramics in Aqueous Hydrogen Chloride Solutions, 1988: *J. Am. Ceram. Soc.*, 71 [12] 1074–1079.
[147] Dante R.C., Kajdas C.K. A Review and a Fundamental Theory of Silicon Nitride Tribochemistry, *Wear*, 2012: 288 27–38.
[148] Pezzotti G. Bioceramics for Hip Joints: The Physical Chemistry Viewpoint, *Materials (Basel).*, 2014: 7 4367–4410.
[149] Griss, P., Wener, E., Heimke, G. Alumina ceramic, bioglass, and silicon nitride: a comparative biocompatibility study. In: *Mechanical Properties of Biomaterials*. Edited by Hasting, G.W. and Williams, D.F., pp. 217-226, 1980.
[150] Howlett C.R., Mccartney, E., Ching, W. *Clin Orthop*. 1989, 244, 293–304.
[151] Kue R., Sohrabi A., Nagle D., Frondoza C., Hungerford D. *Biomaterials*. 1999, 20, 1195-1201.
[152] Sohrabi A., Holland C., Kue R., Nagle D., Hungerford D.S., Frondoza C.G. *J Biomed Mater Res*. 2000, 50, 43-49.
[153] Amaral M., Lopes M.A., Santos J.D., Silva R.F. *Biomaterials*. 2002, 23, 4123-4129.
[154] Guedes e Silva, Higa O.Z., Bressiani J.C. *Mater Sci Eng C*. 2004, 24, 643-646.
[155] Neumann A., Jahnke K., Maier H., Ragoss C. Biocompatibilty of silicon nitride ceramic in vitro. A comparative fluorescence-microscopic and scanning electron-microscopic study, Laryngo-rhino-otologie, 2004: 83 845-851.
[156] Cappi B., Neuss S., Salber J., Telle R., Knüchel R., Fischer H.Cytocompatibility of high strength non-oxide ceramics. J Biomed Mater Res A. 2010 Apr;93(1):67-76.
[157] Sorrell, C., Hardcastle P.H., Druitt R.K., Howlett C.R., McCartney E.R. Results of 15-years clinical study of reaction bondend silicon nitride intervertebral spacers. IN: 7th WORD BIOMATERIAL CONGRESS, May 17-21, 2004, Sydney. Proceedings... Sydney: *Australian Society for Biomaterials*, 1004, p. 1872.
[158] Newmann A., Unkel C., Werry C., Herborn C.U., Maier H.R., Ragoβ C., Jahnke K. Prototype of a silicon nitride osteofixation system for the midface. *Otolarygology-Head and Neck Surgery*, v. 134, p. 923-930, 2006.
[159] Guedes e Silva C.C., König B., Carbonari M.J., Yoshimoto M., Allegrini S., Bressiani J.C. Tissue response around silicon nitride implants in rabbits, Journal of Biomedical Materials Research Part A, 2008: 84: 337-343.
[160] Andreson M.C., Olsen R. Bone ingrowth into porous silicon nitride. *J Biomed Mat Res A*. 2009, 92, 1598-1605
[161] Mazzocchi M., Bellosi A. *J Mater Sci Mater Med*. 2008, 19, 2881–2887.
[162] Mazzocchi M., Gardini D., Traverso P.L., Faga M.G., Bellosi A. *J Mater Sci Mater Med*. 2008, 19, 2889–2901.
[163] Thompson D.P. Materials Science – Cooking up Tougher Ceramics, Nature 417 (2002) 237.
[164] K.H. Jack W.I. Wilson, Ceramics Based on the Si-Al-O-N and Related Systems, Nature Physic Science 238 (1972) 28–29.
[165] Jack K.H. Review: SiAlONs and Related Nitrogen Ceramics, Journal of Materials Science 11 (1976) 1135–1158.
[166] Lewis M.H., Powell B.D., Drew P., Lumby R.J., North B., Taylor A.J. The Formation of Single-Phase Si-Al-O-N Ceramics, Journal of Materials Science 12 (1977) 61-74.
[167] Notingher I., Jell G., Lohbauer U., Salih V., Hench L.L. In situ noninvasive spectral discrimination between bone cell phenotypes used in tissue engineering, Journal of cellular biochemistry, 92 (2004) 1180-1192.
[168] Swain R.J., Kemp S.J., Goldstraw P., Tetley T.D., Stevens M.M. Assessment of cell line models of primary human cells by Raman spectral phenotyping, Biophysical journal, 2010: 98 1703-1711.
[169] Wild S., Grieveson P., Jack K.H. Special ceramics, in: P. Popper (Ed.), Stoke-on-Trent, 1972: vol. 5, British Ceramic Research Association, p. 385.
[170] Lee D.D., Kang S.J.L., Petzow G., Koon D.K. Effect of a to b phase transition on the sintering of silicon nitride ceramics, Journal of the American Ceramic Society, 1990: 73: 767–769.
[171] Mandal H., Thompson D.P., Ekstrom T. Reversible a-sialon transformation in heat-treated SiAlON ceramics, Journal of the European Ceramic Society, 1993: 12: 421–429.

[172] Lee S.K., Lee K.S., Lawn B.R., Kim D.K. Effect of starting powder on damage resistance of silicon nitrides, Journal of the American Ceramic Society, 1998: 81: 2061–2070.
[173] Hampshire S., K.H. Jack, in: F.L. Riley (Ed.), Progress in Nitrogen Ceramics, Martinus Nijhoff Publishers, Boston, 1983, pp. 225–230.
[174] Ziegler G., Heinrich J., Wotting G. Relationships between processing, microstructure and properties of dense and reaction-bonded silicon nitride, Journal of Materials Science, 1987: 22: 3041–3086.
[175] Mandal H., Ekström T., Thompson D.P. Reversible SiAlON Transformation in Heat-Treated SiAlON Ceramics, Journal of European Ceramic Society, 1993: 12: 421–429.
[176] Camescu N., Thompson D.P., Mandal H. Effect of Starting Composition, Type of Rare-Earth Sintering Additive, and Amount of Liquid Phase on □□□-SiAlON Transformation, Journal of European Ceramic Society, 1997: 17: 599–613.
[177] Kleebe H. J., Pezzotti G., Ziegler G. Microstructure and Fracture Toughness of Si3N4 Ceramics: Combined Roles of Grain Morphology and Secondary Phase Chemistry, Journal of American Ceramic Society, 1999: 82: 1857–1867.
[178] Wiederhorn S.M., Krause R.F., Lofaj F., Taffner U. Creep behavior of improved high temperature silicon nitride, Key Enginnering Materials, 2005: 287: 381-392.
[179] Hampshire S. Silicon nitride ceramics-review of structure, processing and properties. Journal of Achievements in Materials and Manufacturing Engineering. 2007: 24 (1): 43-50
[180] Clarke D.R. On the Equilibrium Thickness of Intergranular Glass Phases in Ceramic Materials, Journal of American Ceramic Society, 70 (1987) 15–22.
[181] Becher P.F., Sun E.Y., Plucknett K.P., Alexander K.B., Hsueh C.H., Lin H.T., Waters S.B., Westmoreland C.G., Kang E.S., Hirao K., Brito M. E. Microstructural Design of Silicon Nitride with Improved Fracture Toughness: I, Effects of Grain Size and Shape, Journal of American Ceramic Society, 1998: 81: 2821–2830.
[182] Bock R.M., McEntire B.J., Bal B.S., Rahaman M.N., Boffelli M., Pezzotti G. Surface modulation of silicon nitride ceramics for orthopaedic applications, Acta biomaterialia, 2015: 26: 318-330.
[183] Rahaman M., Boiteux Y., DeJonghe L. Surface characterization of silicon nitride and silicon carbide powders, Bull. Am. Ceram. Soc. 1986: 65: 1171–1176.
[184] NIST-JANAF Thermochemical Tables, <http://kinetics.nist.gov/janaf/>
[185] Raider S.I., Flitsch R., Aboaf J.A., Pliskin W.A. Surface oxidation of silicon nitride films, J. Electrochem. Soc. 1976: 123: 560–565.
[186] Bergström L., Pugh R.J. Interfacial characterization of silicon nitride powders, J. Am. Ceram. Soc. 1989: 72: 103–109.
[187] Hackley V.A., Sen Wang P., Malghan S.G. Effects of soxhlet extraction nitride powders on the surface oxide layer of silicon nitride powders, Mater. Chem. Phys. 1993: 36: 112–118.
[188] Butt D.P., Albert D., Taylor T.N. Kinetics of thermal oxidation of silicon nitride powders, J. Am. Ceram. Soc. 1996: 79: 2809–2814.
[189] Szépvölgyi J., Mohai I., Gubicza J. Studies on atmospheric ageing of nanosized silicon nitride powders, Key Eng. Mater. 2004: 264–268: 2311–2314.
[190] Busca G., Lorenzelli V., Porcile G., Baraton M.I., Quintard P., Marchand R. FT-IR study of the surface properties of silicon nitride, Mater. Chem. Phys. 1986: 14: 123–140.
[191] Mezzasalma S. Characterization of silicon nitride surface in water and acid environment: a general approach to the colloidal suspensions, J. Colloid Interface Sci. 1996: 180: 413–420.
[192] Iler R.K., The Chemistry of Silica, Wiley, New York, NY, 1979.
[193] Greil P., Nitzsche R., Friedrich H., Hermel W. Evaluation of oxygen content on silicon nitride powder surface from the measurement of the isoelectric point, J. Eur. Ceram. Soc. 1991: 7: 353–359.
[194] Sonnefeld J. Determination of surface charge density parameters of silicon nitride, Colloids Surf. A, 1996: 108: 27–31.
[195] Reed J.S. Principles of Ceramics Processing, second ed., Wiley, New York, 1195.
[196] Israelachvili J.N. Intermolecular and Surface Forces, third ed., Academic Press, London, 2011.
[197] Greil P., Processing of silicon nitride ceramics, Mater. Sci. Eng. A 1989: 109: 27–35.
[198] Parks G.A. The isoelectric points of solid oxides, solid hydroxides, and aqueous hydroxo complex systems, Chem. Rev. 1965: 65: 177–198.
[199] Franks G.V., Gan Y. Charging behavior at the alumina-water interface and implications for ceramic processing, J. Am. Ceram. Soc. 2007: 90 3373–3388.

[200] Trevino K.J., Shearer J.C., McCurdy P.R., Pease-Dodson S.E., Okegbe C.C., Fisher E.R., Isoelectric points of plasma-modified and aged silicon oxynitride surfaces measured using contact angle titrations, Surf. Interface Anal. 2011: 43: 1257–1270.
[201] Schroeder A., van der Zypen E., Stich H., Sutter F. The reactions of bone, connective tissue, and epithelium to endosteal implants with titaniumsprayed surfaces, J. Maxillofac. Surg. 1981: 9: 15–25.
[202] Kokubo T. Apatite formation on surfaces of ceramics, metals and polymers in body environment, Acta Mater. 1998: 46: 2519–2527.
[203] Kokubo T., Takadama H. How useful is SBF in predicting in vivo bone bioactivity?, Biomaterials. 2006: 27: 2907–2915
[204] Roebben G., Sarbu C., Lube T., Van der Biest O., Quantitative determination of the volume fraction of intergranular amorphous phase in sintered silicon nitride, Mater. Sci. Eng. A 2004: 370: 453–458.
[205] Witvrouw A., Du Bois B., De Moor P., Verbist A., Van Hoof C.A., Bender H. Comparison Between wet HF etching and vapor HF etching for sacrificial oxide removal, in: Micromach. Microfabr., International Society for Optics and Photonics, 2000, pp. 130–141.
[206] Schrader B. Infrared and Raman spectroscopy: methods and applications, John Wiley & Sons, 2008.
[207] Raman, C. V. A new radiation. *Indian J. Phys.* 1928: 2: 387–398. Retrieved 14 April 2013.
[208] Smekal A. Zur Quantentheorie der Dispersion. *Naturwissenschaften*, 1923: 11 (43): 873–875.
[209] R. Singh, CV Raman and the Discovery of the Raman Effect, Physics in Perspective, 4 (2002) 399-420.
[210] Bowley H.J., Gerrard D.L., Louden J.D., Turrell G., Gardiner D.J., Graves P.R. Practical raman spectroscopy, Springer Science & Business Media, 2012.
[211] Smith E., Dent G. Introduction, basic theory and principles, Modern Raman Spectroscopy-A Practical Approach, (2005) 1-21.
[212] Pawley J.B. (editor) (2006). *Handbook of Biological Confocal Microscopy* (3rd ed.). Berlin: Springer.
[213] Smith E., Dent G. Modern Raman spectroscopy: a practical approach, John Wiley & Sons, 2013.
[214] Ball D.W. The basics of spectroscopy, Spie Press, 2001.
[215] Williams E.R., Steiner R.L., Newell D.B., Olsen P.T. Accurate measurement of the Planck constant, Physical Review Letters, 1998: 81: 2404.
[216] Palinkas G., Bopp P., Jancso G., Heinzinger K. The effect of pressure on the hydrogen-bond structure of liquid water, Z. Naturforsch. A: Phys. Sci. (1984): 39: 179-185.
[217] Marie P. J., Ammann P., Boivin G., Rey C. Mechanisms of action and therapeutic potential of strontium in bone, Calcif. Tissue Int. 2001. 69:121-129.
[218] Wopenka B., Pasteris J.D., A mineralogical perspective on the apatite in bone, Materials Science and Engineering: C, 2005: 25: 131-143.
[219] Corno M., Busco C., Civalleri B., Ugliengo P. Periodic ab initio study of structural and vibrational features of hexagonal hydroxyapatite $Ca_{10}(PO_4)_6(OH)_2$, Physical Chemistry Chemical Physics, 2006: 8: 2464-2472.
[220] Sanchez-Pastenes E., Reyes-Gasga J. Rev. Mexic. Fis., Determination of the point and space groups for hydroxyapatite by computer simulation of CBED electron diffraction patterns, 2005: 51: 525-529.
[221] Wilson R., Elliott J., Dowker S. Rietveld refinement of the crystallographic structure of human dental enamel apatites, America mineralogist, 1999: 84: 1406-1414.
[222] Posner A.S., Perloff A., Diorio A.F. Refinement of the hydroxyapatite structure, Acta Crystallographica, 1958: 11: 308-309.
[223] Narasaraju T., Phebe D. Some physico-chemical aspects of hydroxylapatite, Journal of Materials Science, 1996: 31: 1-21.
[224] Fischer-Cripps A.C. Introduction to Contact Mechanics, Springer (2007).
[225] L. Kravitz, J. Kingsley, E. Elkin, Raman and Infrared Studies of Coupled PO_4^{3-} Vibrations, The Journal of Chemical Physics, 49 (1968) 4600-4610.
[226] De Mul F., Hottenhuis M., Bouter P., Greve J., Arends J., Ten Bosch J., Micro-Raman line broadening in synthetic carbonated hydroxyapatite, Journal of dental research, 1986: 65: 437-440.
[227] Pezzotti G., Zhu W., Boffelli M., Adachi T., Ichioka H., Yamamoto T., Marunaka Y., Kanamura N. Vibrational algorithms for quantitative crystallographic analyses of hydroxyapatite-based biomaterials: I, theoretical foundations, Analytical and bioanalytical chemistry, 2015: 407: 3325-3342.

[228] Nelson D. G. A., Williamson B. E. Low-temperature laser Raman spectroscopy of synthetic carbonated apatites and dental enamel, Aust. J. Chem. 1982: 35: 715-727.
[229] G.S. Kino, T.R. Corle. Confocal scanning optical microscopy and related imaging systems, Academic Press, 1996.
[230] Minsky M. Memoir on inventing the confocal scanning microscope, Scanning, 1988: 10: 128-138.
[231] Andersen M. E., Muggli R. Z. Microscopical techniques in the use of the molecular optics laser examiner Raman microprobe. Analytical Chemistry. 1981: 53 (12): pp 1772–1777.
[232] Honda K, Yokoyama S, Tanaka S. Assignment of the Raman active vibration modes of β-Si_3N_4 using micro-Raman scattering. J Appl Phys 1999;85:7380-7384.
[233] Husson E., Proust C., Gillet P., Itie J.P. Phase transitions in yttrium oxide at high pressure studied by Raman spectroscopy. Materials Research Bulletin: 1999: 34 (12/13): 2085-2092.
[234] Kuball M. Raman spectroscopy of GaN, AlGaN and AlN for process and growth monitoring/control. *Surf. Interface Anal.* 2001: 31: 987-999.
[235] R. Krishnan, R. Kesavamoorthy, S. Dash, A.K. Tyagi, Baldev Raj, Scr. Mater. 2003: 48: 1099-1104.
[236] Kidma K.J., Russell J.H. Raman spectroscopic study of microcrystalline silica. American Mineralogist. 1994: 79: 269-273.
[237] Wadia W., Balloomal L. On the Interpretation of the Vibrational Spectra of Vitreous Silica and Alkali Silicates. Recent Advances in Science and Technology of Materials. 1974: 133-151.
[238] Hurrel J.P., Porto S.P.S., Chang I.F., Mitra S.S., Bauman R.P. Optical Phonons of Yttrium Aluminum Garnet. Physical Review. 1968: 173 (3): 851-856.
[239] Kuzuba T., Kijima K., Bando Y. Raman-active modes of alpha silicon nitride. The Journal of Chemical Physics. 1978: 69: 40.
[240] Penel G, Delfosse C, Descamps M, Leroy G. Composition of bone and apatitic biomaterials as revealed by intravital Raman microspectroscopy. Bone 2005; 36: 893-901.
[241] Cheng W.T., Liu M.T., Liu H.N., Lin S.Y. Micro-Raman spectroscopy used to identify and grade human skin pilomatrixoma. *Micrsc. Res. Tech.* 2005: 68: 75–79.
[242] Golub E.E. Role of Matrix Vesicles in Biomineralization. *Biochim Biophys Acta*. 2009: 1790(12): 1592–1598.
[243] Krafft, C., Neudert, L., Simat, T., and Salzer, R. (2005) Near infrared Raman spectra of human brain lipids. Spectrochimica Acta, Part A, 61: 1529–1535.
[244] Craven, B. M., Crystal structure of cholesterol monohydrate. *Nature* 1976, 260, (5553), 727-9.
[245] Laird, D. F.; Mucalo, M. R.; Yokogawa, Y., Growth of calcium hydroxyapatite (Ca-HAp) on cholesterol and cholestanol crystals from a simulated body fluid: a possible insight into the pathological calcifications associated with atherosclerosis. *J. Colloid Interface Sci.* 2006, 295, (2), 348-363.
[246] Xu, S.; Yu, J. J., Beneath the minerals, a layer of round lipid particles was identified to mediate collagen calcification in compact bone formation. *Biophys. J.* 2006, 91, (11), 4221-4229.
[247] Boyan, B. D.; Schwartz, Z.; Swain, L. D.; Khare, A., Role of lipids in calcification of cartilage. *Anat. Rec.* 1989, 224, (2), 211-19.
[248] Raggio, C. L.; Boyan, B. D.; Boskey, A. L., *In vivo* hydroxyapatite formation induced by lipids. *J. Bone Miner. Res.* 1986, 1, (5), 409-15.
[249] Pully V.V. From Cells to Bone: Raman Microspectroscopy of the Mineralization of Stromal Cells. 2010
[250] Kirsch T, Harrison G, Golub EE, Nah HD. The roles of annexins and types II and X collagen in matrix vesicle-mediated mineralization of growth plate cartilage. J Biol Chem. 2000; 275: 35577.
[251] Stone N., Kendall C., Smith J., Crow P., Barr H. Raman spectroscopy for identification of epithelial cancers. *Faraday Discussion* 2004: 126: 141–157.
[252] Stone N., Kendell C., Shepherd N., Crow P., Barr, H. Near-infrared Raman spectroscopy for the classification of epithelial pre-cancers and cancers. *J. Raman Spectroscopy.* 2002: 33: 564–573.
[253] Jess P. R. T., Smith D. D. W., Mazilu M., Dholakia K., Riches, A. C., Herrington C. S. Early detection of cervical neoplasia by Raman spectroscopy by Raman spectroscopy. *Int. J. Cancer* 2007: 121: 2723–2728.
[254] Frank C. J., McCreecy R. L., Redd D. C. B. Raman spectroscopy of normal and diseased human breast tissues. *Anal. Chem*. 1995: 67: 777–783.

[255] Shen T. F.; Strecker H. J. Synthesis of proline and hydroxyproline in human lung (WI-38) fibroblasts. *Biochem J* 1975: 150: (3), 453-61.)

[256] Kolijenovic S., Scut T.B., Vincent A., Kros J.M., Puppels G.J. Detection of meningioma in dura mater by Raman spectroscopy. Analytical Chemistry, 2005: 77 (24): 7958–7965.

[257] Shetty G., Kedall C., Shepherd N., Stone N., Barr H. Raman spectroscopy: Evaluation of biochemical changes in carcinogenesis of oesophagus. British Journal of Cancer, 2006: 94: 1460–1464.

[258] Chan, J. W., Taylor, D. S., Zwerdling, T., Lane S. T., Ihara, K., and Huser, T. Micro-Raman spectroscopy detects individual neoplastic and normal hematopoietic cells. *Biophys. J.* 2006: 90: 648–656.

[259] Krishna C. M., Prathima N. B., Malini R., Vadhiraja B. M., Bhatt R. A., Fernandes D. J., Kushtagi P., Vidyasagar M. S., Kartha V. B. Raman spectroscopy studies for diagnosis of cancers in human uterine cervix. *Vibrational Spectroscopy*. 2006: 41: 136–141.

[260] Staniszewska-Slezak E., Malek K., Baranska M. Complementary analysis of tissue homogenates composition obtained by Vis and NIR laser excitations and Raman spectroscopy. Spectrochimica Acta Part A: Molecular and Biomolecular Spectroscopy 2015: 147: 245–256

[261] Howell N.K., Arteaga G., Nakai S., Li-Chan E.C., Raman spectral analysis in the C-H stretching region of proteins and amino acids for investigation of hydrophoic interactions. J Agric Food Chem. 1999: 47(3): 924-33.

[262] Hatano, K., Inoue, H., Kojo, T., Tsujisawa, T., Uchiyama, C., & Uchida, Y. (1999). Effect of Surface Roughness on Proliferation and Alkaline Phosphatase Expression of Rat Calvarial Cells Cultured on Polystyrene. Bone, 25, 439-445.

[263] Lim, J. Y., Hansen, J. C., Siedlecki, C. A., Runt, J., & Donahue, H. J. (2005). Human foetal osteoblastic cell response to polymer-demixed nanotopographic interfaces. Journal of Royal Society Interface, 2, 97-108.

[264] Agarwal R, Tandon P, Gupta VD. Phonon dispersion in poly(dimethylsilane). J Organometal Chemi 2006; 691: 2902-2908.

[265] Farguharson S., Shende C., Inscore F. E., Maksymiuk P., Gift A. Analysis of 5-fluorouracil in saliva using surface-enhanced Raman spectroscopy. *J. Raman Spectroscopy* 2005: 36: 208–212.

[266] So Yeon Kim, Ji-Yeon Yoo, Joo-Young Ohe, Jung-Woo Lee, Ji-Hoi Moon, Yong-Dae Kwon, Jung Sun Heo.Differential Expression of Osteo-Modulatory Molecules in Periodontal Ligament Stem Cells in Response to Modified Titanium Surfaces. Hindawi Publishing Coroporation: BioMedi Reasearch International.2014

Chapter 6

Aknowledgements

I wish to remind all those who have been part of my journey in these three years concluded with the achievement of this goal.

Firstly, I would like to thank Professor Pietro Riello, Relator and Professor Giuseppe Pezzotti for allowing me to develop the thesis at the KIT in Japan, giving me the opportunity to learn and apply myself to new environments and cultures.

To my tutor, Dr. Alfredo Rondinella for welcoming me, for putting up with me and for the help in the writing of this thesis; with him I also would like to thank Dr. Elia Marin for guidance, advice and assistance received. I wish these people a successful future.

I want to thank my family and my friends for everything they have made, sharing different moments throughout these years.

Thank you.